Universidad de Chile
Facultad de Ciencias Físicas y Matemáticas
Departamento de Astronomía

SUB-MILLIMETER STUDIES OF COLD GAS AND DUST IN THE MAGELLANIC CLOUDS

TESIS PARA OPTAR AL GRADO DE MAGÍSTER EN CIENCIAS MENCIÓN ASTRONOMÍA

by

CELIA ANAHÍ VERDUGO SALGADO

Advisor Professor	:	Mónica Rubio López
Examiner Comitee	:	Alberto Bolatto
		Leonardo Vanzi
		Ricardo Muñoz Vidal

Santiago - Chile.
April, 2012.

Presentamos datos a 870 μm obtenidos con el telescopio APEX en la SMC, LMC y puente Magallánico, obteniendo imágenes con $22''.4$ de resolución para 9 nubes moleculares gigantes. Usamos estos datos en combinación con observaciones de Spitzer (SAGE) y Herschel (HERITAGE) para construir distribuciones de energía espectral (SEDs) y ajustar una ley de cuerpo negro modificada simple, a fin de determinar temperaturas de polvo, índices de emisividad espectral β y opacidades de polvo. Encontramos valores promedios de temperaturas de polvo de 22, 24 y 19 K para la LMC, SMC y puente Magallánico respectivamente, y para los índices de emisividad espectral estos resultados fueron 1.7, 1.6 y 1.7. Encontramos opacidades de polvo promedio a 870 μm de 9, 4 y 2 $\times 10^{-5}$ para la LMC, SMC y puente Magallánico respectivamente. De las SEDs encontramos un claro exceso de emisión a 870 μm con respecto a la ley de cuerpo negro modificada. Para la LMC, estos excesos variaron de 0.3 a 3 veces lo que había sido predicho por la ley de cuerpo negro modificada a 870 μm, y de 1.3 a 2.5 veces para la SMC. El puente Magallánico reportó el exceso más alto con un factor de 9. Con el propósito de entender este exceso de emisión a 870 μm, realizamos un análisis de tres partes con los resultados que se obtienen a partir de la emisión a 870 μm: la emisividad del polvo, la masa de gas y la razón de gas-a-polvo. Usando datos complementarios de CO determinamos densidades de columna de hidrógeno a partir de masas viriales, y junto con las opacidades de polvo obtenidas de los ajustes, calculamos emisividades de polvo por columna de gas, permitiéndonos determinar masas de gas y polvo a partir de la emisión milimétrica a 870 μm. Estas emisividades de polvo resultaron mayores que el valor Galáctico de Boulanger et al. (1996), indicando una mayor emisividad del polvo o que la aproximación virial estaría equivocada. Adicionalmente, calculamos masas de gas a partir de la emisión milimétrica usando el valor de emisividad de Bot et al. (2010), el cual es un valor Galáctico correguido por metalicidad, y las comparamos con las masas viriales obtenidas a partir de los datos complementarios de CO. Obtuvimos masas milimétricas de gas mayores que las masas viriales en un factor de 2-14 en la LMC, 2-6 en la SMC y 100 en el puente Magallánico. Esto nuevamente indica que la aproximación virial estaría equivocada, por lo tanto no estaría trazando toda la masa de gas, o que la emisividad a 870 μm es más alta, produciendo una sobrestimación de la masa de gas a partir de la emisión milimétrica. Finalmente, usamos masas de polvo obtenidas a partir de la emisión milimétrica usando el resultado de emisividad de Bot et al. (2010), y las masas de gas a partir de los datos de CO y la aproximación virial para determinar razones de gas-a-polvo. Obtuvimos valores más altos que el Galáctico (~ 100), indicando menores cantidades de polvo en relación al gas que en nuestra Galaxia. Esto muestra la dificultad en explicar el exceso de emisión a 870 μm como una componente en masa en estos sistemas de bajo contenido de polvo, y tal vez sería la emisividad del polvo que es distinta a 870 μm y que produce este exceso de emisión.

Abstract

We present data at 870 μm obtained with the APEX telescope in the SMC, LMC and Magellanic Bridge, yielding images with a $22''.4$ resolution of 9 giant molecular clouds. We used these data in combination with Spitzer (SAGE) and Herschel (HERITAGE) observations to construct spectral energy distributions (SEDs) and fitted a single modified blackbody law in order to determine dust temperatures, spectral emissivity indices β and dust opacities. We found average values for dust temperatures of 22, 24 and 19 K for the LMC, SMC and Magellanic Bridge respectively, and for spectral emissivity indices these results were 1.7, 1.6 and 1.7. We found average dust opacities at 870 μm of 9, 4 and 2 $\times 10^{-5}$ for the LMC, SMC and Magellanic Bridge respectively. From the SED's we found a clear excess of emission at 870 μm with respect to the modified blackbody law fitted. For the LMC, these excesses varied from 0.3 to 3 times what was predicted by the modified blackbody law at 870 μm, and from 1.3 to 2.5 times for the SMC. The Magellanic Bridge reported the highest excess with a factor of 9. With the aim to understand this excess of emission at 870 μm, we made a three-parts analysis with three results obtained from the emission at 870 μm: dust emissivity, gas mass and gas-to-dust ratio. By using CO complementary data we determined hydrogen column densities from virial masses, and along with the dust opacities obtained from the fit, we calculated dust emissivities per gas column, allowing us to determine dust and gas masses from the millimeter emission at 870 μm. These dust emissivities were higher then the Galactic value from Boulanger et al. (1996), indicating a higher emissivity of the dust or that the virial approximation would be wrong. Additionaly, we calculated gas masses from millimeter emission using the emissivity value of Bot et al. (2010), which is a Galactic value corrected for metallicity, and compared them with virial masses obtained from the complementary CO data. We obtained millimeter gas masses higher than the virial masses by a factor of 2-14 in the LMC, 2-6 in the SMC and 100 in the Magellanic Bridge. This once again indicates that the virial aproximation could be wrong, therefore not tracing the total amount of gas, or that the emissivity at 870 μm is higher, producing an overestimation of the gas mass from millimeter emission. Finally, we used dust masses obtained from the millimeter emission using the emissivity result of Bot et al. (2010) and gas masses from CO data and virial approximation to determine gas-to-dust ratios. We obtained values higher than the Galactic (~ 100), indicating lower dust contents in relation with gas than in our Galaxy. This shows the difficulty in explaining the excess of emission as a mass component in these system with low dust contents, and maybe it is the emissivity of the dust that is different at 870 μm and would be causing this excess of emission.

Esta tesis está dedicada con mucho cariño a Felipe, Andrés y Sergio,
pues sin ellos no lo podría haber logrado.

Acknowledgments

No creo poder explicar con palabras la cantidad de trabajo y esfuerzo que me significó esta tesis. Fue un trabajo que me causó tanto inspiraciones como cansancio a ratos, pero siempre motivo aún más mi interés por la astronomía. Tuve la suerte de participar en este proyecto desde el momento de las observaciones, experiencias de las cuales aprendí muchísimo. Yo misma realizé la reducción de los datos encontrandome con muchos problemas en el camino, pero por muy difícil que haya parecido a ratos, la experiencia, aprendizaje y satisfacción que me trajo resolver problemas que en un momento me parecieron insolubles fue impagable. Esta valiosa experiencia se la debo a muchas personas, y sólo espero algún día poder retribuirles de alguna manera todo lo que hicieron por mí.

En primer lugar quiero agradecer a mi profesora guía Mónica Rubio por el apoyo incondicional que me otorgó durante todo este proceso. Me ha guidao y ha estado conmigo en todo momento, apoyandome en decisiones, viajes y publicaciones. De su parte siempre sentí una gran valoracion de mi trabajo, y siempre me puso en el primer plano de sus prioridades académicas. Le agradezco de todo corazón la dedicación y preocupación que puso en mi para impulsar mi carrera que está recién empezando, por estar siempre preocupada del bienestar de los estudiantes, apoyandolos y defendiendolos en todo, por jugarsela por las nuevas generaciones.

Asimismo quiero agradecer también a mi profesor co-guía Alberto Bolatto, que a la distancia me ayudó en todo mi trabajo, respondiendo todas y cada una de mis inmumerables preguntas. No cualquiera se da el tiempo de atender a un estudiante a la distancia y de otra institución. Le agradezco enormemente que me haya recibido en dos oportunidades en Maryland para ayudarme con mi trabajo, y por todos los consejos y enseñanzas que me dió. Sin duda le debo gran parte de este trabajo.

También quiero agradecer sinceramente a mi familia, de quienes he recibido un amor y apoyo incondicional durante toda mi vida. Mi padres siempre han estado muy orgullosos de mi y me apoyaron desde un principio en esta difícil carrera. La enorme confianza que han depositado mi me ha llevado hasta donde estoy ahora. Y sin duda mis hermanos, quienes adoro con todo el corazón, han sido mis ejmplos a seguir. Ellos me han apoyado y cuidado en todo momento y nunca acabaré de agradecerles por facilitarme la vida en todo aspecto.

Además quiero agradecer a todas las personas que me ayudaron a la distancia frente a todos los problemas que enfrente en la reducción de los datos, en particular a Erik Muller, Marcus Albrecht y Axel Weiss. También quiero agradecer a todo el staff de APEX por acogerme y ayudarme, no solo durante los runs de observación sino por haber contestado todos mis mails. Quiero agradecer con mucho cariño a Mauricio Matínez, Felipe McAllife, Rodrigo Parra y Giorgio Siringo que se dieron incontables minutos para explicarme pacientemente todo lo que les pedí, tanto dentro como fuera de sus horas de trabajo.

Por último, quisiera agradecer a todas las personas que componen Cerro Calán, que son como una familia. Sin duda creo que la mayor riqueza de este departamento está en su gente, siempre dispuesta a brindar una sonrisa y ayuda desinteresada, y estoy segura que es lo que mas hecharé de menos. Quiero agradecer a todos mis compañeros por las ayudas y los buenos ratos que pasamos juntos. En este departamento hice grandes amigos que me brindaron muchas alegrías y ayudas invaluables, y sé que al dejarlos atrás no encontraré un grupo de gente igual. Quiero

agradecer especialmente a mis compañeros de oficina, quienes se convirtieron en mis mejores amigos de Calán y me brindaron solo alegrías y buenos ratos. Sin la ayuda que me dieron no podría haber termiando esta tesis. Por eso y por mucho más siempre los llevaré en mi corazón a donde quiera que vaya.

Quisiera agradecer el apoyo financiero otorgado por FONDAP a través del convenio n° 15010003 y FONDECYT con fondo n° 1080335 a lo largo de todo mi master. También agradezco a SOCHIAS por financiarme viajes a escuelas y conferencias en el extranjero que complementaron mi formación académica.

Contents

Chapter 1

Introduction

1.1 The Magellanic Clouds

Visible in the sky at naked eye, the Small Magellanic Cloud and Large Magellanic Cloud, hereafter SMC and LMC respectively, are the closest irregular satellite galaxies to our own, the Milky Way. At a distance of 61 kpc (Hilditch et al. 2005) for the SMC and 50 kpc for the LMC (Persson et al. 2004), the Magellanic Clouds are the nearest galaxies to study the evolution and structure of molecular clouds, where the star formation takes place. Figure 1.1 shows HERSCHEL images at 160 μm of the SMC and LMC. These galaxies are gas-rich and low metallicity environments ($Z_{LMC} = 0.5Z_{\odot}$, Keller & Wood 2006 and $Z_{SMC} = 0.1Z_{\odot}$, Maeder et al. 1999), in which the amount of available gas has been determined in numerous molecular clouds in order to eventually quantify the ongoing star formation. Comparisons with our Galaxy are important since these galaxies, with their lower metallicities, could be considered as representations of universe farther in look-back time, and can give answers to some questions that our Galaxy cannot. A third component of the Magellanic system will be analysed: the Magellanic Bridge. A gas and dust stream that seem to connect the SMC and LMC. It is a less studied region but with a particular interest since it has a lower metallicity than the SMC and LMC. It can be seen in the SMC image of Figure 1.1

1.2 Observing molecular clouds

Molecular clouds are constituted mainly of hydrogen, which at the typical low temperatures of molecular clouds ($\sim$10 K) tends to be molecular and is extremely difficult to observe.

Even though hydrogen is the most abundant element in the universe, observing molecular hydrogen is highly difficult in the ISM. For H_2, the first excited state, the J = 1 rotational state, is 100 - 200 K above ground state, whereas typical molecular clouds have temperatures of a few tens, making this transition highly unlikely. Even more, since the H_2 is a homonuclear molecule, it is difficult to observe because it has no electric dipole transitions that can change J by 1 (therefore no J = 1$\rightarrow$0 emission) and the nearest transitions are the quadrupolar (J = 2$\rightarrow$0) with a very low probability, because the J = 2 state is 511 K above ground state. The basic reason of why it is so difficult to observe molecular hydrogen is its low mass. For a quantum oscillator or rotor the level spacing varies with reduced mass as $m^{-1/2}$, making it so difficult to

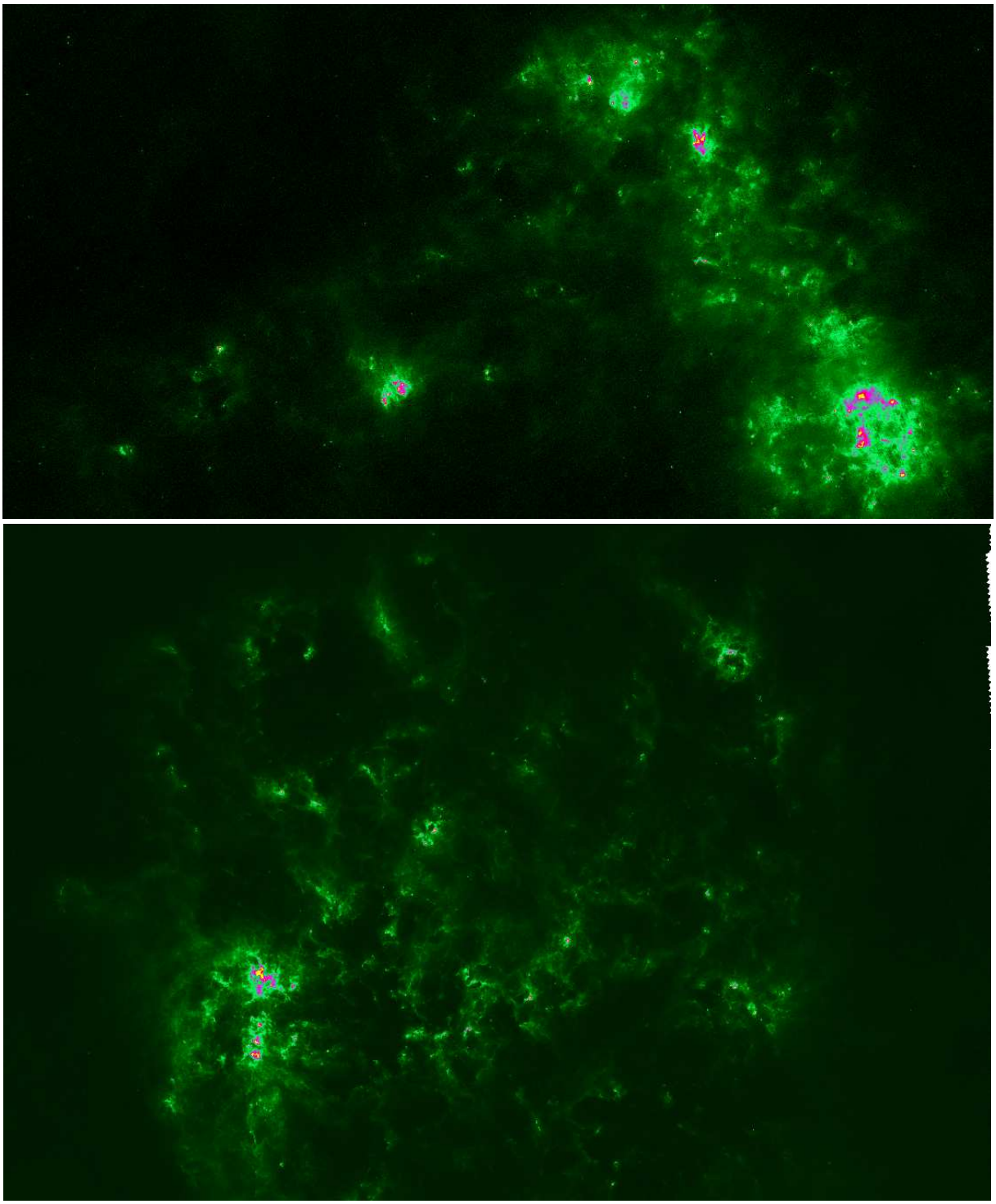

Figure 1.1: HERSCHEL images of the entire SMC (top) and LMC (bottom) at 160 μm (north up). SMC image is 4×3 deg and LMC image is 6×6 deg.

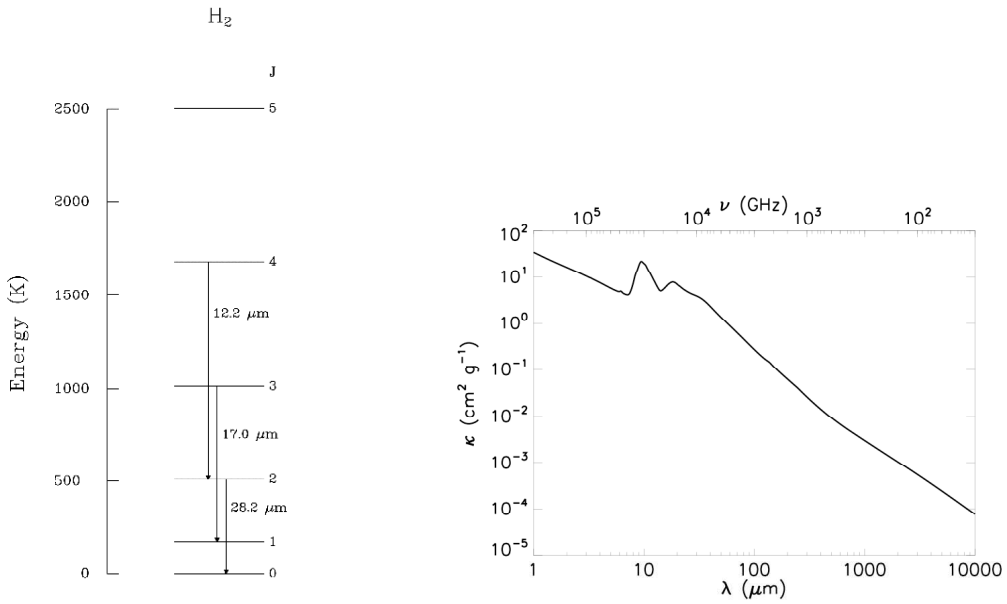

Figure 1.2: *Left:* H_2 energy levels. *Right:* Dust absorption coefficient.

go from one transition to another (Figure 1.2 *Left*). For these reasons we turn to other tracers to determine the amount of H_2. The most common one is the CO molecule, thanks to its dipole moment and its bright emission line. Carbon and oxygen are two of the most common elements in the ISM beyond H and He, and since the CO molecule is much more massive than H_2, its lowest rotational state is only 5.5 K above ground state, making CO molecules abundant with bright emission lines, easy to detect. As a consequence, CO has long been used as the preferred molecular gas tracer. Unfortunately, at low metallicities (the case for the Magellanic system) CO can be photo-dissociated by UV radiation and thus traces only the densest parts of the cloud, while H_2 molecules can extend farther.

Another tracer for molecular gas is dust. Interstellar gas clouds are always mixed with dust, and dust grains emit thermal radiation which we can observe. Dust continuum emission can be used to trace the dense and cold interstellar medium where the gas is molecular and it can therefore be used to unveil the total mass of dense gas in clouds. The advantage of dust grains is that, since they are solid particles, they can absorb or emit continuum radiation, which the gas cannot. Dust grains have their lower absorption coefficients at longer wavelengths, this is why we shift to the millimeter and sub-millimeter range (Figure 1.2 *Right*).

Numerous molecular clouds in the Magellanic Clouds have been observed in CO lines (Israel et al. 1993, Rubio et al. 1993b, Rubio et al. 1993a, Rubio et al. 1996) and were found to have weak CO emission, in line intensity and velocity dispersion. This indicates the possibility that CO observations largely underestimate the amount of molecular gas in these low metallicity conditions.

1.3 Mass Discrepancy

In our Galaxy, CO and molecular gas (H_2)are spatially correlated, implying that the CO molecule, which is easy to observe, is a good tracer for H_2. In fact, in our Galaxy all mass tracers (dust continuum, CO line intensity, virial theorem through CO velocity dispersion) give the same amount of gas (Dame et al. 2001).

But in low metallicity systems such as the Magellanic Clouds, this CO-H_2 correlation does not seem to be valid, since gas masses inferred from the dust emission are unexpectedly higher than gas masses obtained from the CO emission line, which could be showing that CO might not be tracing the entire content of molecular mass. A possible explanation for this relies on the fact that the Magellanic Clouds have lower metallicity and therefore dust content than our Galaxy. A lower metallicity implies a less relative amount of heavy elements in the entire system, including the two elements that make up the CO molecule: carbon and oxygen. A lower dust content also affects the abundance of CO because it is a natural shield from the external UV radiation that can destroy the molecule. H_2 has the property of self-shielding from this radiation, but CO does not. When UV photons first enter the cloud they find their way in quite easily because of the few dust grain they encounter, but as they keep trying to get deeper into the center of the cloud, the probability of being absorbed by the surrounding atoms grows, so it becomes more difficult for them to reach the inner parts of the cloud, leaving dense clumps of CO free from this photodissociation. This could be an explanation of the lower abundance of CO in systems where the dust-to-gas ratio is lower than in our Galaxy, and therefore it would not be tracing all the (not-photodissocated) H_2. In this sense, dust emission would be a much better tracer for the molecular gas because it stays unaffected by the UV radiation from the surroundings of the cloud and it is intrinsically related to the gas content, since H atoms need dust grain surfaces to couple and form H_2 molecules.

Gas masses have been determined using to dust observations in low metallicity systems. The first result for the SMC showed that the masses derived from dust emission were larger than the masses reported from CO line intensities or virial mass determinations from CO velocity dispersions (Rubio et al. 2004), indicating that in fact CO emission is coming from the densest parts of the cloud and does not trace the full cloud area and velocity distribution. In particular, new studies in giant molecular clouds (GMCs) in the SMC have shown a discrepancy between cloud masses deduced from 0.87 mm (LABOCA) and 1.2 mm (SIMBA) continuum emission and their virial masses (thought to trace the entire cloud potential; Rubio et al. 2004, Bot et al. 2007, 2010), giving dust continuum masses almost 4 times larger than virial ones. Thus, CO observations would be underestimating the total amount of gas mass. Back then this was quite an unexpected result since in our galaxy all mass tracers give the same amount of gas.

1.4 Procedure

This work presents sub-millimeter LABOCA observations at 870 μm of 29 molecular clouds in the Magellanic system. These data were complemented with HERSCHEL and SPITZER data in order to construct spectral energy distributions (SEDs) with the purpose of fitting a single modified blackbody law to determine dust temperatures, spectral emissivity indices and dust opacities. From CO complementary data we determined virial masses and hydrogen column densities which, along with the dust opacities from the fitting procedure, were used to determine

dust emissivities per gas column and compare them with the results in our Galaxy. From the results of dust emissivities we were able to calculate dust and gas masses from the sub-millimeter emission. In combination with the virial masees calculated with the complementary CO data, we used dust masses from millimeter emission to calculate gas-to-dust ratios.

1.5 Thesis structure

We present a description of the LABOCA observations and complementary data in Chapter 2, and the details for the LABOCA data reduction in Chapter 3. Results of flux densities measured from the photometry are in Chapter 4, along with the spectral energy distributions and fitting results. Chapter 5 presents the analysis of sub-millimeter excess, dust emissivities and dust and gas masses, and final discussions and conclusions are in Chapter 6.

Chapter 2

LABOCA Observations and Data

At the typical low temperatures of molecular clouds (tens of Kelvins), sub-millimeter wavelenghts (around 200 μm to 1 mm) take special interest. Bolometers are among the most sensitive available detectors at these wavelenghts. Basically, they are devices for measuring incident power via the heating of a material. They can be simplified as the combination of an extremely sensitive temperature sensor called thermistor and a radiaton absorber (Siringo et al. 2009). The absorber is conected to a thermal reservoir through a thermal link, so the absorved power increases the temperature and the temperature change can be measured directly by the thermistor.

Also at the typical temperatures of molecular clouds, from Wien law's we have that the peak of emission is expected to be around 100-200 μm, so we used the SPITZER map at 160 μm to select sources to be observed, privileging the ones with known previous CO data.

We carried out 870μm observations with the Large APEX Bolometer Camera (LABOCA) (Siringo et al. 2009) on the Atacama Pathfinder Experiment (APEX, Güsten et al. 2006) telescope in Llano de Chajnantor. LABOCA is an array of bolometers specifically designed for fast mapping of large areas of the sky at moderate resolution and with high sensitivity (Siringo et al. 2009). It is a 295-channel facility bolometer camera (Schuller et al. 2008) with a central frequency at 345 GHz, a bandwidth of 60 GHz, a beamsize of $19''.2$ and a total field of view (FOV) of $11'.4$. The footprint in the sky of the bolometers array can be seen in Figure 2.1. Observations took place in August and October 2010 (project C-086.F-0679A-2010), in mostly good to excellent weather conditions with a precipitable water vapor (PWV) content typically between 0.2 and 0.9 mm. We derived calibration factors by observing Neptune and Uranus, as well as secondary calibrators G5.89, N2071IR and G34.3. The observing mode was spiral raster. Spirals are done with a movement of the LABOCA instrument with a constant angular speed and an increasing radius, allowing an efficient and homogeneous coverage of the source (Figure 2.1 left). For more extended sources these spirals can move in specified directions to cover the whole area of interest (Figure 2.1 right).

Table 2.1 presents the sources observed in the project, with their coordinates, integration times, rms and peak signal-to-noise (S/N), and map sizes. Figure 2.2 shows their locations.

In addition to our observations, a LABOCA $\sim$1.2$\times$1.2 deg^2 map at 870 μm of the entire south-west region of the SMC was reduced at Bonn University (M. Albrecht) combining data from projects C-080.F-0018-2007 (Bot et al. 2010), C-086.F-0679A-2010, C-087.F-0020A-2011 and

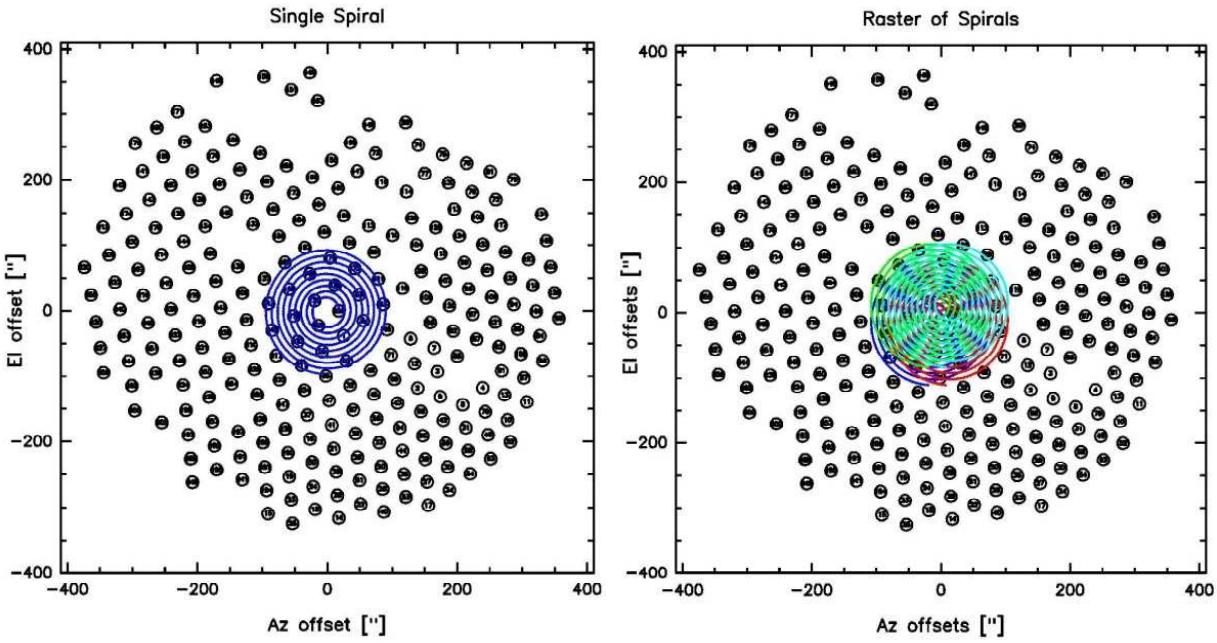

Figure 2.1: LABOCA spirall raster

Table 2.1. Sources in LMC, SMC and Magellanic Bridge selected for the sample and their observing properties

Source	α (J2000) [^{hr}: ' : "]	δ(J2000) [°: ' : "]	Int. time [hrs]	rms [mJy/beam]	S/N	map size [arcmin]
SMC-M	00 40 00	-73 00 00	5.87	7	no detection	15×15
SMC-mid	00 50 00	-72 51 31	4.29	13	no detection	30×30
LMC-N159	05 39 34.6	-69 45 34.8	0.73	15	36	15×15
LMC-N113	05 13 20	-69 22 38	0.74	8	39	15×15
LMC-N71	05 13 12	-69 39 00	1.32	8	10	15×15
LMC-N80	05 16 39.8	-68 12 18.3	6.08	12	4	20×40
LMC-N4	04 52 8.2	-66 55 16	0.23	15	12	15×15
LMC-S2	05 41 38	-71 19 11	1.03	15	8	20×20
LMC-S6	05 39 56	-71 10 08	0.39	12	13	10×10
LMC-N52	05 47 00	-70 40 00	2.57	6	3.5	15×15
MagBridge-A	01 43 41.8	-74 32 28	3.94	5	2	15×15
MagBridge-B	01 49 24.4	-74 37 52.4	7.2	5	no detection	10×10
MagBridge-C	01 56 47.5	-74 17 41.3	20	3	no detection	10×10

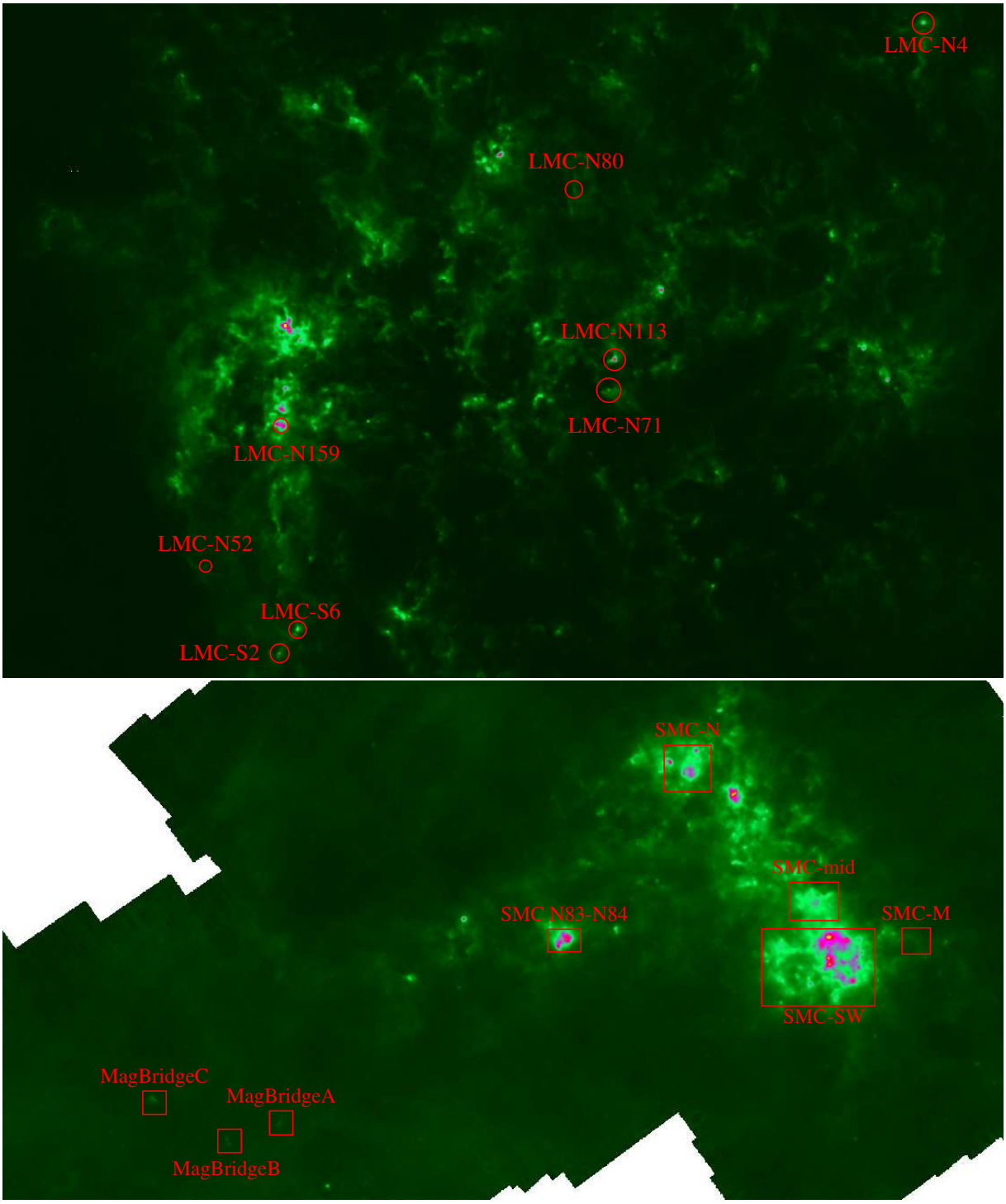

Figure 2.2: Molecular clouds observed in the LMC (top) and SMC (bottom) in SPITZER images 160 μm (north up). SMC image is $\sim$4×3 deg and LMC image is $\sim$6×6 deg. SMC-N was observed but there was no detection, the desired rms was not reached.

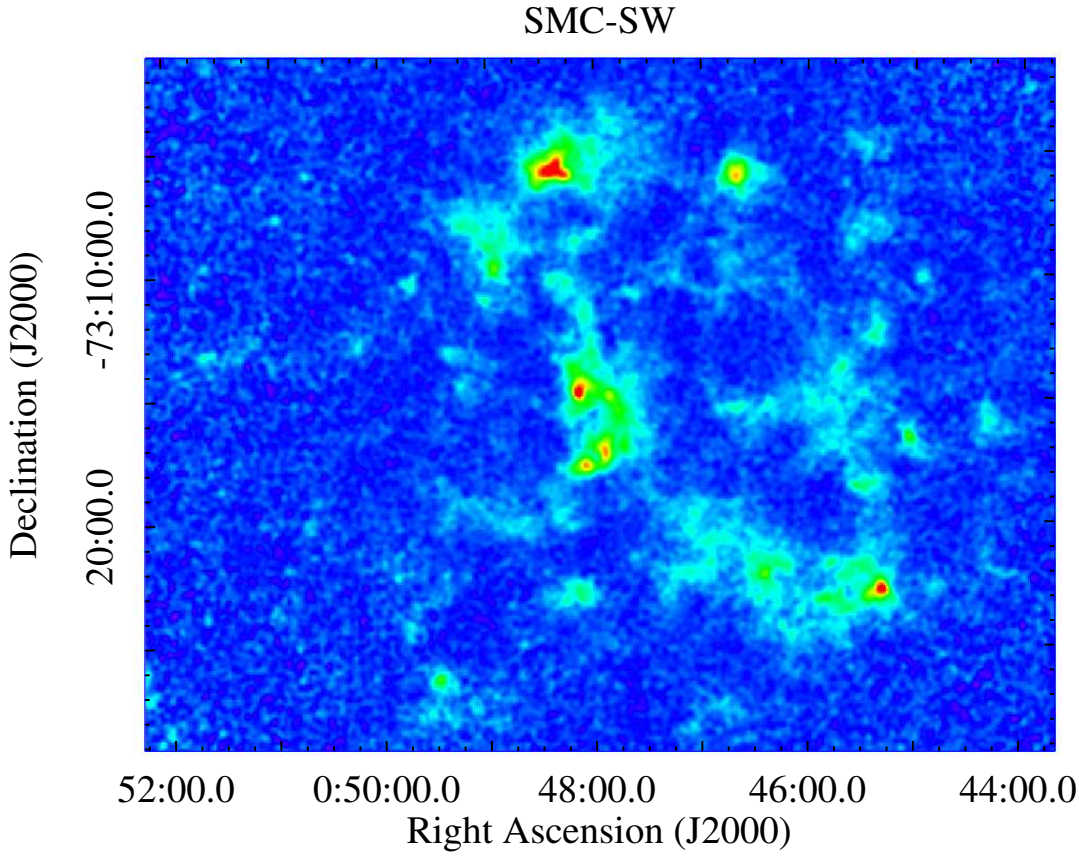

Figure 2.3: SMC-SW LABOCA map (M. Albrecht)

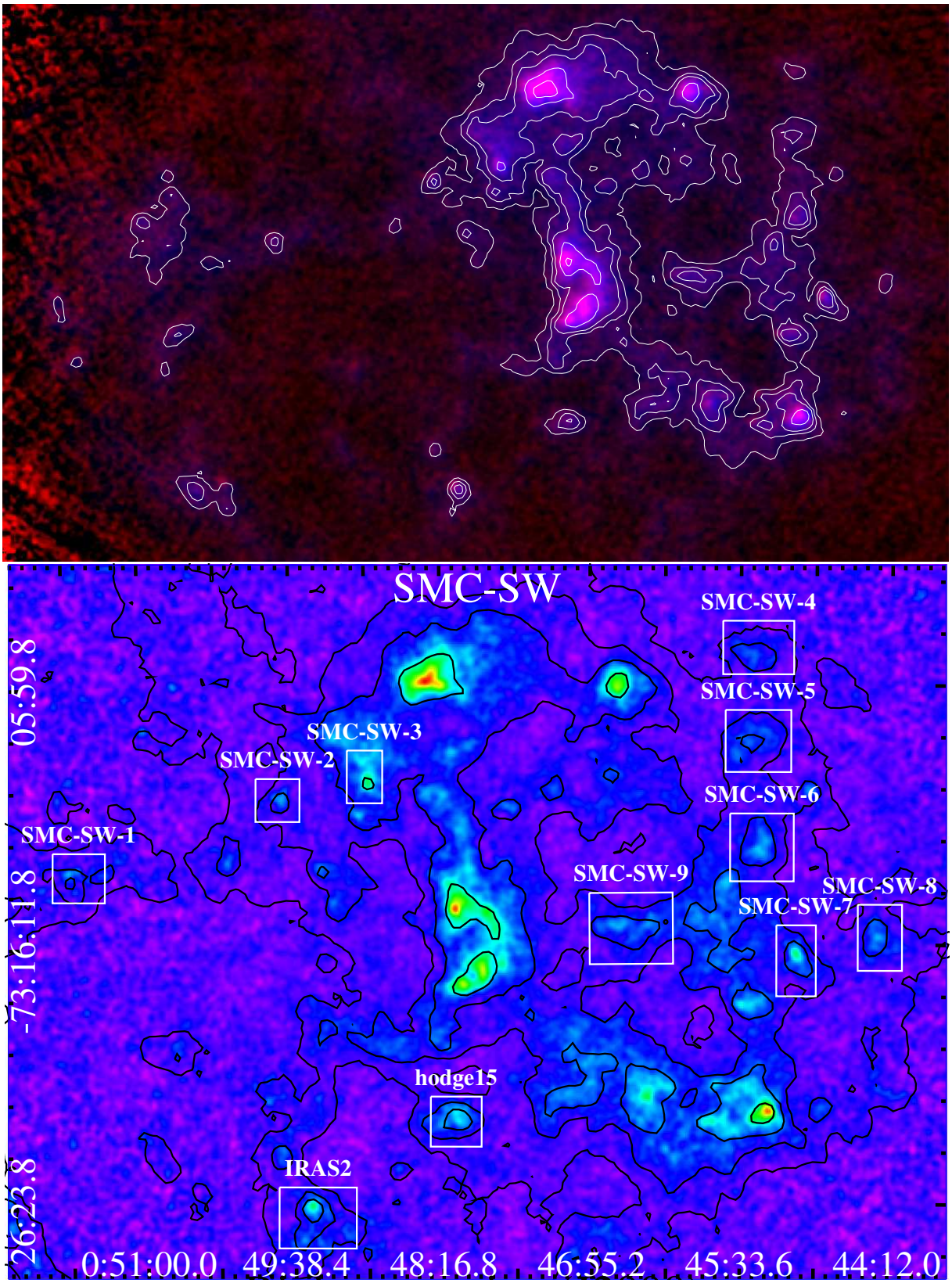

Figure 2.4: Top: Composite color image of SMC-SW region. In red, LABOCA image (870 μm). Blue and white contours, 500 μm emission form HERSCHEL. Bottom: Molecular clouds selected in the SMC-SW region (coordinates in J2000). Black contours represent emission at 500 μm from HERSCHEL data

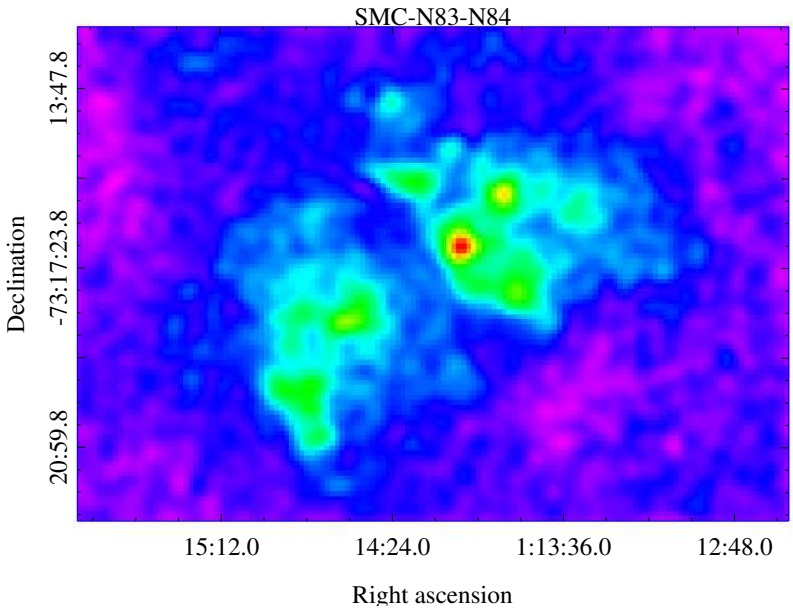

Figure 2.5: LABOCA map for N83-N84 (870 μm) from Guzmán (2010).

E-081.C-0826A-2008 (ESO data. PI A. Leroy). Figure 2.3 shows this map. Since dust particles are colder than gas, they have their peak of emission at longer wavelenghts ($> 500\mu m$), so by combining this LABOCA image with emisison at 500 μm from HERSCHEL (see Top Figure 2.4) we selected eleven aditional sources where the dust is expected to emit. Figure 2.4 shows these sources and their coordinates are presented in Table 2.2. Most of these sources where selected for having previous CO data (M. Rubio). Additionally, we included to the sample a LABOCA map of the N83-N84 complex in the SMC from Guzmán (2010) (Figure 2.5), also with previous CO observations (Bolatto et al. 2003). Figure 2.2 (bottom) presents the locations in the SMC of these two regions, SMC-SW and the N83-N84 complex.

2.1 Complementary Data

We used HERSCHEL data obtained by the Heritage team (PI M. Meixner with M. Rubio and A. Bolatto team members), providing us with maps of the entire SMC with the Magellanic Bridge and the LMC at 100, 160, 250, 350 and 500 μm. The Photodetector Array Camera and Spectrometer (PACS) operates at a wavelength range between 60 and 210 μm. (Poglitsch et al. 2010). The PACS 100 and 160 μm images of the LMC and SMC have resolutions of $9''$ and $14''$ respectively. The Spectral and Photometric Imaging Receiver (SPIRE) instrument contains an imaging photometer (camera) operating in three wavelength bands centered on 250, 350 and 500 μm, and so can make images of the sky simultaneously in three sub-millimeter "colors". (Griffin et al. 2006). The resolutions of these images are $22''$, $30''$ and $43''$ respectively

We also used two SPITZER images, one at 70 and one at 160 μm, for the LMC obtained from The Multiband Imaging Photometer for Spitzer (MIPS) database (Meixner et al. 2006), and two images (70 and 160 μm) for the SMC from Bolatto et al. (2007) The SPITZER images at

Table 2.2. New Sources in SMC southwest region selected for the sample

Source	α (J2000) [^{hr}: ' : "]	δ(J2000) [$^{\circ}$: ' : "]
IRAS2	00 49 29.2	-73 26 26.9
hodge15	00 48 10.4	-73 22 57.6
SMC-SW-1	00 51 38.6	-73 13 28.6
SMC-SW-2	00 49 44.2	-73 10 32.9
SMC-SW-3	00 48 57.4	-73 09 28.8
SMC-SW-4	00 45 29.7	-73 04 50.6
SMC-SW-5	00 45 27.3	-73 08 14.4
SMC-SW-6	00 45 22.2	-73 12 23.7
SMC-SW-7	00 45 02.3	-73 16 47.3
SMC-SW-8	00 44 19.1	-73 15 57.6
SMC-SW-9	00 46 42.2	-73 15 26.6

Table 2.3. CO data

Source	transition	telescope	FWHM[$''$]	reference
MagBridgeA	$CO(3-2)$	ASTE	22	E. Muller priv. comm.
LMC-N159	$CO(2-1)$	SEST	23	Bolatto et al. (2000)
LMC-N113	$CO(3-2)$	APEX	20	Wang et al. (2009)
LMC-N4	$CO(1-0)$	SEST	43	Heydari-Malayeri & Lecavelier Des Etangs (1994)
LMC-N52	$CO(2-1)$	SEST	23	M. Rubio priv. comm.

70 and 160 μm map the entire SMC with the Magellanic Bridge and the LMC. Additionaly, we obtained 1.2 mm SIMBA data for LMC-N159 from M. Rubio (Rantakyrö et al. 2005).

To subtract CO contributions, we obtained CO data from different telescopes and collaborations. For some sources we used individual CO maps presented in Table 2.3, and for the rest of the sources we used CO(1-0) NANTEN maps of the entire galaxies at a $60''$ beamsize resolution.

Chapter 3

Data Reduction

We reduced our LABOCA data using BoA, the designed software package for the reading, handling and analysis of bolometer array data (Schuller et al. 2008). Before carrying out the actual data reduction, we need to make a calibration procedure in order to correct for opacity and calibrate the flux measurements.

3.1 Data Calibration

Recalling that in the millimeter and sub-millimeter range the approximation for the specific intensity I_ν (the power emitted by the source per unit frequency, per unit area and per unit solid angle as a function of planck's law at a dust temperature T

$$I_\nu = \tau_\nu^{atm} B_\nu(T) \tag{3.1}$$

is valid, we can see that τ_ν^{atm}, the atmospheric opacity term ($\ll 1$) that indicates how transparent (optically thick or thin) is the medium, attenuates in a linear way all radio observations, and the determination of its value is essential for processing bolometric data. For LABOCA data there are two independent methods to determine opacities. The first one relies on the PWV level measured every minute by the APEX radiometer broadly along the line of sight. The PWV is converted into an opacity value using an atmospheric transmission model (ATM, Pardo et al. 2001) and the LABOCA passband. The accuracy of this approach is limited by the knowledge of the passband, the applicability of the ATM and the accuracy of the radiometer (Siringo et al. 2009). The second method uses skydips, which are scans designed to measure the power of the atmospheric emission as a function of the airmass while tipping the telescope from high to low elevation, where τ_ν^{atm} increases with airmass. Skydips consist in detail of two scans: one hot-sky scan or bolotip scan that measures the zenith sky temperature, and the skydip itself at a given elevation that calculates the observed sky temperature at that elevation. Finally the zenith opacity is fitted to the sky temperature-elevation curve (Figure 3.1). Since radiowavelengths are very sensitive to changes in the atmosphere, these skydip measurements are repeated many times during observations, obtaining one temperature-elevation curve and therefore one τ_ν for every skydip measure.

Once the zenithal opacity correction factors are obtained we need to do a flux calibration correc-

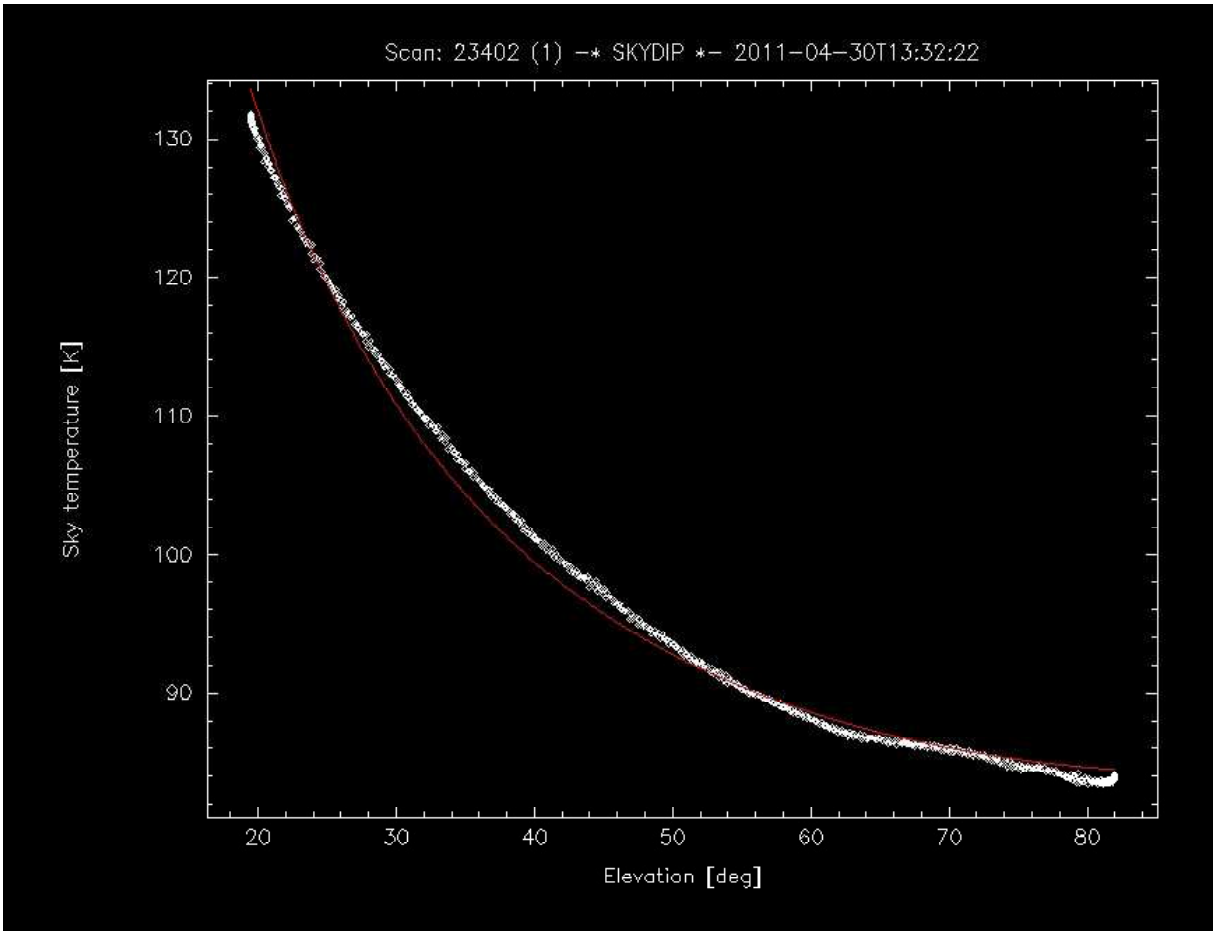

Figure 3.1: Sky temperature - elevation curve

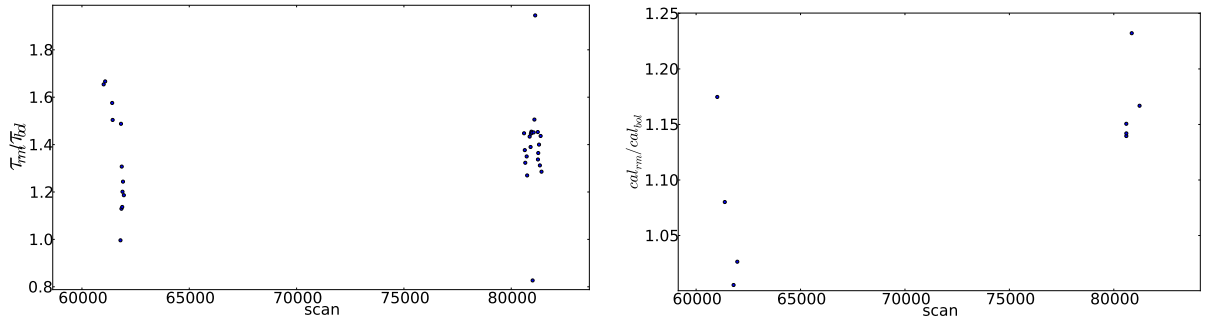

Figure 3.2: *Left:* Comparison of $\tau's$ values obtained from the radiometer and from bolotip measurements for every bolotip scan. *Right:* Comparison of flux calibration correction factors obtained from radiometer $\tau's$ and bolotip $\tau's$ for every calibrator scan. In both figures points in the left side correspond to August observations and points to the right side to October observations

tion, in order to determine if the fluxes obtained by the instrument are accurate or not. For this purpose only bright sources are used, like planets (primary calibrators) and ultracompact HII regions, protostellar objects and AGB stars (secondary calibrators), and their measured fluxes are compared with the ASTRO fluxes corresponding to the specified time and location of the observation.

An interesting result of this calibration procedure was a comparison between both methods for determining zenithal opacities: radiometer and bolotip measurements. τ values obtained by the radiometer turned out to be larger than the bolotip $\tau's$ by a factor $\sim$1.4 due to an underestimation of the zenithal opacities determined by BoA from the bolotips (Figure 3.2 *left*). As BoA uses the values of zenithal opacities in the determination of calibration correction factors, an underestimation of a τ value will directly affect the real estimations of such calibration factors. A comparison was done between calibration flux correction factors calculated with the τ values from the radiometer and from the bolotips (Figure 3.2 *right*).

As can be seen in Figure 3.2, an underestimation of a zenithal opacity results in a direct underestimation of the attenuation in the emission of the source due to the atmosphere and therefore underestimating the real flux correction factor. This is why calibration correction factors measured from the radiometer are larger than the ones measured from the τ bolotips. Our tests proved that reductions made with the bolotips $\tau's$ had overestimated flux values, making this method unreliable. Moreover, calibrations made with radiometer $\tau's$ are significantly more accurate since these are taken for each scan during observations, whereas bolotips are taken with a variable frequency depending on the weather conditions, but typically when changing targets during the observations. This implies that calibrations with bolotips $\tau's$ use and interpolation to obtain a calibration factor for every scan between two bolotip measurements, whereas radiometer taus give the actual factor measured directly for every scan. For these reasons we carried out our calibration procedures using radiometer $\tau's$. Values obtained for opacity calibration and flux correction are used in every step of the reduction explained in the next section.

3.2 Iterative Reduction

Our BoA reduction is based on the scripts presented in the BoA User and Reference Manual (Schuller et al. 2008) and the indications in Section 3 of Belloche et al. (2011). As the sample consists of faint and extended sources, we made the reduction in an iterative process with a signal-to-noise mask. After the first reduction is completed, the next iteration is done with a previous flagging of data points in the first map with a signal-to-noise (S/N) above a certain threshold ($\sim$3.5), and only those data points are reduced in this new iteration. With this process we are reducing only the regions in the map where the real source is, increasing the signal and therefore the S/N. This iteration is repeated 2 or 3 times depending on the source, and after each iteration data points are unflagged in order to recover all the data for the next iteration. The following iterations use a subtraction instead of a flagging process, where a S/N mask is created from iteration i with all data points with S/N < 3.5 set to 0, therefore containing only data points of the source. This mask is subtracted from the real data before iteration *i+1*, in order to subtract the source from the data and leave only the "sky" for the *i+1* reduction. With this we decrease the sky emission and increase the S/N. The source mask is added back to the data before iteration *i+2*.

We repeat this process nearly 10 times or more depending on the source, finally yielding in 10' x 10' to 20' x 20' maps with a 22.4" beamsize. Figures 3.3 through 3.6 present such maps. A detailed explanation of the entire procedure with the reduction scripts can be found in Appendix A.

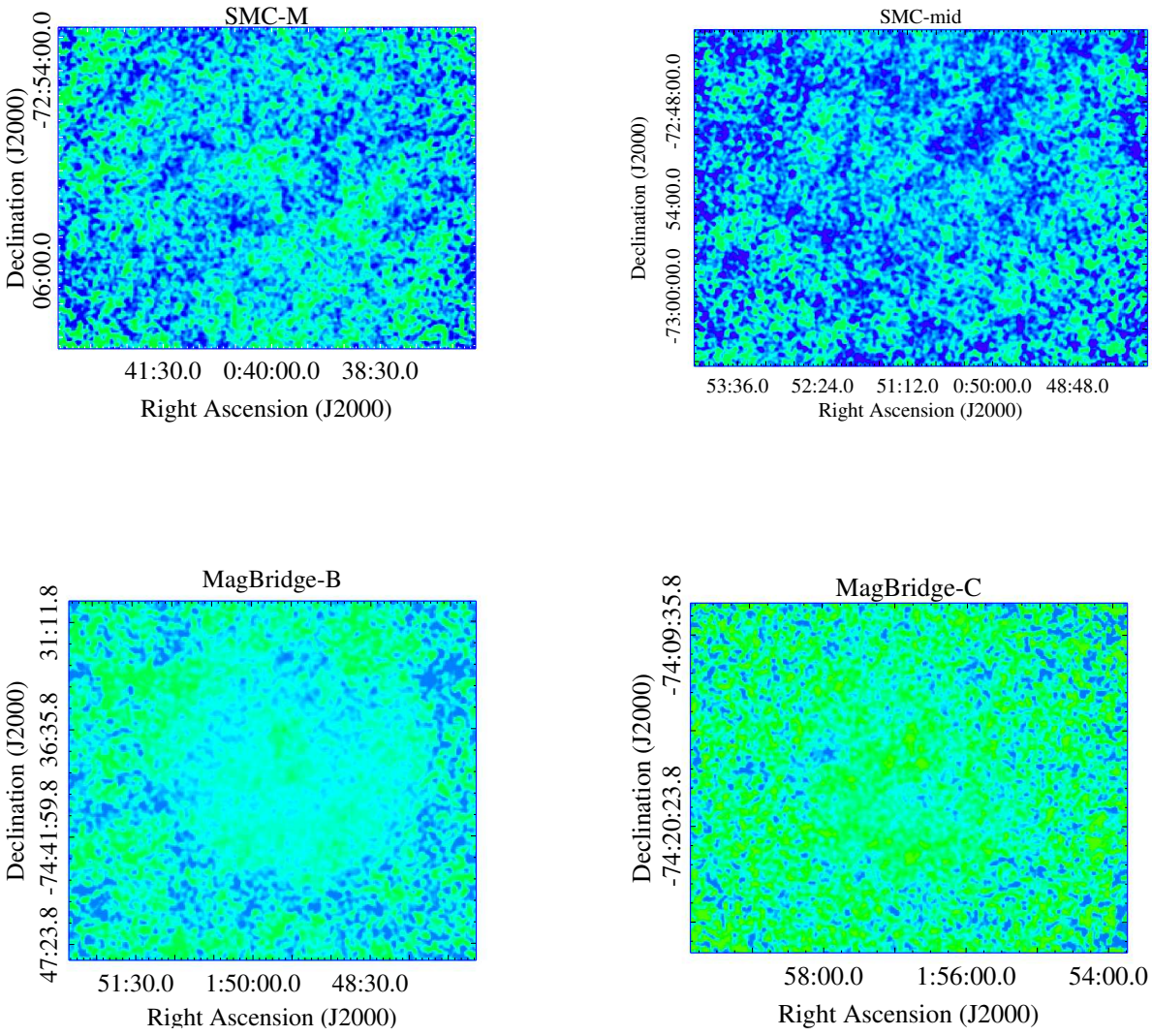

Figure 3.3: LABOCA maps of SMC and Magellanic Bridge sources in the sample (no detections). See Table 2.1 for rms values.

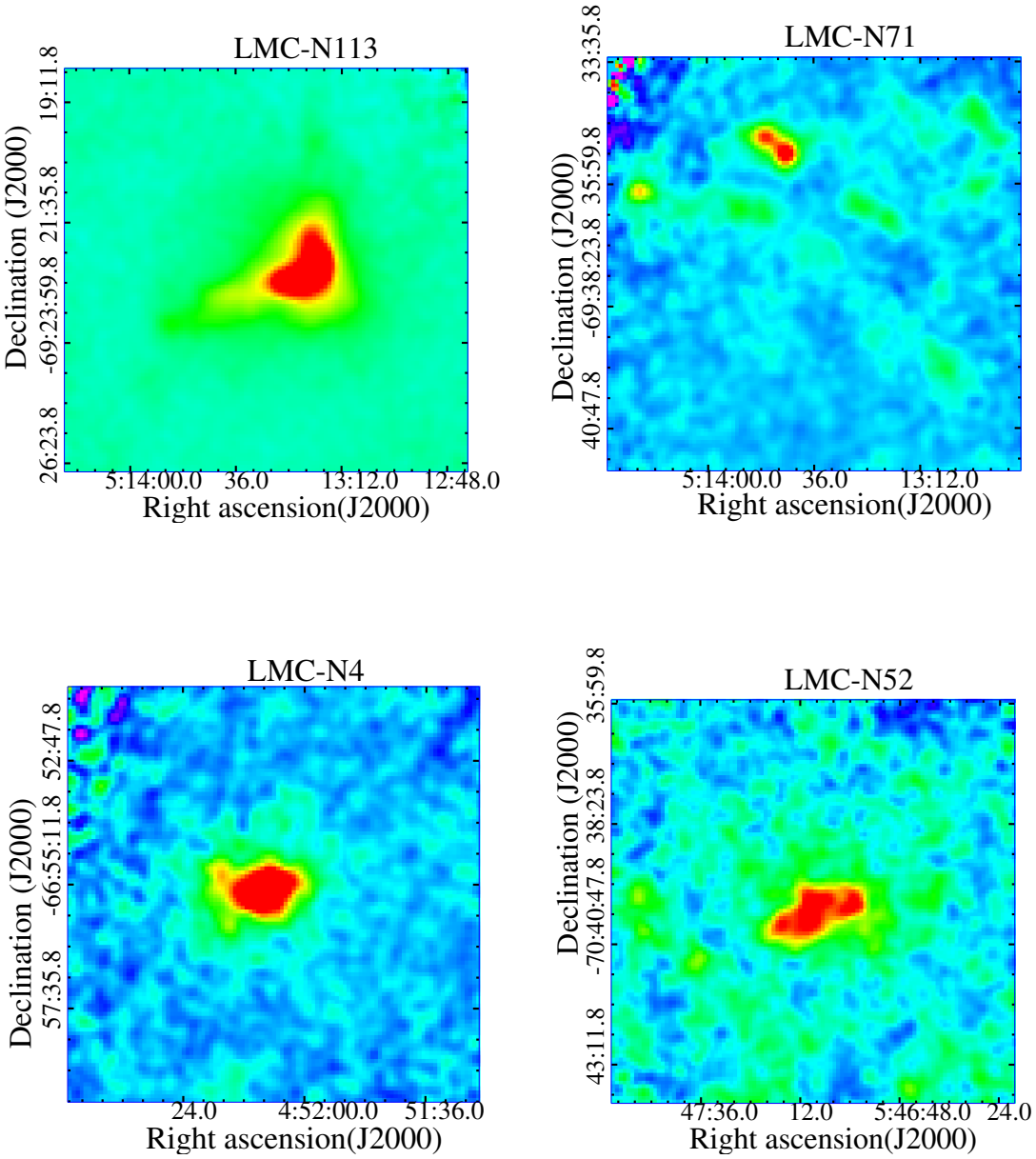

Figure 3.4: LABOCA maps of LMC sources in the sample. See Table 2.1 for rms and S/N values.

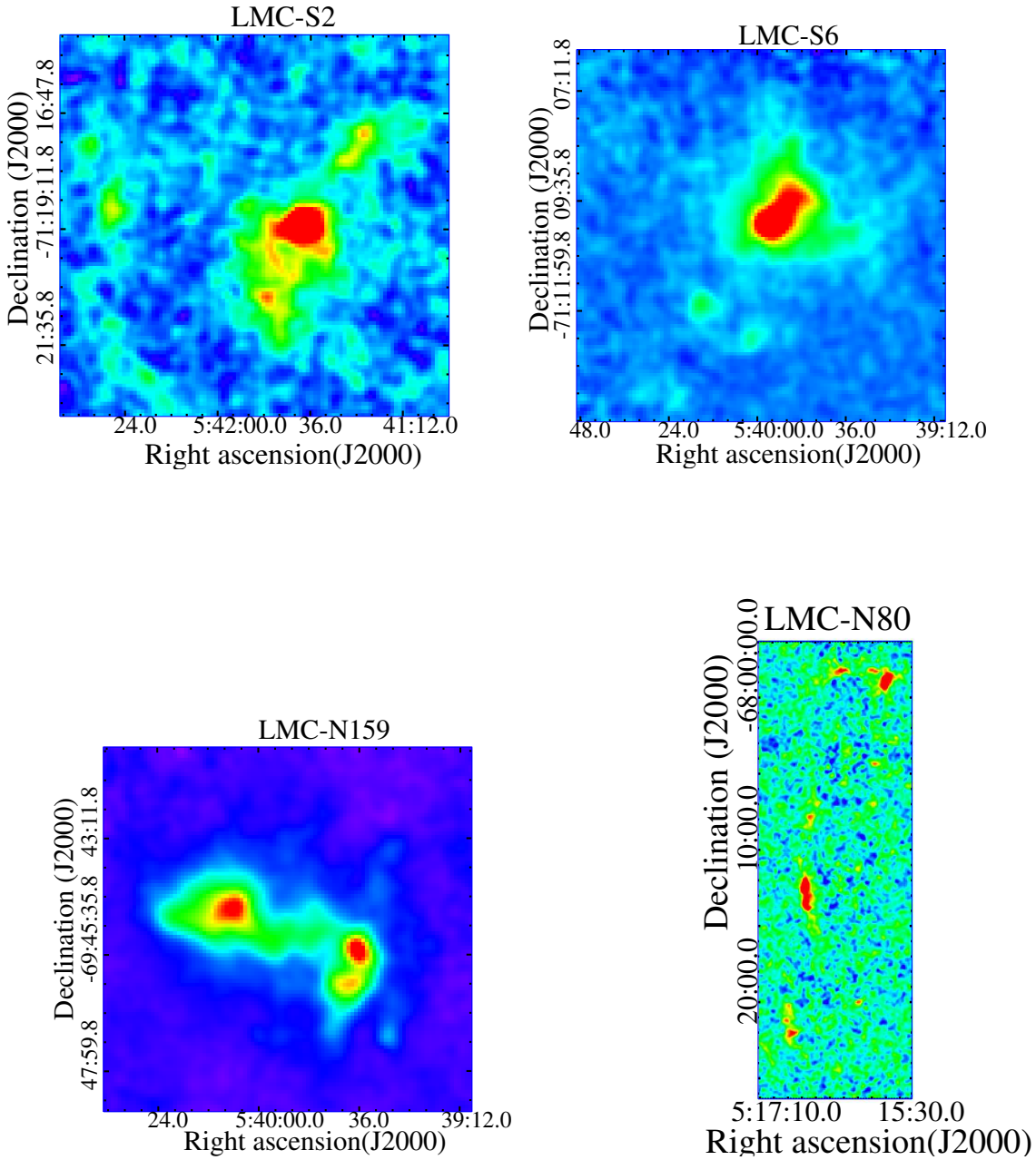

Figure 3.5: LABOCA maps of LMC sources in the sample. See Table 2.1 for rms and S/N values

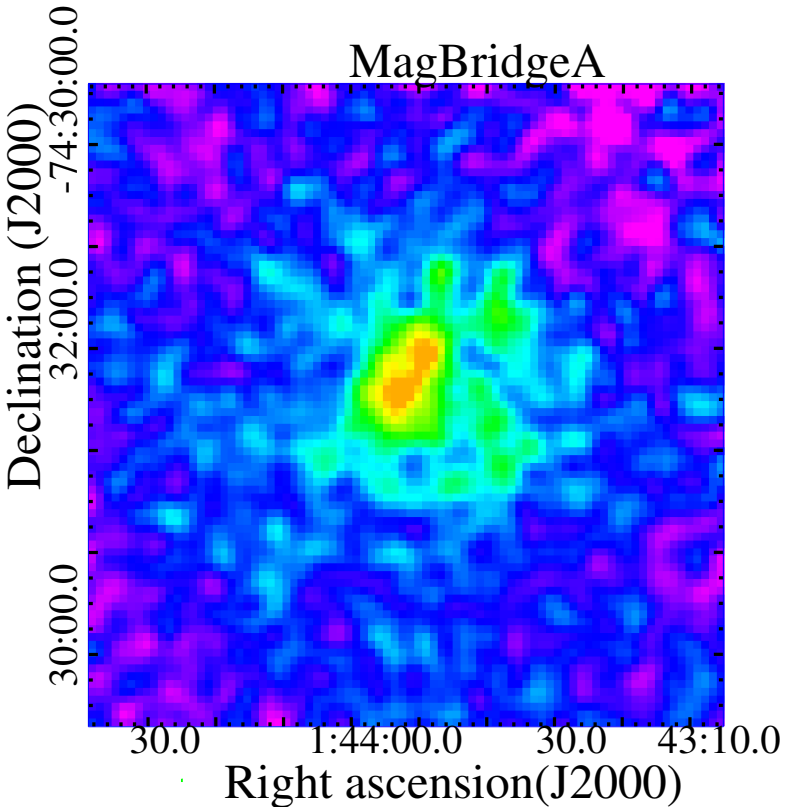

Figure 3.6: LABOCA map of MagBridgeA. See Table 2.1 for rms and S/N values

Chapter 4

Results

At 870 μm there is more than one emission mechanisms, not only dust. In the following, we will describe emission mechanisms of free-free emission and CO emission, along with their subtraction to the dust emission.

Also in this chapter, we will describe the photometry process used to obtain flux densities at different wavelenghts for all the sources in the sample, in order to construct spectral energy distributions. Finally we will explain the fitting procedure of a blackbody law to the spectral energy distributions and the parameters obtained from the fit: spectral emissivity index, dust temperature and dust opacity.

4.1 Free-Free Contribution

Free-Free emission or Bremsstrahlung emission is produced by the acceleration of a free charged particle in the electric field of another free charged particle. Given that they are free particles, their energy states are not quantized and the radiation resulting from the changes in kinetic energy is continuum along the entire spectrum. Therefore this radiation can contribute to the dust continuum emission, so to avoid a possible overestimation of dust mass from dust continuum emission, free-free emission must be removed at every wavelength under consideration. For the free-free emission we used ATCA radio-continuum maps at 8.6 GHz of the entire LMC and SMC with a beamsize of $22''$(Dickel et al. 2010). we divides these maps into smaller maps, one for each source, and convolved them to the LABOCA $22.4''$ beamsize resolution. This convolution was done with a 2-dimensional gaussian kernel:

$$G(x,y) = Aexp\left(-\frac{x^2+y^2}{2\sigma^2}\right) \tag{4.1}$$

where $x^2 + y^2$ is the squared distance of each pixel of the kernel to the central pixel in arcsec units, A is a normalization constant and σ is the gaussian dispersion related with the full width at half maximum (FWHM) θ as

$$\theta = 2\sqrt{2ln(2)}\sigma \tag{4.2}$$

The convolution of 2 functions is given by the relation

$$(I * G)(x, y) = \int \int I(x', y') G(x - x', y - y') dx' dy' \tag{4.3}$$

where in our case the function $I(x, y)$ corresponds to the image of best resolution, $G(x, y)$ the convolution function and the variable x' and y' the pixels coordinates in the image. The convolution is done with the 'convolve2d' task of the 'stsci' library of python. The detailed script is presented in Appendix B.

Then, the ATCA convolved images are projected to the LABOCA coordinate grid so every pair of corresponding pixels in both images actually have the same celestial coordinates. Finally we transformed these radio-continuum maps (originally at 8.6 GHz) to a 345 GHz emission with a $S_\nu \propto \nu^{-0.1}$ law for an optically thin region and then subtracted them to the LABOCA maps. This subtraction is only possible because both ATCA and LABOCA maps now have the same resolution and coordinate grid. A complete description of this image proccesing is explained in Appendix A.2 with the scripts written in python.

Additionally, we measured the free-free contributions for each source to know exactly how much free-free emission we were subtracting to the LABOCA images. We did this directly on the ATCA image using a photometric technique described in the following section (which will be the same photometry used in the entire work). Table 4.4 and Figure 4.4 present the results of these contributions, where it can be seen that they do not represent a contribution of more than 5% in most cases.

4.2 Aperture Photometry

To measure the flux density coming from every source in the sample, we made an aperture photometry using the 'qphot' task in the 'digiphot.apphot' package of IRAF. An example of the parameters given to the task is presented in Appendix C. After analyzing each LABOCA map, for each source we chose an aperture radius to enclosure the source and an appropriate radius and width for a concentric ring to measure the sky emission. Along with the image coordinates these parameters are given to 'qphot' which sums the intensity of each pixel inside the aperture and measures the average value between the pixels inside the sky ring (annulus) to use it as the sky emission value. The photometry result is the sum of all pixels inside the aperture minus the area of the annulus ring times the sky value. Figures 4.1 and 4.2 and Table 4.1 present the chosen radius for the photometry.

Each pixel in the LABOCA maps have units of Jy/beam, which are units of specific intensity I_ν (Intensity measured at a given frequency) and therefore the photometry result corresponds to an intensity value. The *beam* is related to a solid angle but is not a physical unit. To translate this intensity value of Jy/beam to a flux measurement we need to multiply by the solid angle of one pixel in units of the beam solid angle, which can be approximated to a gaussian beam:

$$F_\nu = I_\nu \cdot \frac{\Omega_{pixel}}{\Omega_{beam}} = I_\nu \cdot \frac{CDELT^2}{1.133 \cdot FWHM^2} \tag{4.4}$$

where CDELT is the width of one pixel in arcsec units and FWHM is the full width at half maximum of the image, also in arcsec units.

Table 4.1. Photometry parameters. Since N80-N and N80-NE are so close to each other, sky level for these sources was measured in an annulus of $2.5'$ width placed in a region close to them (See Figure 4.1 (h)). For the same reason, sky level for N159 sources was measured in an annulus of $0.4'$ width in a close region (See Figure 4.1 (g)).

Source	$R_{aperture}[']$	$R_{annulus}[']$	$dannulus\ [']$
IRAS2	0.7	1.5	0.5
hodge15	1.0	1.3	0.7
SMC-SW-1	0.6	0.8	0.4
SMC-SW-2	0.6	1.2	0.3
SMC-SW-3	1.0	1.2	0.5
SMC-SW-4	0.8	1.0	0.5
SMC-SW-5	0.7	1.0	0.5
SMC-SW-6	0.7	1.0	0.5
SMC-SW-7	0.8	1.0	0.5
SMC-SW-8	0.9	1.2	0.5
SMC-SW-9	1.0	1.5	0.5
MagBridgeA	1.5	3.0	0.5
LMC-N159E	1.5	...	...
LMC-N159W	1.0	...	...
LMC-N159S	1.2	...	...
LMC-N113	3.5	4.0	0.7
LMC-N71	1.0	2.0	0.3
LMC-N80-N	1.3	...	...
LMC-N80-NE	1.3	...	...
LMC-N80-M	2.6	3	1
LMC-N80-S	2.6	3	1.5
LMC-N4	3.5	4.0	0.5
LMC-S2	5.5	6.5	1.4
LMC-S6	2.8	3.5	0.5
LMC-N52	1.5	2.0	0.5
LMC-N83A	0.5	0.7	0.2
LMC-N83B	0.4	0.5	0.2
LMC-N84A	0.7	0.8	0.2
LMC-N84B	1.0	1.2	0.3

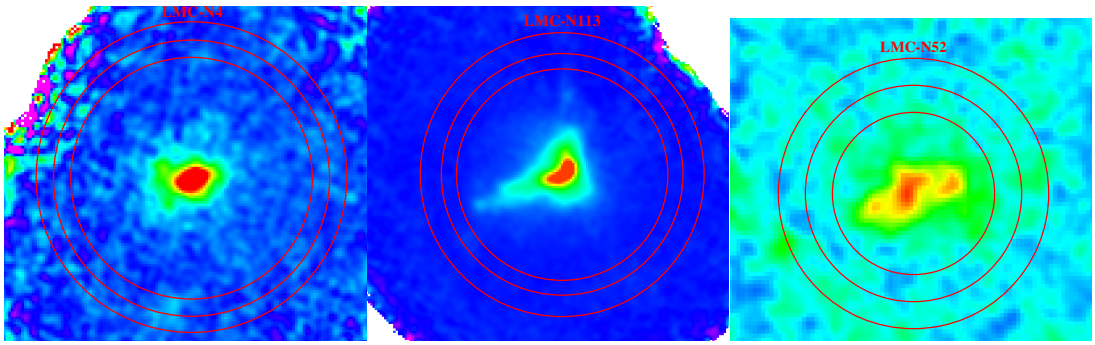

(a) LMC-N4 **(b)** LMC-N113 **(c)** LMC-N52

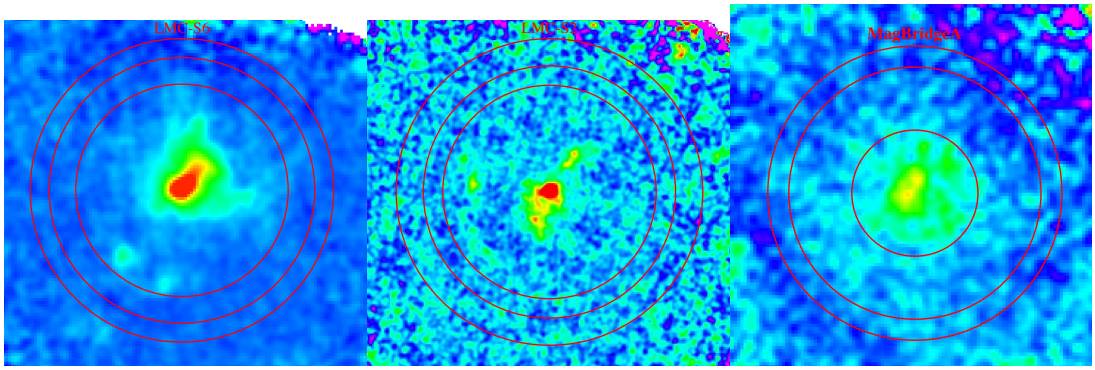

(d) LMC-S6 **(e)** LMC-S2 **(f)** MagBridgeA

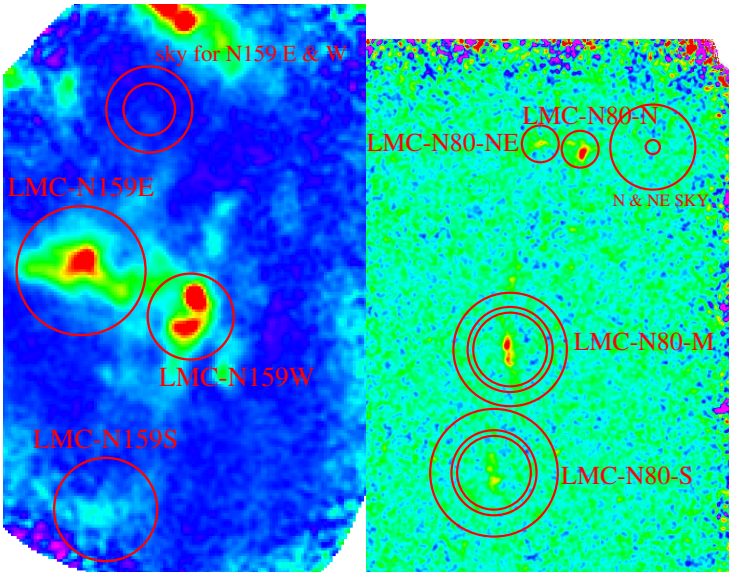

(g) LMC-N159 **(h)** LMC-N80

Figure 4.1: Photometry apertures

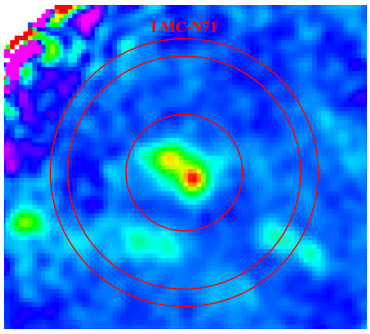

(a) LMC-N71

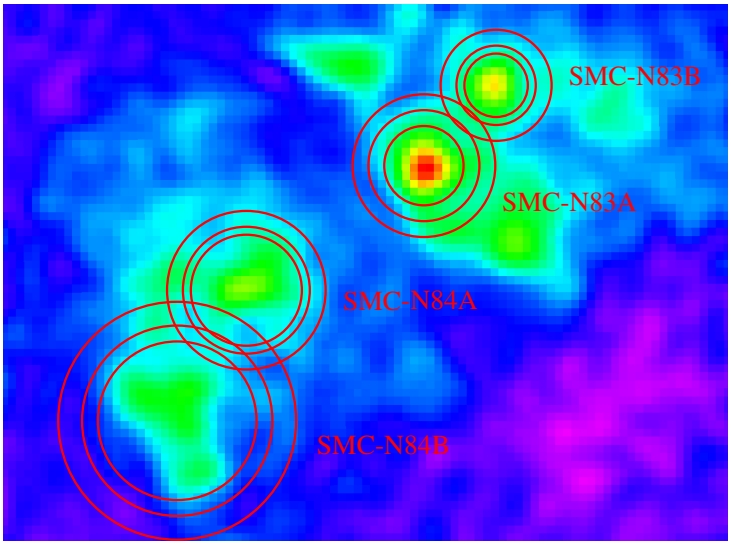

(b) SMC-N83 & SMC-N84

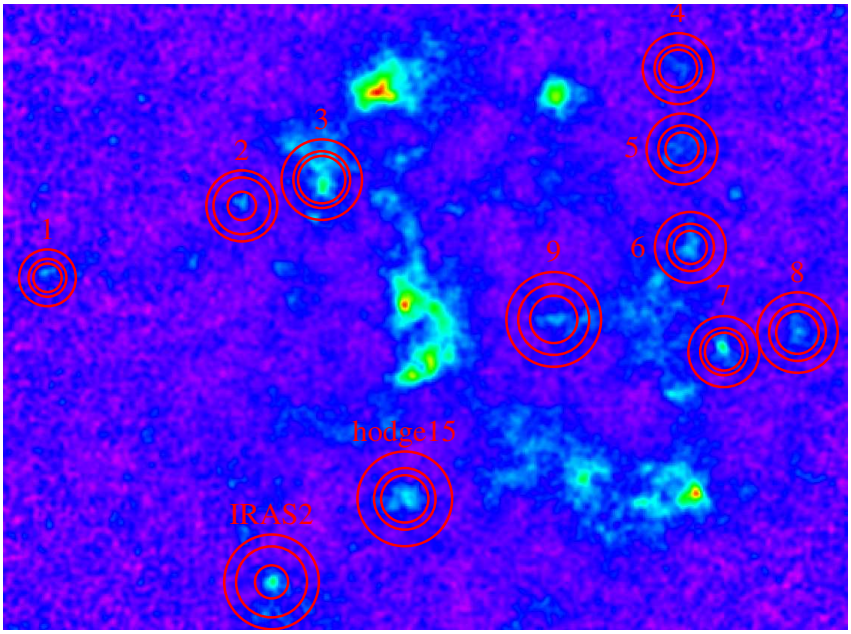

(c) SMC-SW region

Figure 4.2: Photometry apertures

Table 4.2. Conversion Factors from intensity (I_ν) to flux units (S_ν)

image	conversion factor
70 μm SPITZER (SMC)	$5.8 \cdot 10^{-4}$
70 μm SPITZER (LMC)	$6.0 \cdot 10^{-3}$
100 μm HERSCHEL (SMC & LMC)	$9.4 \cdot 10^{-5}$
160 μm HERSCHEL (SMC & LMC)	$2.1 \cdot 10^{-4}$
160 μm SPITZER (SMC)	$5.8 \cdot 10^{-4}$
160 μm SPITZER (LMC)	$6.0 \cdot 10^{-3}$
250 μm HERSCHEL (SMC & LMC)	$8.5 \cdot 10^{-4}$
350 μm HERSCHEL (SMC & LMC)	$2.4 \cdot 10^{-3}$
500 μm HERSCHEL (SMC & LMC)	$4.6 \cdot 10^{-3}$
870 μm LABOCA	$3.7 \cdot 10^{-2}$

HERSCHEL and SPITZER images are all in units of MJy/sr, also a unit of specific intensity, so converting their photometry results in units of flux translates into multiply by the area of one pixel in steroradian units. Conversion factors for all the images in the sample are presented in Table 4.2. These factors leave the photometry results in units of Jansky (flux density).

4.3 CO contribution

Motion of molecules in the interstellar medium produce emission at different wavelengths, including the $870\mu m$ window, so molecular emission can increase the emission of dust at $870\mu m$. As discussed in Chapter 1, carbon and oxygen are the two most abundant elements after hydrogen, making CO transition lines most probable. Emission from molecules can be due to electronic transitions from a higher to a lower energy level, vibrational transitions due to a displacement of the nuclei of the molecule from the equilibrium point, and rotational transitions due to a rotation of the nuclei of the molecule with a certain moment of inertia. Of these three types of molecular transitions, the rotational are the ones that need the lowest temperatures to occur, making them the most probable in such low temperature systems as molecular clouds (see Figure 4.3). Of all the CO transitions with wavelengths close enough to a wavelength of this dataset, the most likely is the $CO(3-2)$ at 345 GHz (870 μm), coinciding with the LABOCA frequency. CO data was obtained from Nanten (CO(1-0), $60''$ beamsize) and SEST (CO(2-1), CO(3-2), $22''$ beamsize) surveys and a corresponding ratio of $CO(3-2)/CO(1-0)$ and $CO(2-1)/CO(1-0)$ of $\sim$1 was assumed to estimate the CO(3-2) contribution at 345 GHz. We made an aperture photometry to these images in the same way as for the LABOCA images with free-free contribution subtraction. These contributions turned out to be less than 10% of the 345 GHz emission in most cases (Table 4.3 and Figure 4.4). These CO(1-0) data were used to measure the CO contributions only for the sources with no other CO data of better resolution available. For MagBridgeA, N159, N113, N4 and N52 we used the CO data described in Table 2.3. After subtracting the free-free and CO contributions finally we obtain the emission of pure dust at 870 μ (Table 4.5)

For the sources in the SMC-SW region, since we did not have available CO data for all the

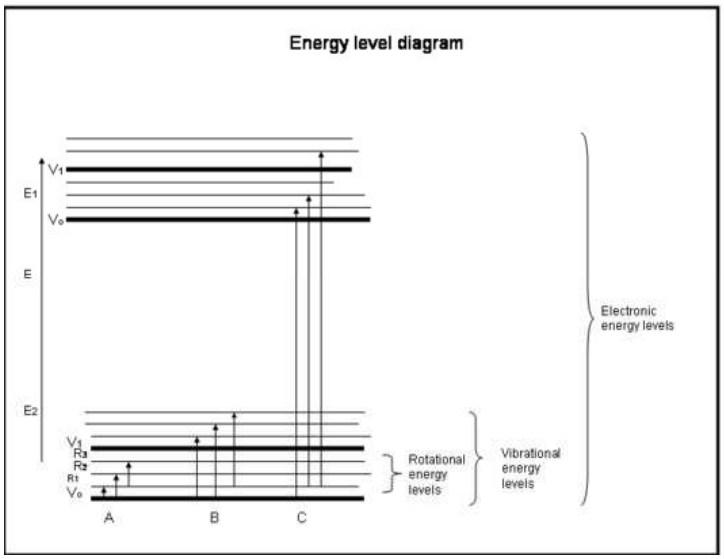

Figure 4.3: Energy level diagram of electronic, vibrational and rotational transitions.

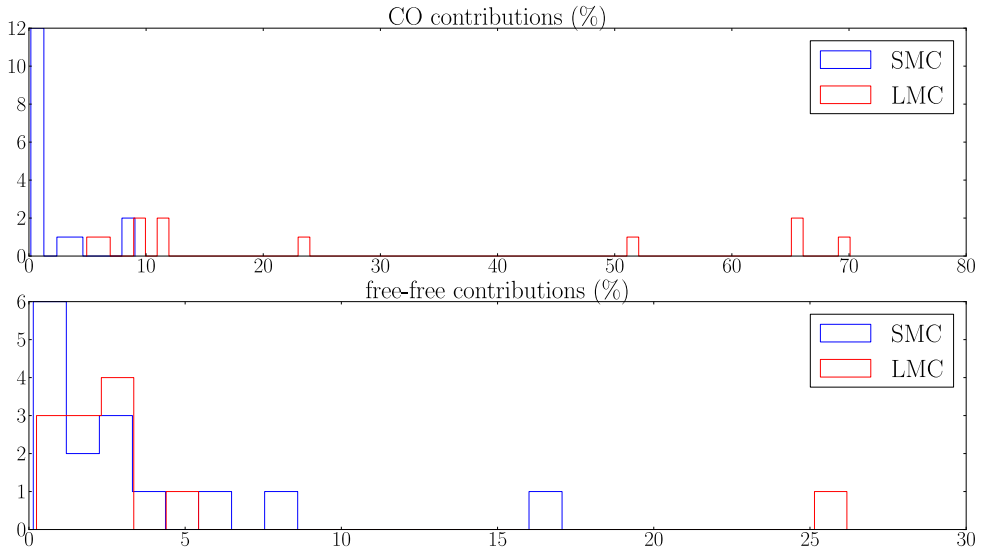

Figure 4.4: Distributions of CO and free-free percentual contributions to dust emission

Table 4.3. CO contributions at 870 μm

Source	$S_{CO}[Jy]$	CO contribution [%]
LMC-N159E	0.84	4.93
LMC-N159W	0.80	9.65
LMC-N113	0.94	6.51
LMC-N71	0.09	11.3
LMC-N80-M	0.59	65.21
LMC-N80-N	0.22	23.28
LMC-N80-NE	0.22	70.09
LMC-N80-S	0.38	51.92
LMC-N4	0.16	6.65
LMC-S2	0.54	11.53
LMC-S6	0.86	8.99
MagBridge A	0.001	0.16
LMC-N52	0.40	66.06
SMC-N83A	0.04	8.34
SMC-N83B	0.03	9.05
SMC-N84A	0.02	2.78
SMC-N84B	0.04	3.85

sources, we used a value of CO contribution of 0.3% as determined in Bot et al. (2010) for other sources in the same SMC-SW region.

4.4 Spectral Energy Distributions

We obtained emission at 70, 100, 160, 250, 350 and 500 μm from the SPITZER and HERSCHEL images by doing photometry in the same way as for the LABOCA maps, with the same angular sizes, and subtracting the free-free emission as explained in the previous section (which turned out to be almost negligible). Table 4.7 presents results at all wavelengths.

We used these flux densities obtained from the photometry (Table 4.7), along with the flux density at 870μm, to construct spectral energy distributions (SED's) for each source in the sample (Figures 4.5 through 4.20).

4.4.1 Fitting Procedure

At millimeter and sub-millimeter wavelenghts we can assume that molecular clouds emit in an optically thin medium, so their power emitted per unir area, frequency and solid angle can be approximated to

$$I_\nu = \tau_\nu B_\nu(T_d) \tag{4.5}$$

Table 4.4. Free-free contributions

Source	$S_{ff}[Jy]$	ff contribution [%]
N113	0.37	2.57
N159E	0.53	3.11
N159S	0.01	2.39
N159W	0.25	3.02
N4	0.63	26.18
N52	0.01	1.99
N80-M	0.02	2.22
N80-NE	0.003	1.06
N80-N	0.01	0.61
N80-S	0.01	1.72
S2	0.22	4.69
S6	0.02	0.24
N83A	0.005	0.90
N83B	0.001	0.42
N84A	0.02	3.57
N84B	0.01	1.24
SWE1	0.01	8.04
SWE2	0.01	5.78
SWE3	0.01	2.43
SWE4	0.03	17.06
SWE5	0.0003	0.14
SWE6	0.002	0.70
SWE7	0.01	2.79
SWE8	0.002	0.80
SWE9	0.001	0.21
hodge15	0.01	1.97
IRAS2	0.01	3.16

Table 4.5. Flux densities measured from the photometry at 870 μm.

Source	$S_{870\mu m}$ [Jy]
IRAS2	0.23 ± 0.05
hodge15	0.30 ± 0.06
SMC-SW-1	0.07 ± 0.01
SMC-SW-2	0.10 ± 0.02
SMC-SW-3	0.37 ± 0.07
SMC-SW-4	0.13 ± 0.03
SMC-SW-5	0.19 ± 0.04
SMC-SW-6	0.24 ± 0.05
SMC-SW-7	0.26 ± 0.05
SMC-SW-8	0.29 ± 0.06
SMC-SW-9	0.27 ± 0.05
LMC-N159E	16.20± 3.24
LMC-N159W	7.76 ± 1.55
LMC-N159S	0.09 ± 0.01
LMC-N113	13.3 ± 2.7
LMC-N71	0.76 ± 0.2
LMC-N80-M	0.89 ± 0.18
LMC-N80-NE	0.32 ± 0.06
LMC-N80-N	0.74 ± 0.15
LMC-N80-s	0.34 ± 0.09
LMC-N4	1.6 ± 0.3
LMC-S2	4.23 ± 0.85
LMC-S6	9.13 ± 1.83
MagBridgeA	0.59 ± 0.12
LMC-N52	0.50 ± 0.10
SMC-N83A	0.46 ± 0.09
SMC-N83B	0.26 ± 0.05
SMC-N84A	0.62 ± 0.12
SMC-N84B	0.99 ± 0.20

Table 4.6. Flux calibration errors

Image	σ [%]
$100\mu m$ PACS	10
$160\mu m$ PACS	20
$70, 160\mu m$ MIPS	10
$250, 350, 500\mu m$ SPIRE	7
$870\mu m$ LABOCA	20
CO(1-0) NANTEN	40
8.6GHz ATCA	20

Table 4.7. Dust emission. Flux densities for all sources at different wavelengths.

Source	$S_{70\mu m}$ [Jy]	$S_{100\mu m}$ [Jy]	$S_{160\mu m}$ [Jy] (SPITZER)	$S_{160\mu m}$ [Jy] (HERSCHEL)	$S_{250\mu m}$[Jy]	$S_{350\mu m}$[Jy]	$S_{500\mu m}$[Jy]	$S_{870\mu m}$[Jy]	$S_{1.2mm}$[Jy]
IRAS2	7.49±0.75	9.20±0.92	4.33±0.43	8.62±1.72	4.67±0.33	1.91±0.13	0.78±0.05	0.23±0.05	···
hodge15	2.33±0.23	4.73±0.47	3.61±0.36	6.31±1.26	4.56±0.32	2.65±0.19	1.15±0.08	0.30±0.06	···
SMC-SW-1	2.80±0.28	3.92±0.39	1.13±0.11	3.38±0.68	1.81±0.12	0.80±0.06	0.33±0.02	0.07±0.01	···
SMC-SW-2	3.94±0.39	5.73±0.57	2.15±0.22	4.72±0.94	2.60±0.18	0.77±0.08	0.43±0.03	0.10±0.02	···
SMC-SW-3	7.37±0.74	13.74±1.37	8.12±0.81	12.61±2.52	8.18±0.57	3.23±0.23	1.41±0.10	0.37±0.07	···
SMC-SW-4	4.82±0.48	6.74±0.67	3.14±0.31	5.53±1.11	2.78±0.19	1.26±0.09	0.35±0.02	0.13±0.03	···
SMC-SW-5	0.95±0.10	2.02±0.20	1.75±0.16	3.25±0.65	2.37±0.17	1.09±0.08	0.44±0.03	0.19±0.04	···
SMC-SW-6	2.25±0.22	5.24±0.52	2.56±0.26	7.07±1.41	4.59±0.32	14.06±0.14	0.81±0.06	0.24±0.05	···
SMC-SW-7	8.15±0.81	11.46±1.15	4.38±0.44	9.50±1.90	5.10±0.36	2.18±0.15	0.68±0.05	0.26±0.05	···
SMC-SW-8	1.90±0.19	2.83±0.28	1.94±0.19	3.49±0.70	2.25±0.16	1.16±0.08	0.60±0.04	0.29±0.06	···
SMC-SW-9	4.26±0.43	7.99±0.80	6.19±0.62	9.93±1.99	6.45±0.45	2.92±0.20	1.01±0.07	0.27±0.05	···
LMC-N159E	285.48±25.55	885.38±88.854	410.93±41.09	571.59±114.32	247.88±17.35	106.99±7.49	37.41±2.62	16.20±3.24	1.31±0.13
LMC-N159W	178.88±17.89	629.36±62.94	96.76±9.68	445.37±89.07	185.15±18.52	74.06±5.18	25.90±1.81	7.76±1.55	1.13±0.11
LMC-N159S	0.35±0.04	2.27±0.23	2.73±0.27	4.23±0.85	3.77±0.26	1.77±0.12	0.67±0.05	0.22±0.04	0.09±0.01
LMC-N113	323.0±32.3	824.5±82.4	501.0±50.1	674.7±134.9	315.5±22.1	135.4±9.5	52.9±3.7	13.3±2.7	···
LMC-N71	15.2±1.5	44.8±4.5	15.4±1.5	37.1±7.4	17.3±1.2	7.0±0.5	2.8±0.2	0.76±0.2	···
LMC-N80-M	3.49±0.35	3.22±0.32	13.02±1.30	12.85±2.57	12.72±0.89	7.28±0.51	3.16±0.22	0.89±0.18	···
LMC-N80-NE	3.96±0.40	7.85±0.78	19.82±1.98	13.41±2.68	11.34±0.79	6.92±0.48	3.49±0.24	0.32±0.06	···
LMC-N80-N	9.93±0.99	15.35±1.53	32.90±3.29	24.46±4.89	16.74±1.17	9.26±0.65	4.44±0.31	0.74±0.15	···
LMC-N80-s	4.28±0.43	7.99±0.80	26.12±2.61	26.26±5.25	22.26±1.59	12.20±0.85	6.04±0.42	0.34±0.09	···
LMC-N4	103.5±10.3	299.6±30.0	190.1±19.0	257.0±51.4	127.9±9.0	56.8±4.0	22.7±1.6	1.6±0.3	···
LMC-S2	124.04±12.40	230.43±23.04	221.38±22.14	249.76±49.95	140.92±9.86	62.69±4.39	25.33±1.77	4.23±0.85	···
LMC-S6	83.42±8.34	182.78±18.28	153.11±15.31	193.07±38.61	116.76±8.17	56.74±3.97	23.61±1.65	9.13±1.83	···
MagBridgeA	1.12±0.11	1.29±0.13	1.82±0.18	1.99±0.40	1.71±0.12	0.86±0.06	0.35±0.02	0.59±0.12	···
LMC-N52	0.64±0.10	3.40±0.30	6.90±0.70	7.80±1.60	7.60±0.50	3.60±0.30	1.60±0.10	0.50±0.10	···
SMC-N83A	13.35±1.34	14.54±1.45	18.32±1.83	14.33±2.87	8.40±0.59	3.74±0.26	1.32±0.09	0.46±0.09	···
SMC-N83B	13.75±1.37	10.94±1.09	10.89±1.09	9.92±1.98	5.51±0.39	3.28±0.23	1.17±0.08	0.26±0.05	···
SMC-N84A	17.40±1.74	15.23±1.52	15.96±1.60	12.67±2.59	7.56±0.53	3.28±0.23	1.44±0.11	0.62±0.12	···
SMC-N84B	23.05±2.30	29.95±2.99	36.68±3.68	27.78±5.56	16.39±1.15	7.61±0.53	2.72±0.19	0.99±0.20	···

where τ_ν is the optical depth of the molecular cloud and $B_\nu(T_d)$ is Planck's law at a dust temperature. The optical depth of the cloud is

$$\tau_d(\nu) = \kappa_d(\nu) \int \rho dl = \kappa_d(\nu)\Sigma_d \tag{4.6}$$

with $\kappa_d(\nu)$ the absorption coefficient per unit dust mass in $\left[cm^2 g^{-1}\right]$, ρ the gas density in $\left[g\ cm^{-3}\right]$, $\int dl$ is the integral in the line of sight and Σ_d the dust surface mass density in $\left[g\ cm^{-2}\right]$. So

$$I_\nu = \kappa_d(\nu)\Sigma_d B_\nu(T_d) \tag{4.7}$$

Integrating this last equation in the solid angle of the source (Ω)

$$S_\nu = \Omega\kappa_d(\nu)\Sigma_d B_\nu(T_d) \tag{4.8}$$

Now, the absorption coefficient is empirically found to depend on the frequency and the adimensional coefficient β related to chemical composition of dust grains and their size distribution, known as the spectral emissivity index (Hildebrand 1983)

$$\kappa_\nu = \kappa_{\nu_0} \left(\frac{\nu}{\nu_0}\right)^\beta \tag{4.9}$$

where κ_{ν_0} is the absorption coefficent at the frequency ν_0. Including this in (4.8)

$$S_\nu = \Omega\Sigma_d\kappa_{\nu_0} \left(\frac{\nu}{\nu_0}\right)^\beta B_\nu(T_d) \tag{4.10}$$

By identifying the constant values Ω, Σ_d, κ_{ν_0} and ν_0 we see that the flux density depends only on the frequency, β and the dust temperature T_d as

$$S_\nu \propto \nu^\beta B_\nu(T_d) \tag{4.11}$$

where β is normally found to be a value between 1 and 2. According to this and assuming a single temperature component, we fitted a simple modified blackbody law to the SED's. A dust model was not fitted since it is beyond the scope of this work. The fitted law is

$$S_\nu = C \cdot \nu^\beta B_\nu(T_d) \tag{4.12}$$

where C is a constant of proportionality. C, β and T_d where left as free parameters in the fit, using a χ^2 minimization.

$$\chi^2 = \frac{(S_{\nu_{obs}} - S_{\nu_{model}})^2}{\sigma^2_{S_{\nu_{obs}}}} \tag{4.13}$$

where $S_{\nu_{obs}}$ is the observed flux density measured from the photometry, $S_{\nu_{model}}$ is the flux density fitted according to equation (4.12) and $\sigma_{S_{\nu_{obs}}}$ is the error associated to the observed flux density $S_{\nu_{obs}}$. Errors of the flux densities in the SED's are associated with a flux calibration error for each image in the data set (Table 4.6). Errors from the photometry process or the CO and free-free contribution subtraction are negligible compared to flux calibration errors. The modified blackbody law of equation (4.12) fits only the points at 100, 160, 250, 350 and 500 μm, since the points at 70 and 870 μm present excesses of emission (Sauvage et al. 1990, Aguirre et al. 2003) and that will be explained and analysed in Chapter 5. We present SED's for the SMC sources in Figures 4.5 through 4.12, Figure 4.13 for the source in the Magellanic Bridge and Figures

4.14 through 4.20 for sources in the LMC, along with the residuals plots of the fits measured as data/model. In order to be consistent with the units used in this work, the x-axes in the SEDs are presented in micrometer wavelenghts and the y-axes in flux densities (in Jansky) multiplied by the corresponding frequency in GHz. Thus, as $\nu S_\nu = \lambda S_\lambda$, νS_ν can be plotted as a function of ν or λ. By chossing λ we can be consistent with the wavelenght range we have used in our SPITZER-HERSCHEL-LABOCA sample, and by choosing S_ν we are also consistent with flux units of Jy used in this work.

SMC

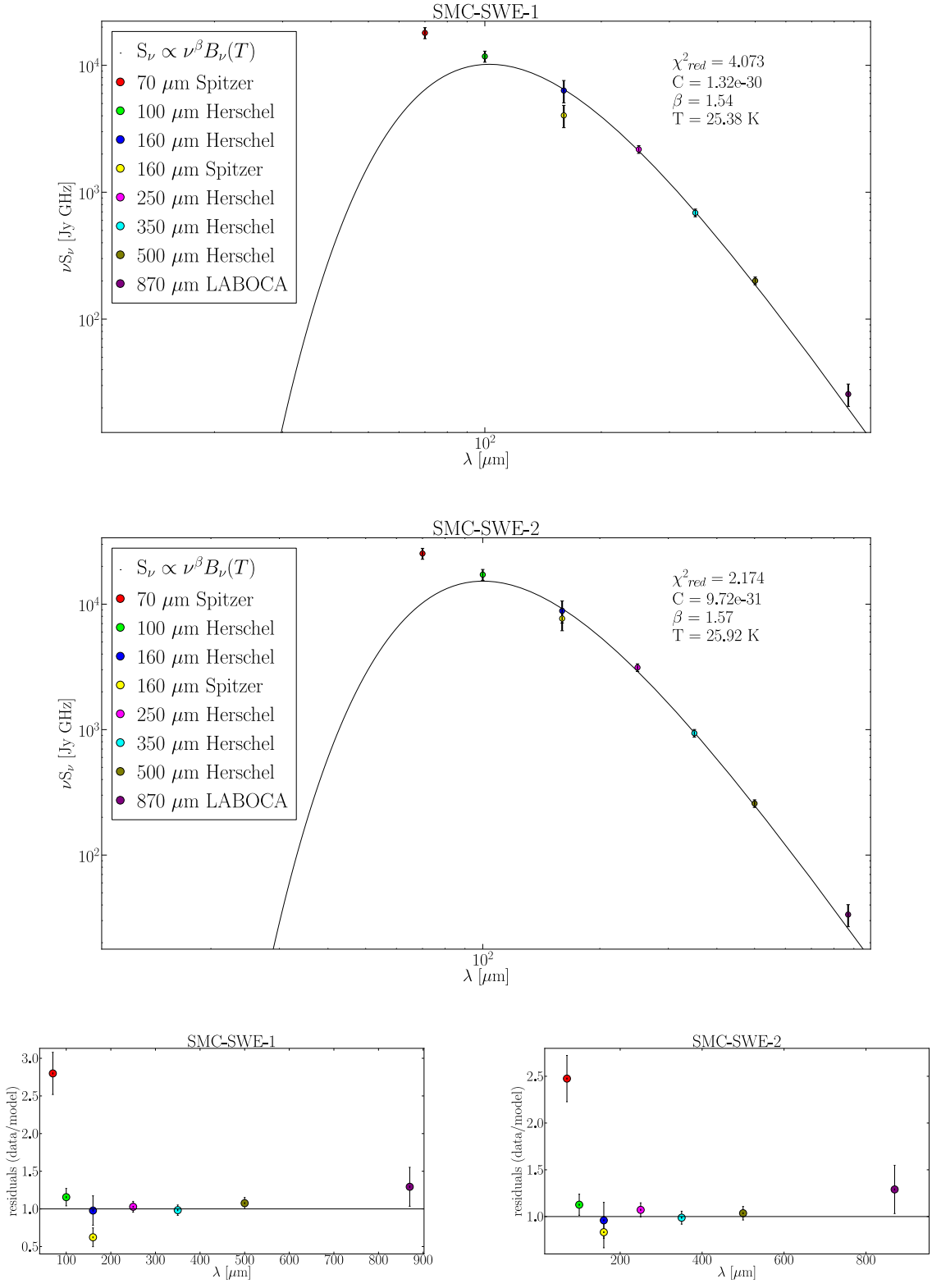

Figure 4.5: SED's for SMC-SWE-1 and SMC-SWE-2 with their corresponding residuals plots.

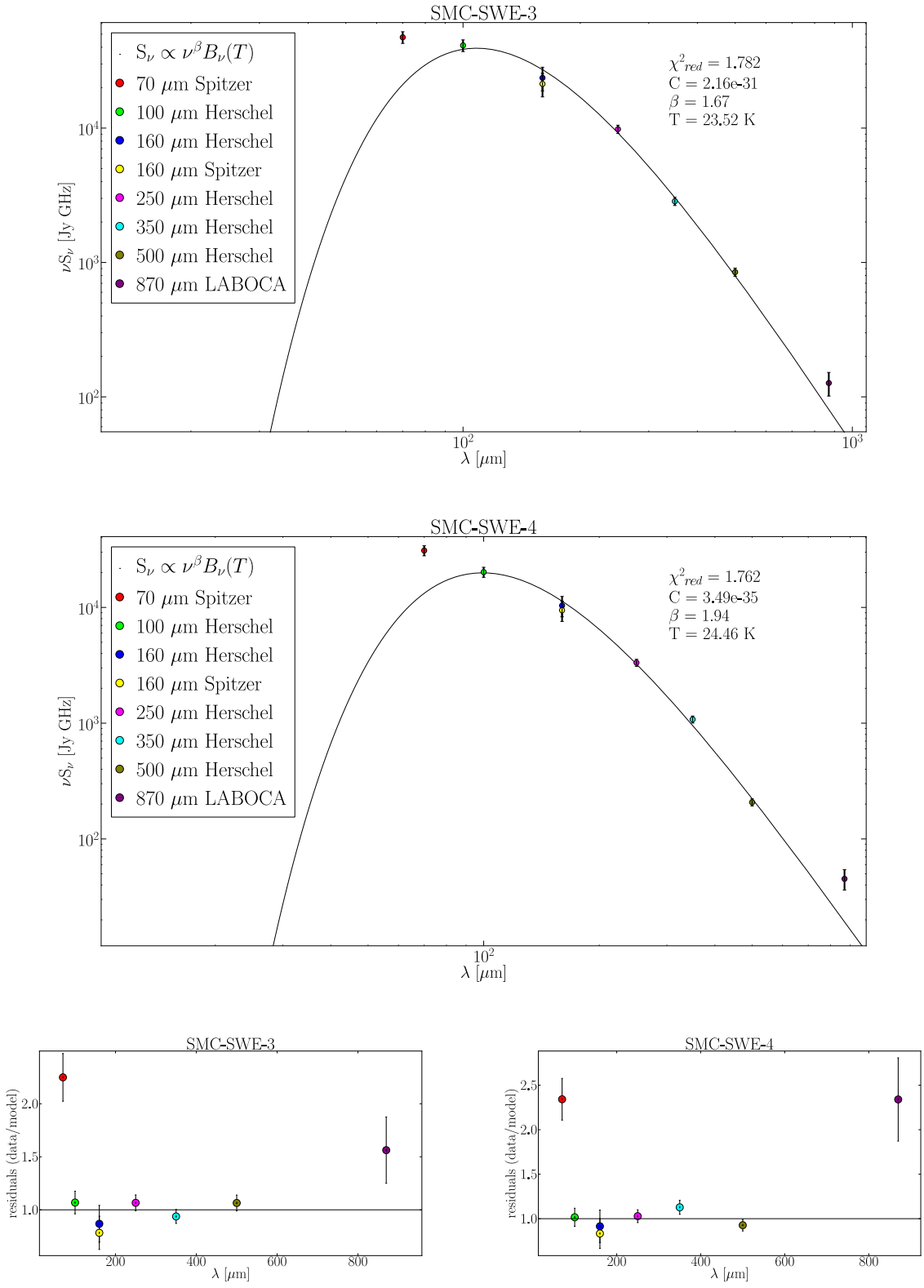

Figure 4.6: SED's for SMC-SWE-3 and SMC-SWE-4 with their corresponding residuals plots.

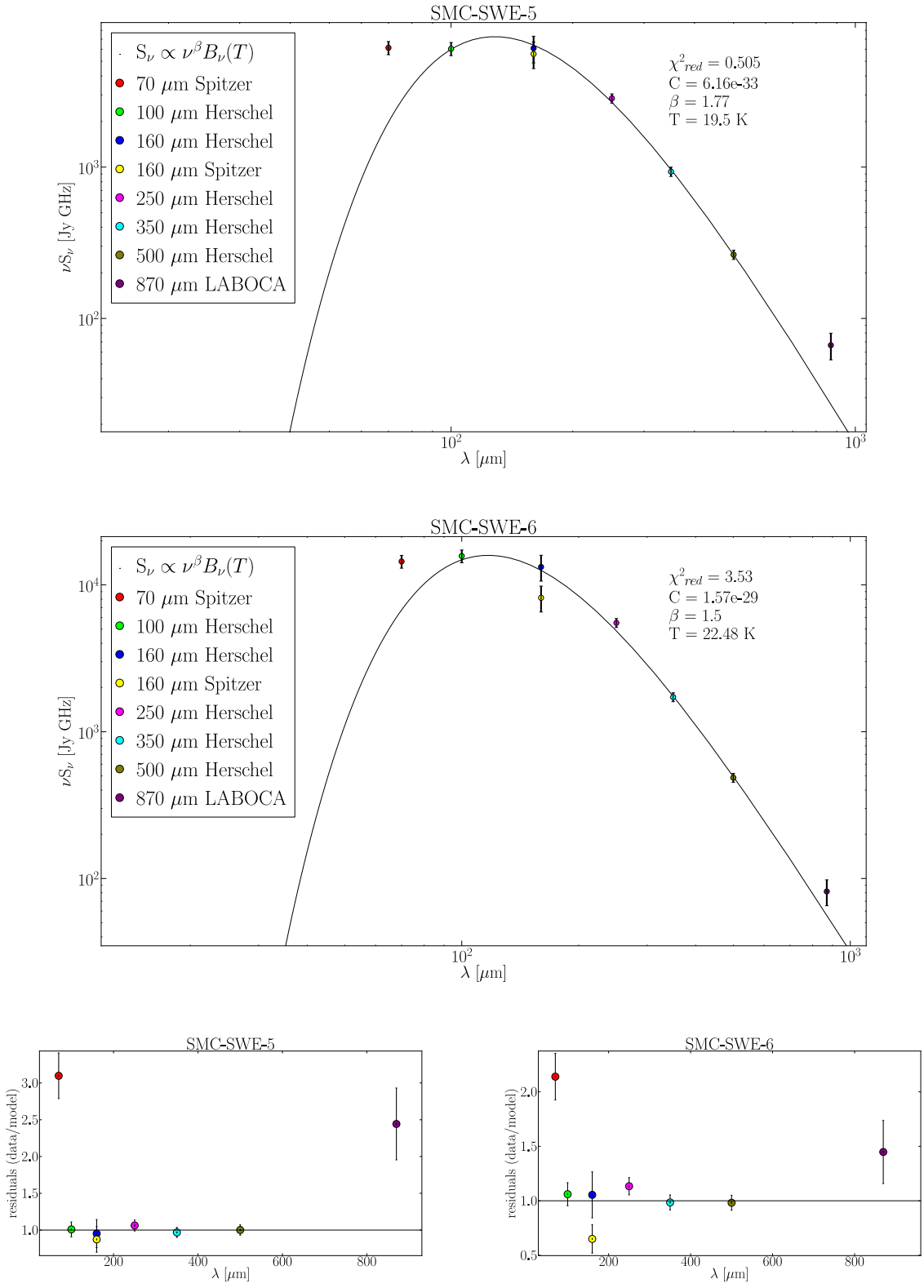

Figure 4.7: SED's for SMC-SWE-5 and SMC-SWE-6 with their corresponding residuals plots.

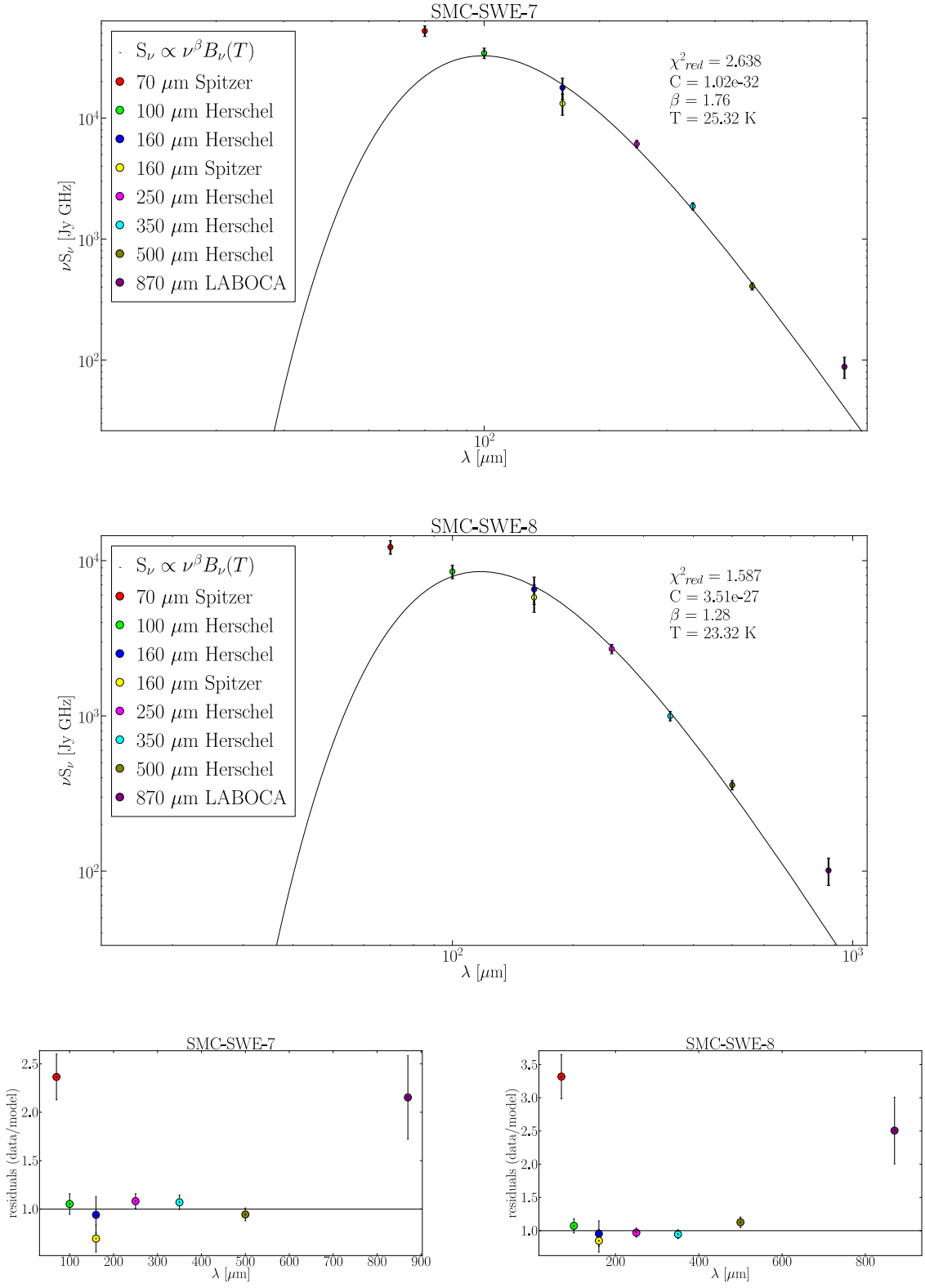

Figure 4.8: SED's for SMC-SWE-7 and SMC-SWE-8 with their corresponding residuals plots.

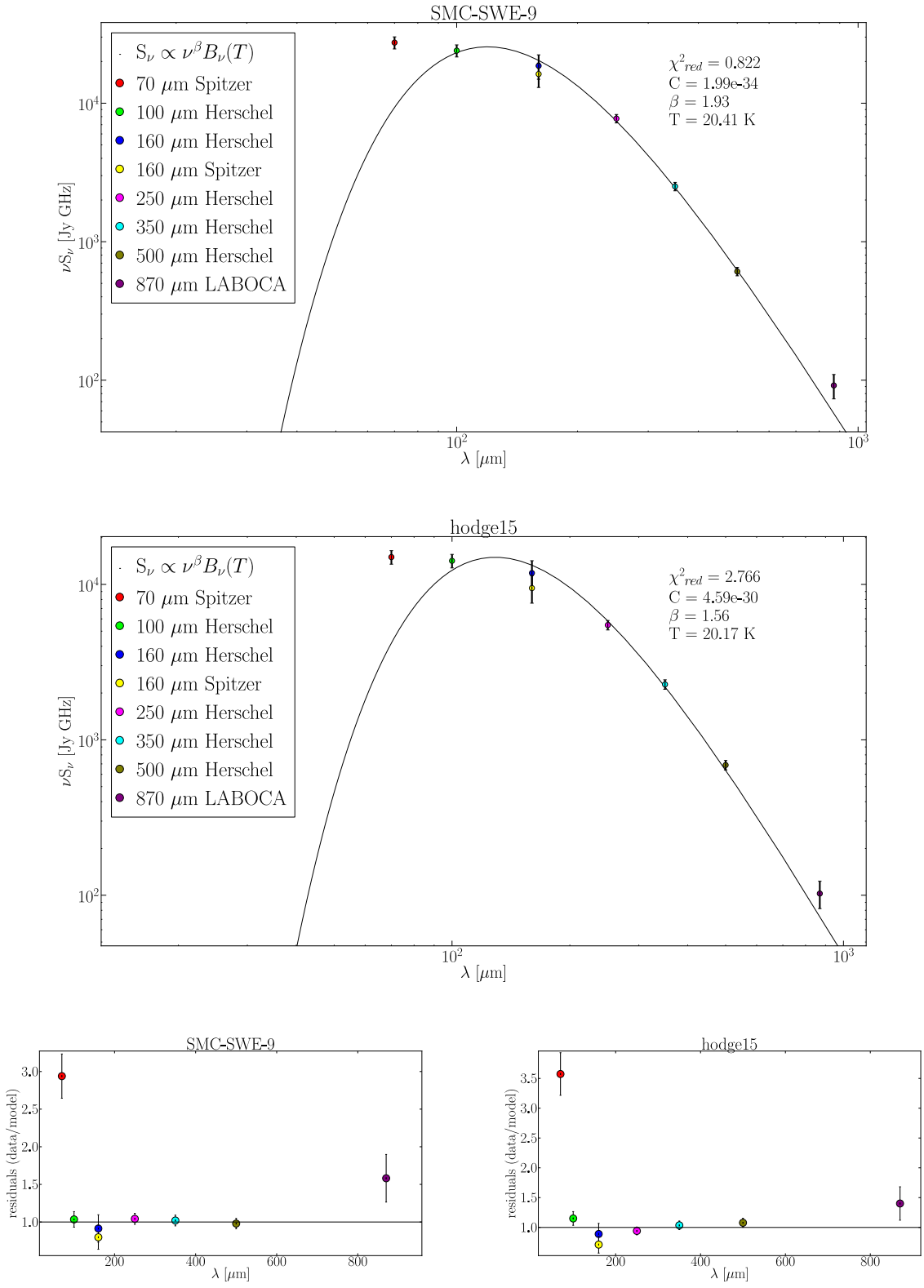

Figure 4.9: SED's for SMC-SWE-9 and hodge15 with their corresponding residuals plots.

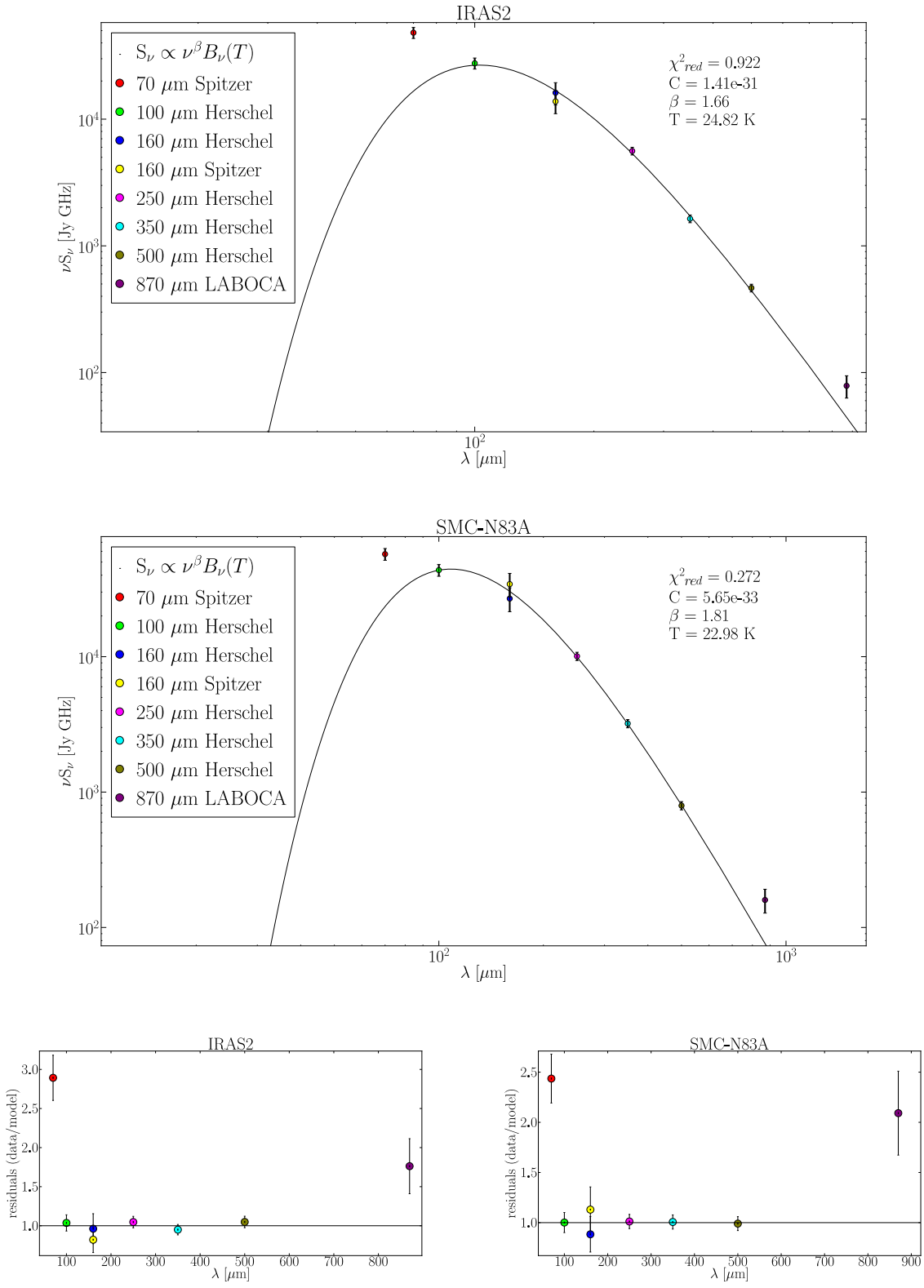

Figure 4.10: SED's for IRAS2 and N83A with their corresponding residuals plots.

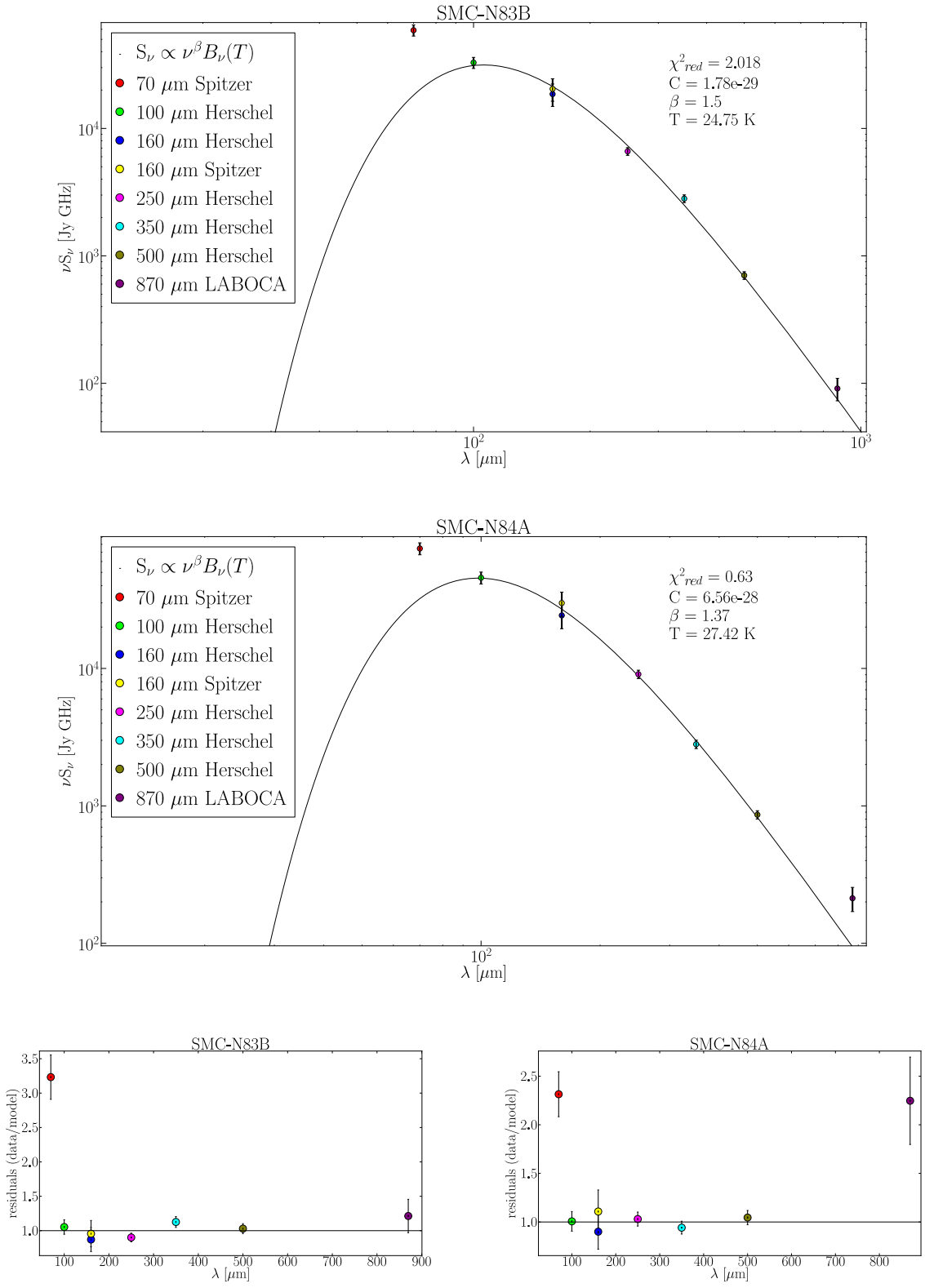

Figure 4.11: SED's for SMC-N83B and SMC-N84A with their corresponding residuals plots.

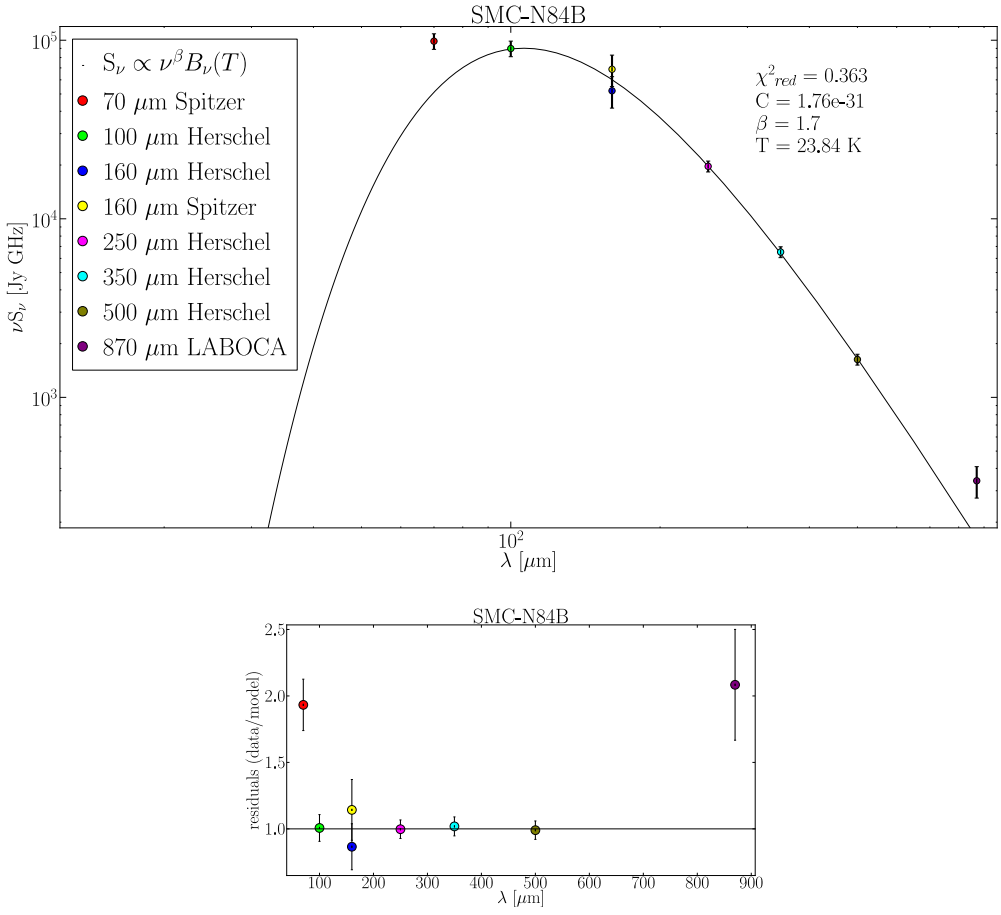

Figure 4.12: SED for SMC-N84B with its corresponding residuals plots.

Bridge

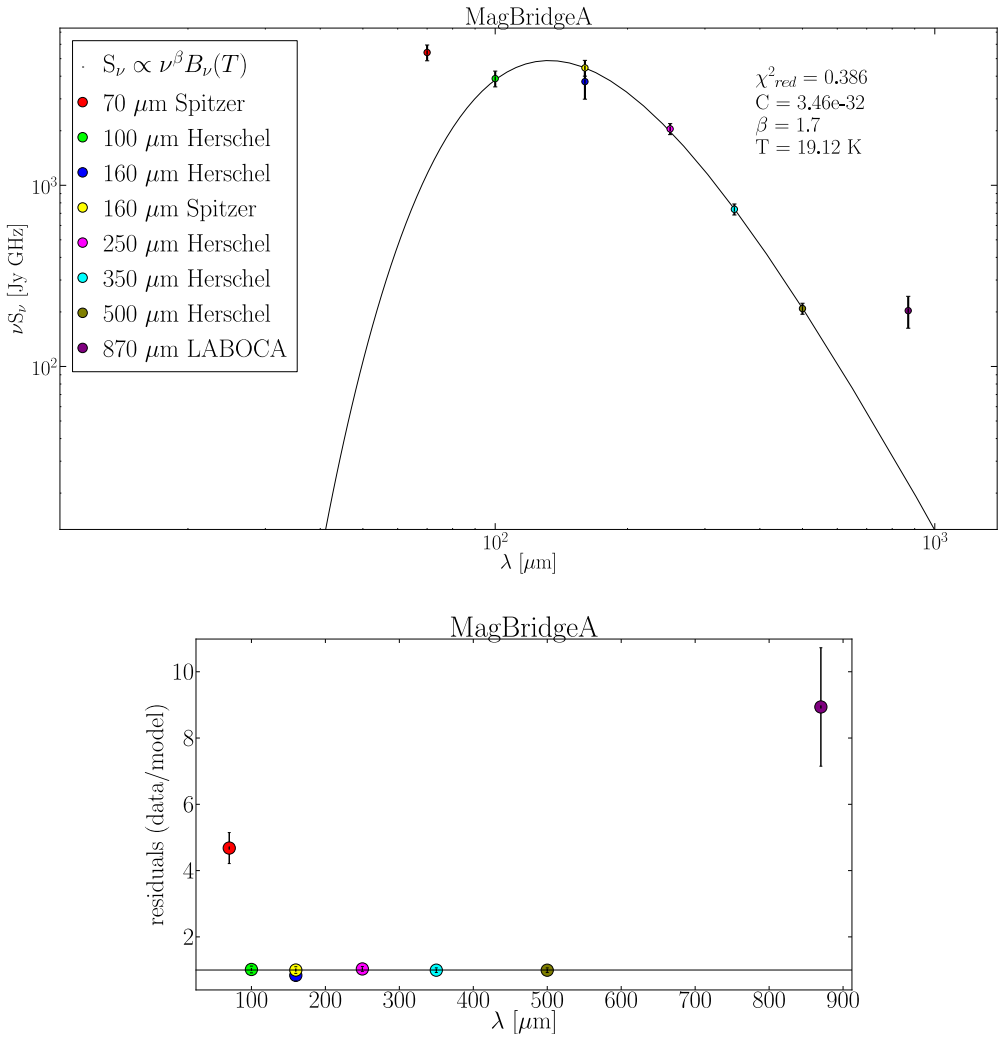

Figure 4.13: SED for MagBridgeA with its corresponding residuals plots.

LMC

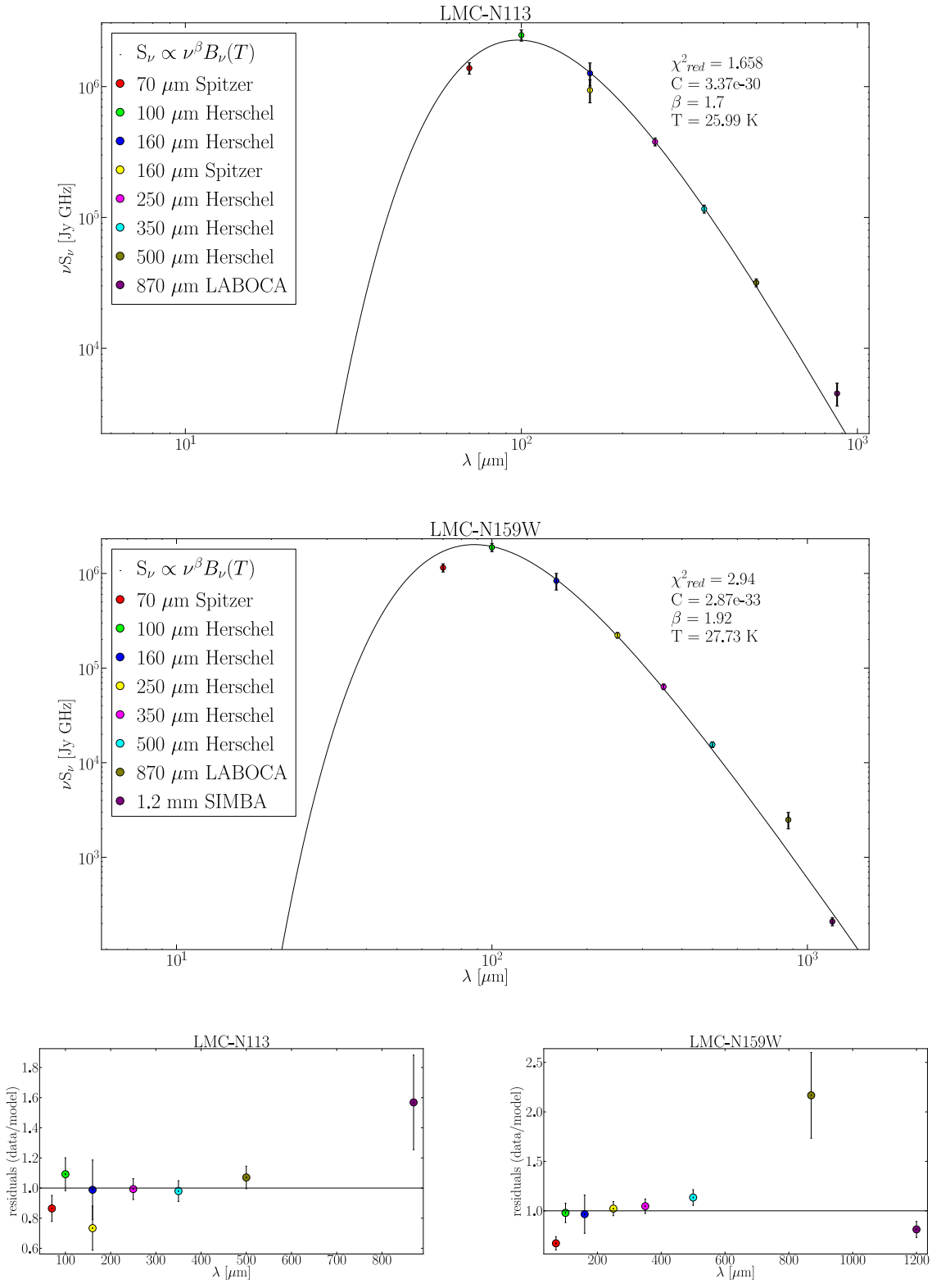

Figure 4.14: SED's for LMC-N113 and LMC-N159W with their corresponding residuals plots.

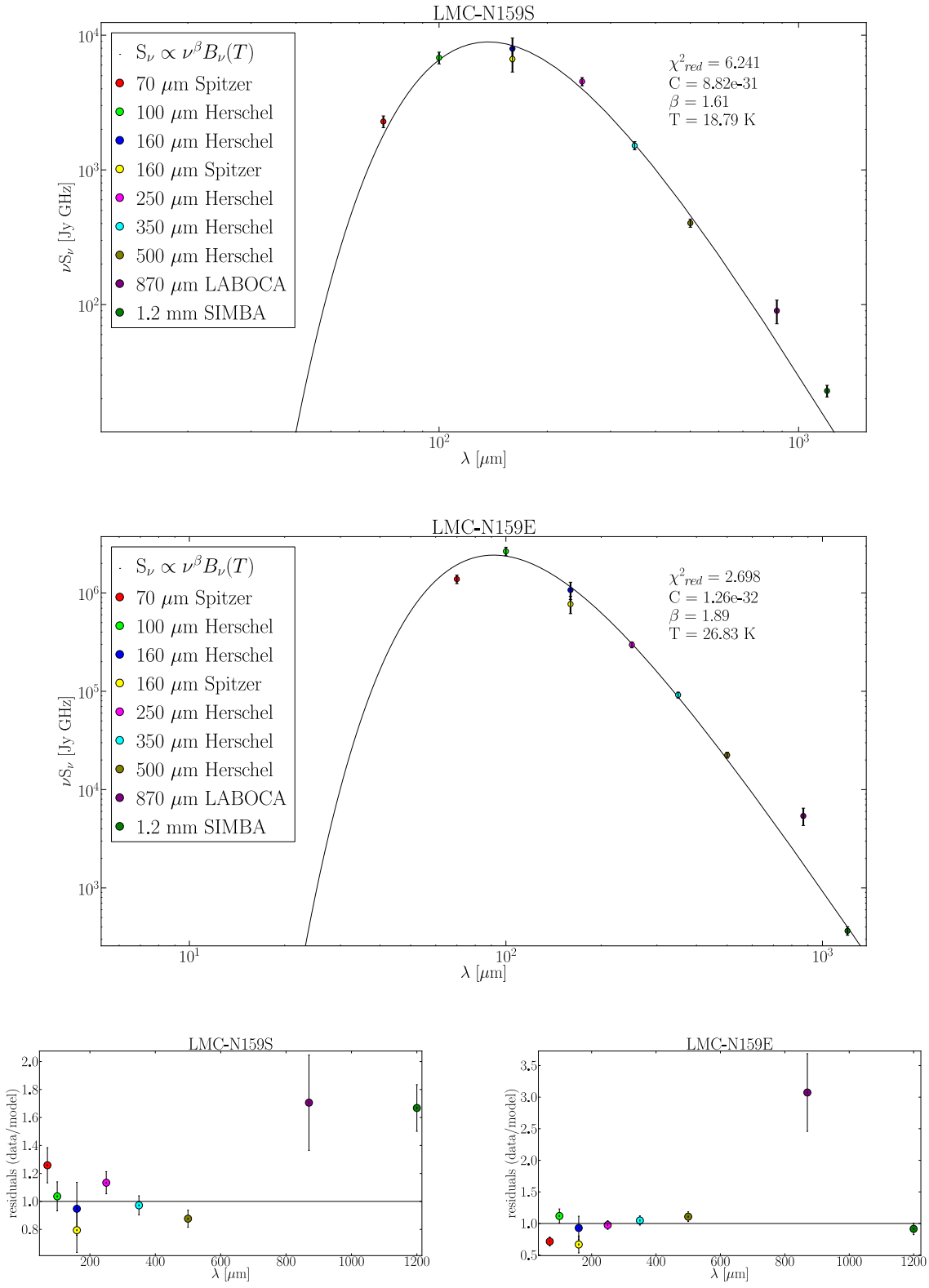

Figure 4.15: SED's for LMC-N159S and LMC-N159E with their corresponding residuals plots.

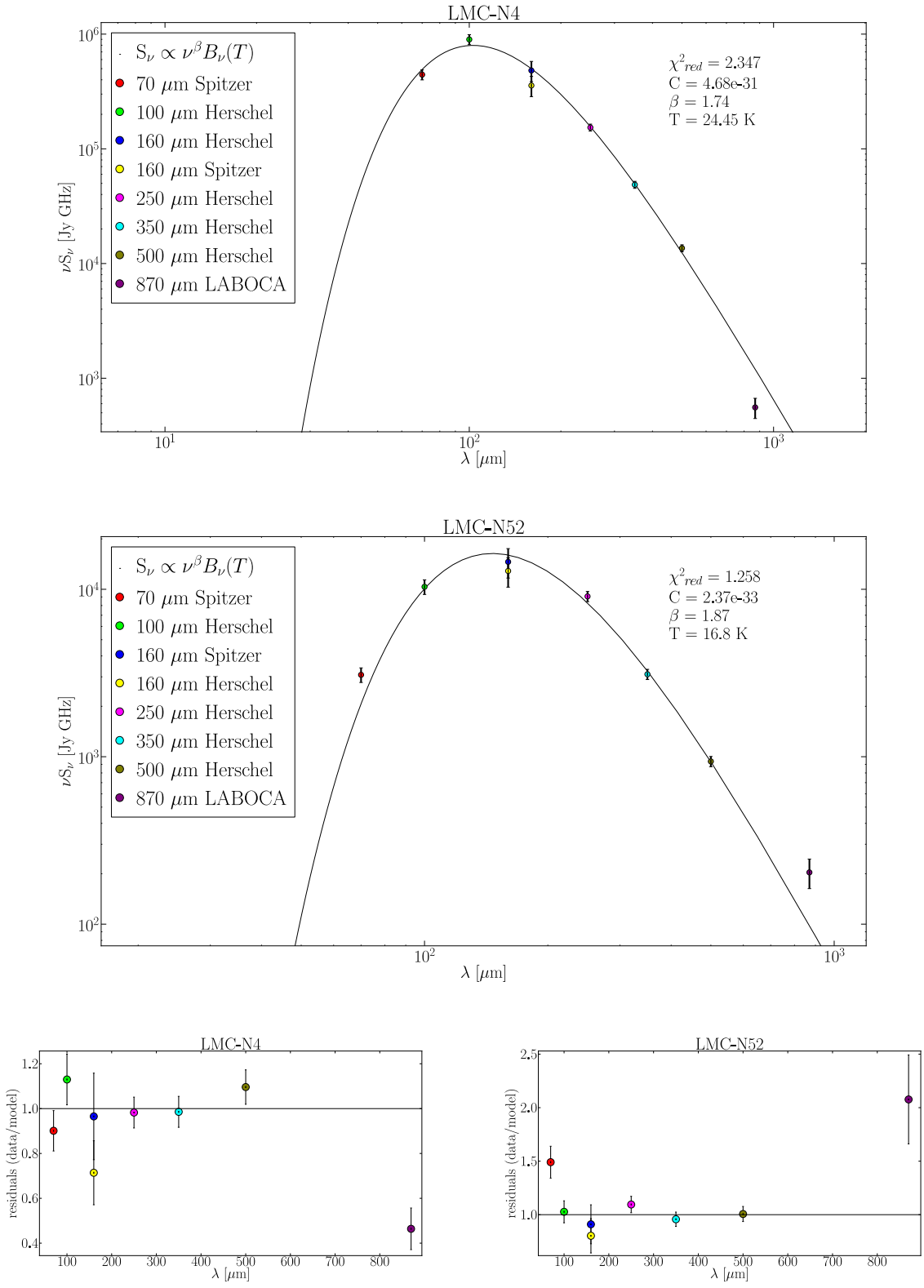

Figure 4.16: SED's for LMC-N4 and LMC-N52 with their corresponding residuals plots.

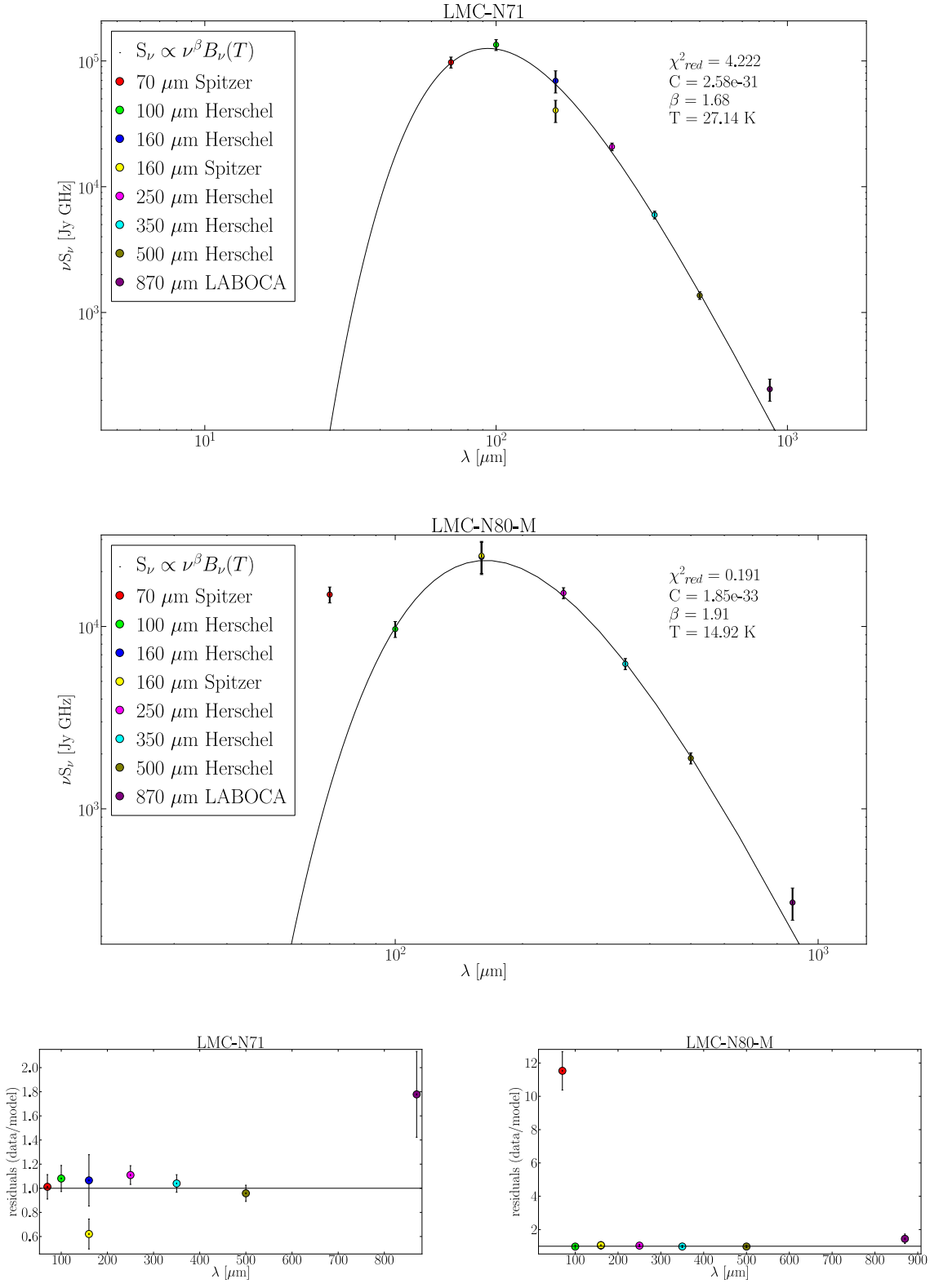

Figure 4.17: SED's for LMC-N71 and LMC-N80-M with their corresponding residuals plots.

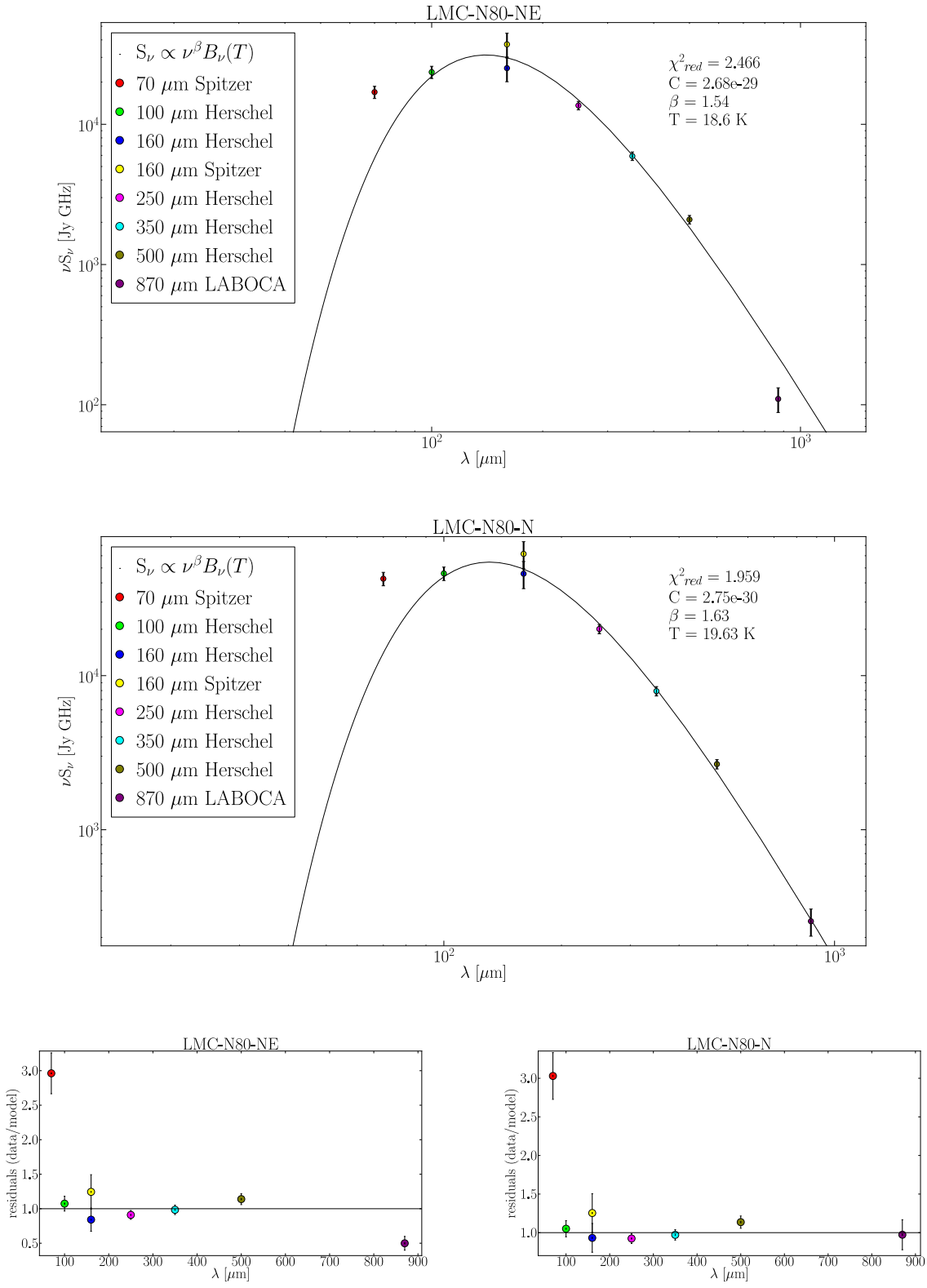

Figure 4.18: SED's for LMC-N80-NE and LMC-N80-N with their corresponding residuals plots.

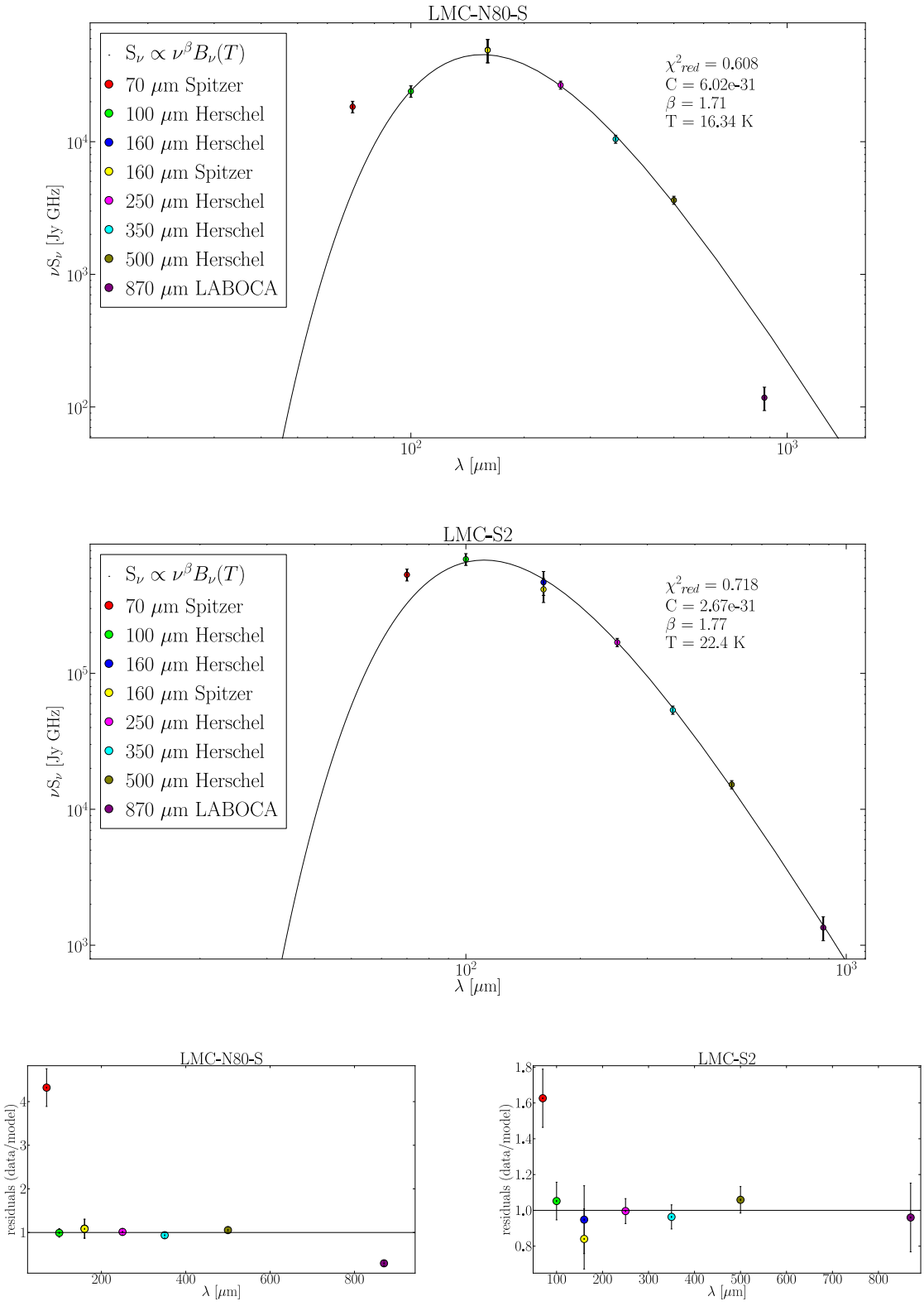

Figure 4.19: SED's for LMC-N80-S and LMC-S2 with their corresponding residuals plots.

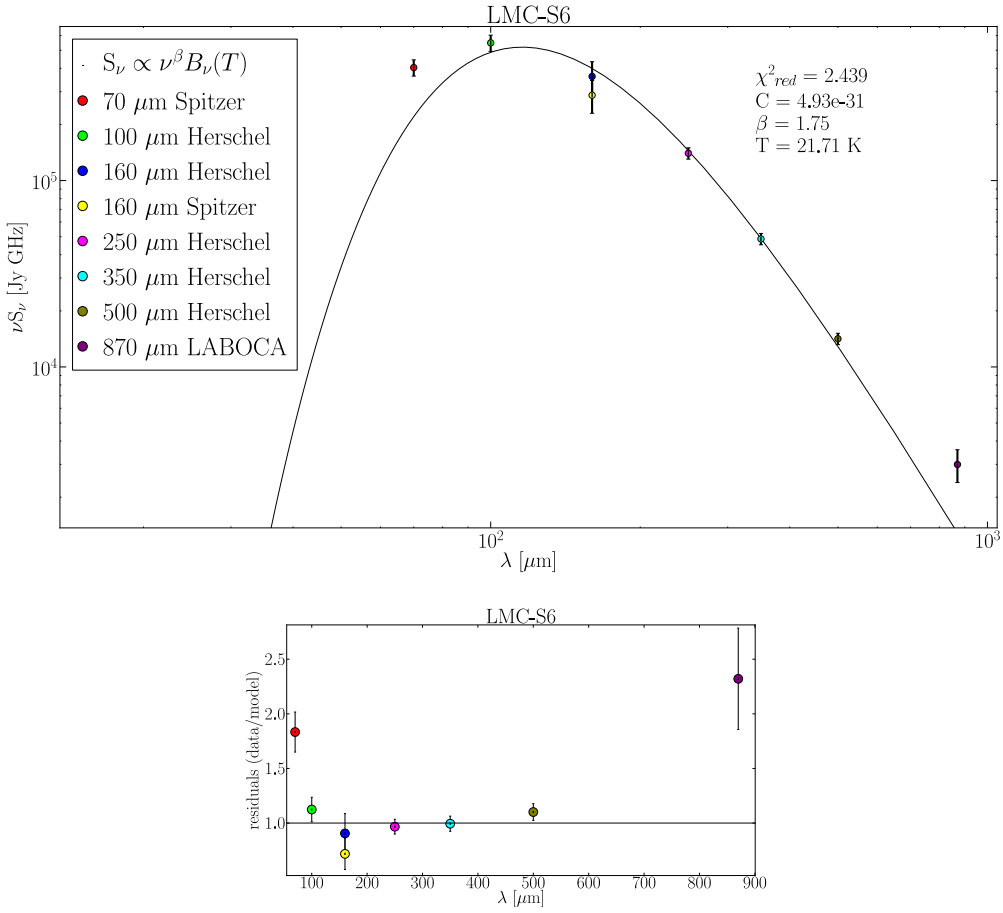

Figure 4.20: SED for LMC-S6 with its corresponding residuals plots.

Table 4.9 presents fitting results, where $\chi^2_{red} = \chi^2/(n-m)$ is the reduced chi-square with n the number of fitted points and m the number of free parameters (in this case 3: C, β and T). To estimate the errors associated to the values of T, β and C obtained from the fit, from the original data set of flux densities we produced synthetic data sets using montecarlo simulations of 5000 iterations (a number reasonably high enough for errors determinations). To create a synthetic data set, to every flux density of the original data set we added a random number normally distributed between -1 and $+1$ multiplied by the error of the corresponding flux density. Since there is a correlation between the parameters fitted (Figure 4.21), to each one of 5000 synthetic data sets we performed the same fitting procedure as for the original data set but leaving just one free parameter at a time. This procedure gave us nearly gaussian distributions with 5000 values for the fitted parameter (Figure 4.22), from which we estimated an error using the standard deviation of the distribution corrected for the deviation of the mean as

$$error = \sqrt{(}\sigma^2 + (m-f)^2) \tag{4.14}$$

where σ is the standard deviation of the distribution, m is the mean value of the distribution and f is the result of the fitting procedure to the original data set.

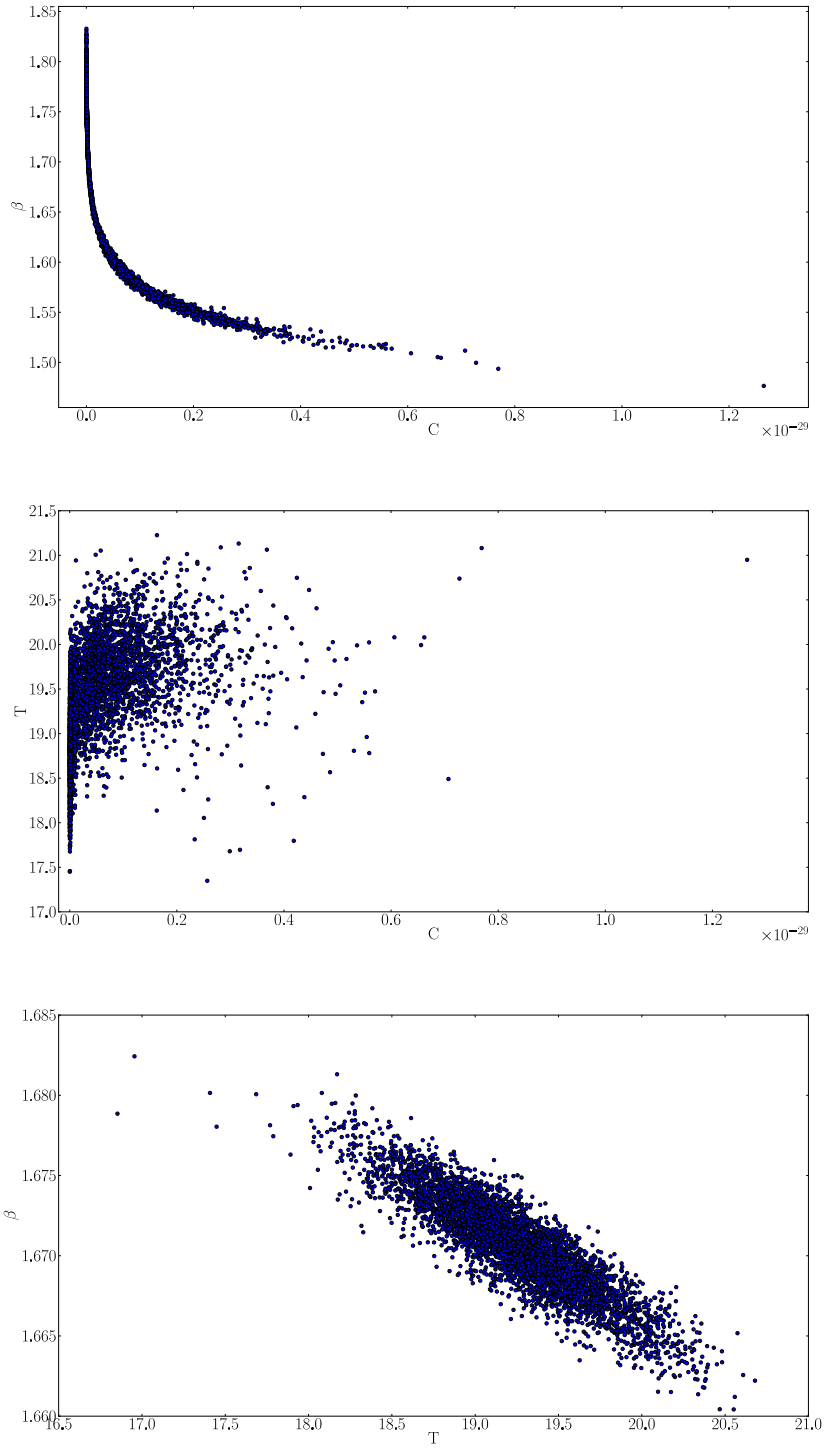

Figure 4.21: Correlations between the parameters obtained from the fit, observed in the montecarlo simulations.

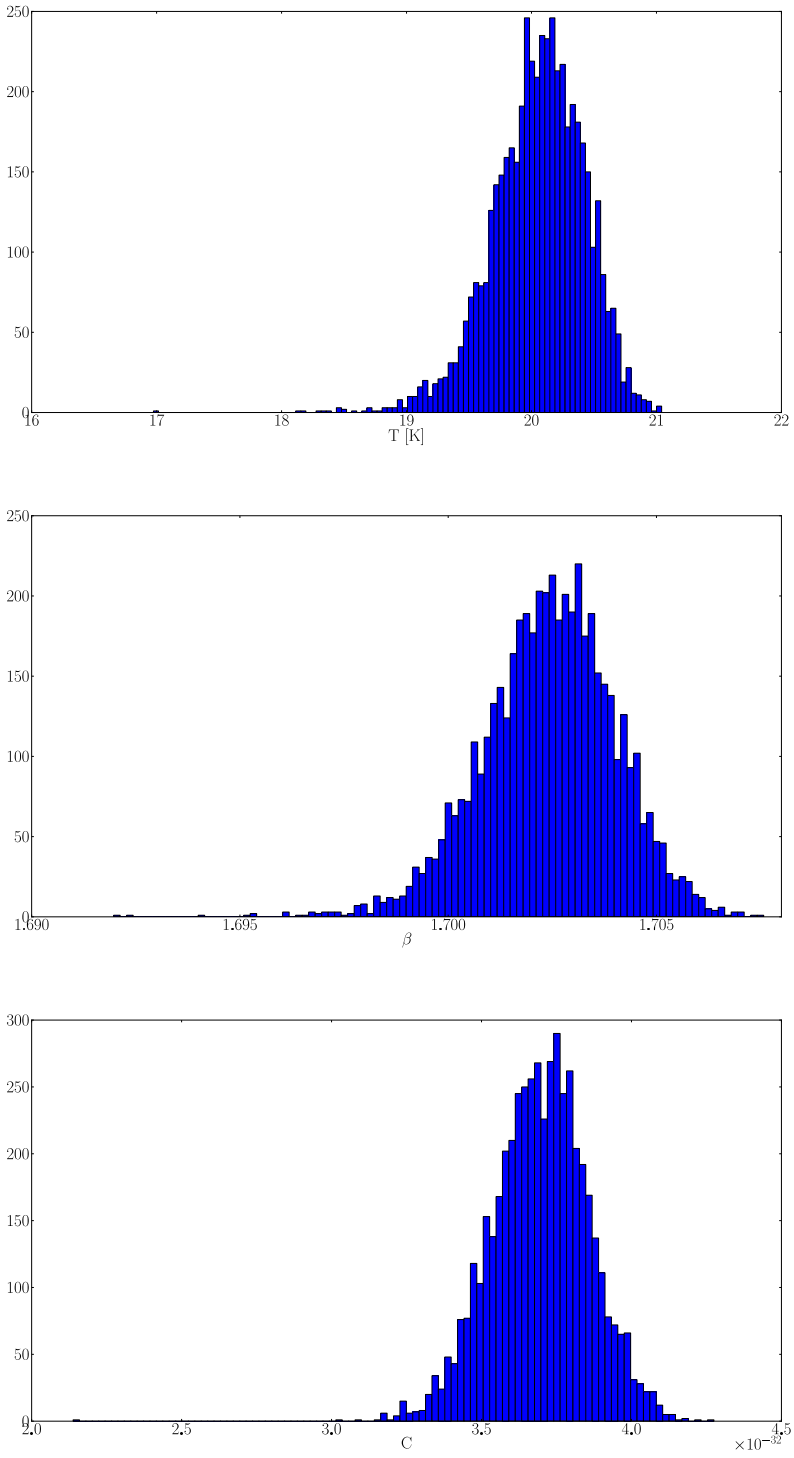

Figure 4.22: Example of histograms with results of montecarlo simulations for fitting results analyzed separately.

4.4.2 Dust opacity

We can determine the opacity of the dust at a given frequency τ_ν from the results of the fitting procedure. Recalling that in an optically thin medium,

$$I_\nu = \tau_\nu B_\nu(T)$$

(a valid assumption in the millimeter and sub-millimeter range). By integrating this relation in the solid angle of the source we obtain the flux density received from the source

$$S_\nu = \tau_\nu B_\nu(T)\Omega \tag{4.15}$$

On the other hand, fitting a blackbody law to the SED yields, from equation (4.12) we see that

$$S_\nu = C \cdot \nu^\beta B_\nu(T_d)$$

and comparing this relation to (4.15) we obtain

$$\tau_\nu \Omega = C\nu^\beta \tag{4.16}$$

So from the values of C and β obtained from the fit and the solid angle of the source we can calculate the dust opacity at a given frequency as

$$\tau_\nu = \frac{C\nu^\beta}{\Omega} \tag{4.17}$$

We calculated the solid angles for every source in the sample as the area of the aperture of photometry, and are presented in Table 4.8

Finally, dust opacities at 160 μm are calculated using equation (4.17) and presented in column 5 of Table 4.9 by using the solid angles of Table 4.8 and the values of C and β obtained from the fit and presented in columns 3 and 4 of Table 4.9.

To obtain the dust opacity at 870 μm we cannot use the relation (4.17) since the model of equation (4.12) does not fit this value (excess of emission explained in Chapter 5). As we are assuming that there is a single dust component, we use the dust temperature obtained from the fit and the flux density measured at 870 μm in equation (4.15) to obtain the dust opacity at 870 μm, i.e:

$$\tau_\nu = \frac{S_\nu}{\Omega B_\nu(T_d)} \tag{4.18}$$

By using the dust temperatures obtained from the fit and presented in column 2 of Table 4.9 and the solid angles presented in Table 4.8 we calculated the dust opaticities at 870 μm, which are presented in column 6 of Table 4.9.

Table 4.8. Solid angles

Source	Ω $[10^{-7} sr]$	Source	Ω $[10^{-}7 sr]$
IRAS2	1.30	LMC-N71	2.66
hodge15	2.66	LMC-N80-M	17.97
SMC-SW-1	0.96	LMC-N80-NE	4.49
SMC-SW-2	0.96	LMC-N80-N	4.49
SMC-SW-3	2.66	LMC-N80-S	17.97
SMC-SW-4	1.70	LMC-N4	32.56
SMC-SW-5	1.30	LMC-S2	80.41
SMC-SW-6	1.30	LMC-S6	20.84
SMC-SW-7	1.70	MagBridgeA	5.98
SMC-SW-8	2.15	LMC-N52	5.98
SMC-SW-9	2.66	N83A	0.66
LMC-N159S	3.83	N83B	0.43
LMC-N159W	2.66	N84A	1.30
LMC-N159E	5.98	N84B	2.66
LMC-N113	32.56		

Table 4.9. Fitting results

Source	T_{dust}[K]	β	$C[srHz^{-\beta}]$	$\tau_{160\mu m}[10^{-4}]$	$\tau_{870\mu m}[10^{-5}]$	χ^2_{red}
IRAS2	24.8±0.4	1.66	1.41e-31±5.97e-33	2.56 ±0.15	2.78 ±0.61	0.92
hodge15	20.0±0.3	1.56	4.59e-30±2.75e-31	2.41 ±0.18	2.40 ±0.48	2.77
SMC-SW-1	25.4±1.0	1.54	1.32e-30±1.73e-31	1.09 ±0.15	1.11 ±0.95	4.07
SMC-SW-2	25.9±1.0	1.57	9.72e-31±1.09e-31	1.87 ±0.22	1.54 ±0.32	2.17
SMC-SW-3	23.5±0.4	1.67	2.16e-31±1.05e-32	2.54 ±0.17	2.35 ±0.45	1.78
SMC-SW-4	24.5±0.5	1.94	3.49e-35±2.40e-36	1.32 ±0.11	1.22 ±0.28	1.76
SMC-SW-5	19.5±0.2	1.77	6.16e-33±4.69e-34	2.50 ±0.22	3.23 ±0.68	0.50
SMC-SW-6	22.5±0.7	1.50	1.57e-29±1.61e-30	3.10 ±0.35	3.32 ±0.71	3.53
SMC-SW-7	25.3±1.3	1.76	1.02e-32±1.49e-33	2.39 ±0.37	2.33 ±0.48	2.64
SMC-SW-8	23.3±0.3	1.28	3.51e-27±20.2e-28	0.84 ±0.48	2.30 ±0.48	1.59
SMC-SW-9	20.4±0.5	1.93	1.99e-34±1.66e-35	3.63 ±0.35	2.10 ±0.40	0.82
LMC-N159S	18.8±0.4	1.61	8.82e-31±7.09e-32	1.32 ±0.12	1.34 ±0.25	6.24
LMC-N159W	27.7±1.0	1.92	2.87e-33±3.13e-34	39.55±4.59	39.43±8.11	2.94
LMC-N159E	26.8±1.4	1.89	1.26e-32±1.71e-33	33.09±4.73	38.27±8.09	2.70
LMC-N113	26.0±1.2	1.70	3.37e-30±1.50e-31	7.56 ±0.50	6.02 ±1.28	1.66
LMC-N71	27.1±1.4	1.68	2.58e-31±3.41e-32	4.03 ±0.57	3.97 ±1.08	4.22
LMC-N80-M	14.9±0.1	1.91	1.85e-33±7.87e-35	2.84 ±0.17	1.66 ±0.34	0.19
LMC-N80-NE	18.6±0.2	1.54	2.68e-29±1.61e-30	4.74 ±0.35	1.69 ±0.32	2.47
LMC-N80-N	19.6±0.2	1.63	2.75e-30±2.03e-31	6.19 ±0.53	3.61 ±0.73	1.96
LMC-N80-S	16.3±0.2	1.71	6.02e-31±3.21e-32	3.24 ±0.22	0.55 ±0.15	0.61
LMC-N4	24.5±0.4	1.74	4.68e-31±2.19e-32	3.25 ±0.22	0.79 ±0.15	2.34
LMC-S2	22.4±0.3	1.77	2.67e-31±1.48e-32	1.75 ±0.12	0.95 ±0.19	0.72
LMC-S6	21.7±0.3	1.75	4.93e-31±4.87e-32	7.10 ±0.77	8.29 ±1.67	2.44
MagBridgeA	19.1±1.0	1.70	3.46e-32±2.55e-33	0.42 ±0.05	2.24 ±0.49	0.39
LMC-N52	16.8±0.2	1.87	2.37e-33±3.25e-34	3.54 ±0.51	2.32 ±0.47	1.26
N83A	23.0±0.3	1.81	5.65e-33±7.09e-34	14.01±1.85	12.17±2.39	0.27
N83B	24.8±0.4	1.50	1.78e-29±1.33e-30	10.63±0.91	9.52 ±1.84	2.02
N84A	27.4±1.2	1.37	6.56e-28±8.18e-29	3.28 ±0.43	6.54 ±1.33	0.63
N84B	23.8±0.3	1.70	1.76e-31±1.56e-32	4.83 ±0.48	6.17 ±1.25	0.36

Chapter 5

Analysis

5.1 Sub-millimeter excess

From the SED's and residual plots of section 4.4 we can see that the flux densities measured at 870 μm and also at 70 μm are higher than expected from the modified blackbody law that fits all the other points, a result previously reported in molecular clouds in the Magellanic system and entire galaxies with low metallicity, including the Magellanic Clouds (Sauvage et al. 1990, Aguirre et al. 2003, Galametz et al. 2011, Israel et al. 2010). The ratio between observations and model is what we call the excess of emission at 870 and 70 μm. These excesses are tabulated in Table 5.1

In order to determine if these excesses are related to any physical property, we plotted them as a funcion of the C, β, T_d and τ obtained from the fit and presented in Table 4.9. Figures 5.1 and 5.2 present these plots, where we have separated the points corresponding to the SMC from those of the LMC and Magellanic Bridge.

At a first look to Figures 5.1 and 5.2, it seems that only the excess at $70\mu m$ in the LMC has a dependence on temperature. Apparently there is no other evident dependance in the other plots. In order to verify this premise, we plotted these same results replacing the values of the X and Y axes with the ordinal number of the excesses, temperatures, $\beta' s$ and opacities and calculated the Spearman's rank correlation coefficient as

$$\rho = 1 - \frac{6 \sum d_i^2}{n(n^2 - 1)} \tag{5.1}$$

With this we are making a non-parametric measure of statistical dependence between the two variables in each plot. It assesses how well the relationship between two variables can be described using a monotonic function. If there are no repeated data values, a perfect Spearman correlation of $+1$ or -1 occurs when one of the variables is a perfect monotonic function of the other, positive or negative respectively. The results are presented in Figures 5.3 and 5.4 with the corresponding spearman's ρ, that was calculated using (5.1) and taking care of including a tie correction for repeated values.

From Figures 5.3 and 5.4 we can see that indeed there is a negative correlation between the

Table 5.1. Sub-millimeter excesses in the fits measured as data/model

Source	E($870\mu m$)	E($70\mu m$)
LMC-N113	1.57±0.31	0.86±0.09
LMC-N80-NE	0.50±0.10	2.96±0.30
LMC-N80-M	1.44±0.29	11.53±1.15
LMC-N80-N	0.97±0.19	3.03±0.30
LMC-N80-S	0.29±0.06	4.32±0.43
LMC-N159E	3.07±0.61	0.72±0.07
LMC-N159W	2.17±0.43	0.67±0.07
LMC-N159S	1.71±0.34	1.26±0.13
LMC-N4	0.46±0.09	0.90±0.09
LMC-N52	2.08±0.42	1.49±0.15
LMC-N71	1.78±0.356	1.01±0.10
LMC-S2	0.96±0.19	1.63±0.16
LMC-S6	2.32±0.46	1.83±0.18
SMC-N83A	2.09±0.42	2.44±0.24
SMC-N83B	1.21±0.24	3.23±0.32
SMC-N84A	2.25±0.45	2.31±0.23
SMC-N84B	2.08±0.42	1.93±0.19
SMC-SWE-1	1.29±0.26	2.80±0.28
SMC-SWE-2	1.29±0.26	2.48±0.25
SMC-SWE-3	1.56±0.31	2.25±0.22
SMC-SWE-4	2.34±0.47	2.34±0.23
SMC-SWE-5	2.44±0.49	3.10±0.31
SMC-SWE-6	1.45±0.29	2.14±0.21
SMC-SWE-7	2.15±0.43	2.36±0.24
SMC-SWE-8	2.51±0.50	3.32±0.33
SMC-SWE-9	1.58±0.32	2.94±0.29
IRAS2	1.76±0.35	2.89±0.29
hodge15	1.40±0.28	3.57±0.36
MagBridgeA	8.94±1.79	4.68±0.47

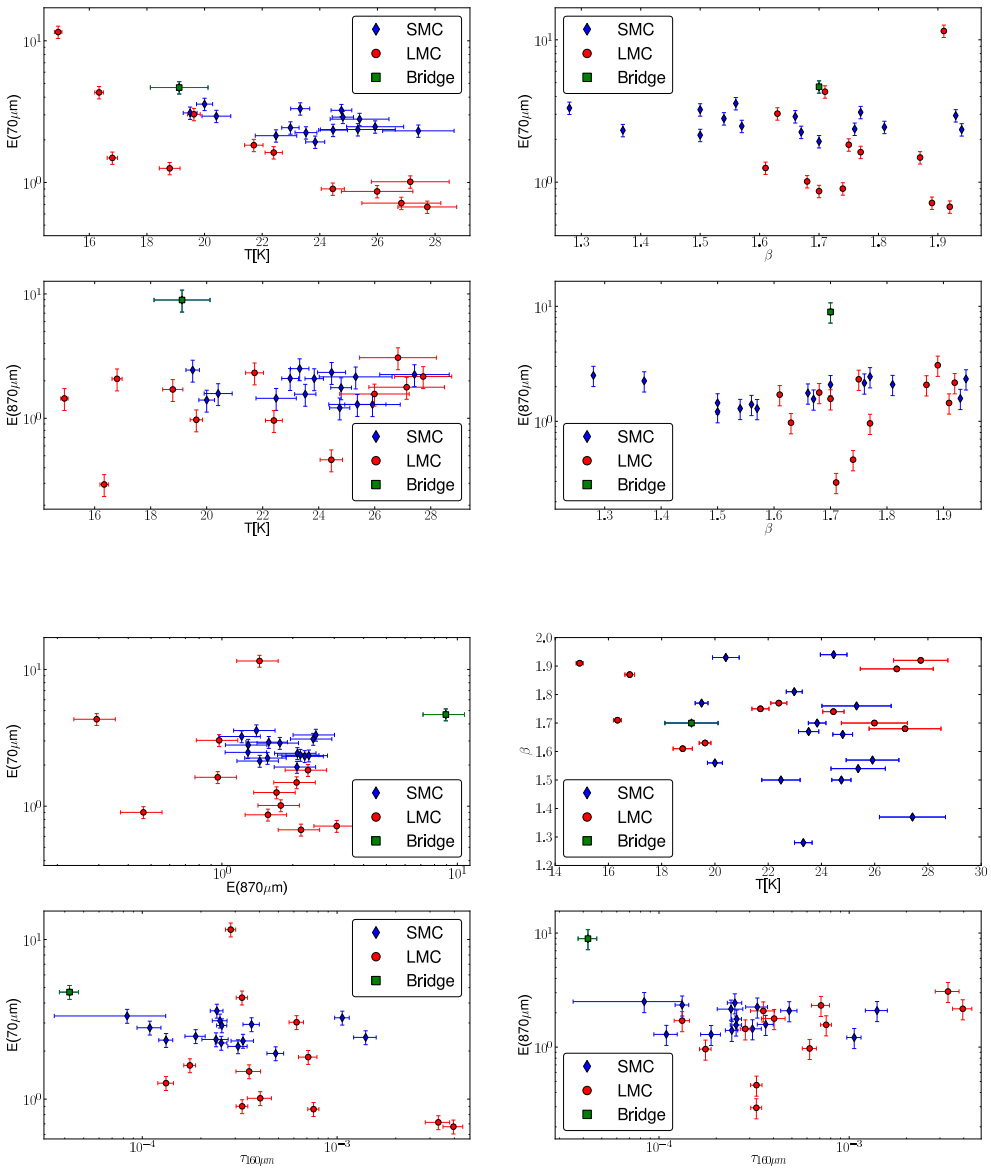

Figure 5.1: Sub-millimeter excesses as a function of T_d, β and τ. Only for E(70μm) there is an apparent dependence with dust temperature. Other plots do not show a relation strong enough.

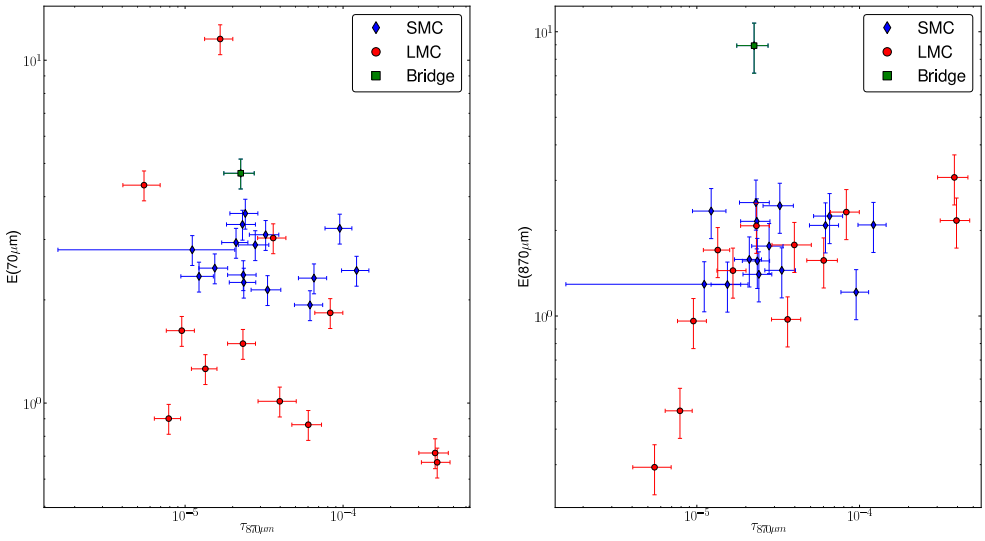

Figure 5.2: Sub-millimeter excesses as a function of T_d, β and τ

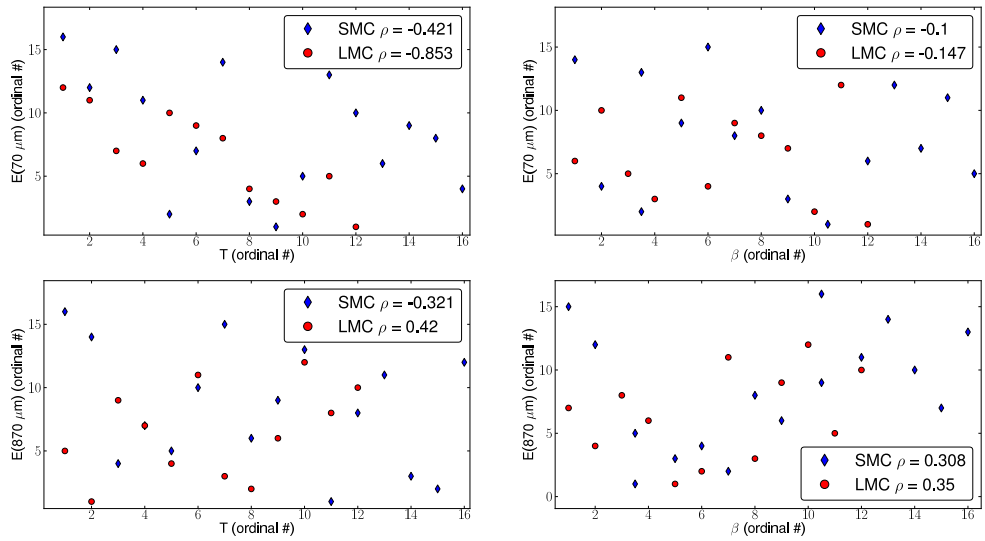

Figure 5.3: Rank correlation plots. Values of variables in axes have been replaced by the ordinal number. ρ is the spearman's rho calculated from equation (5.1)

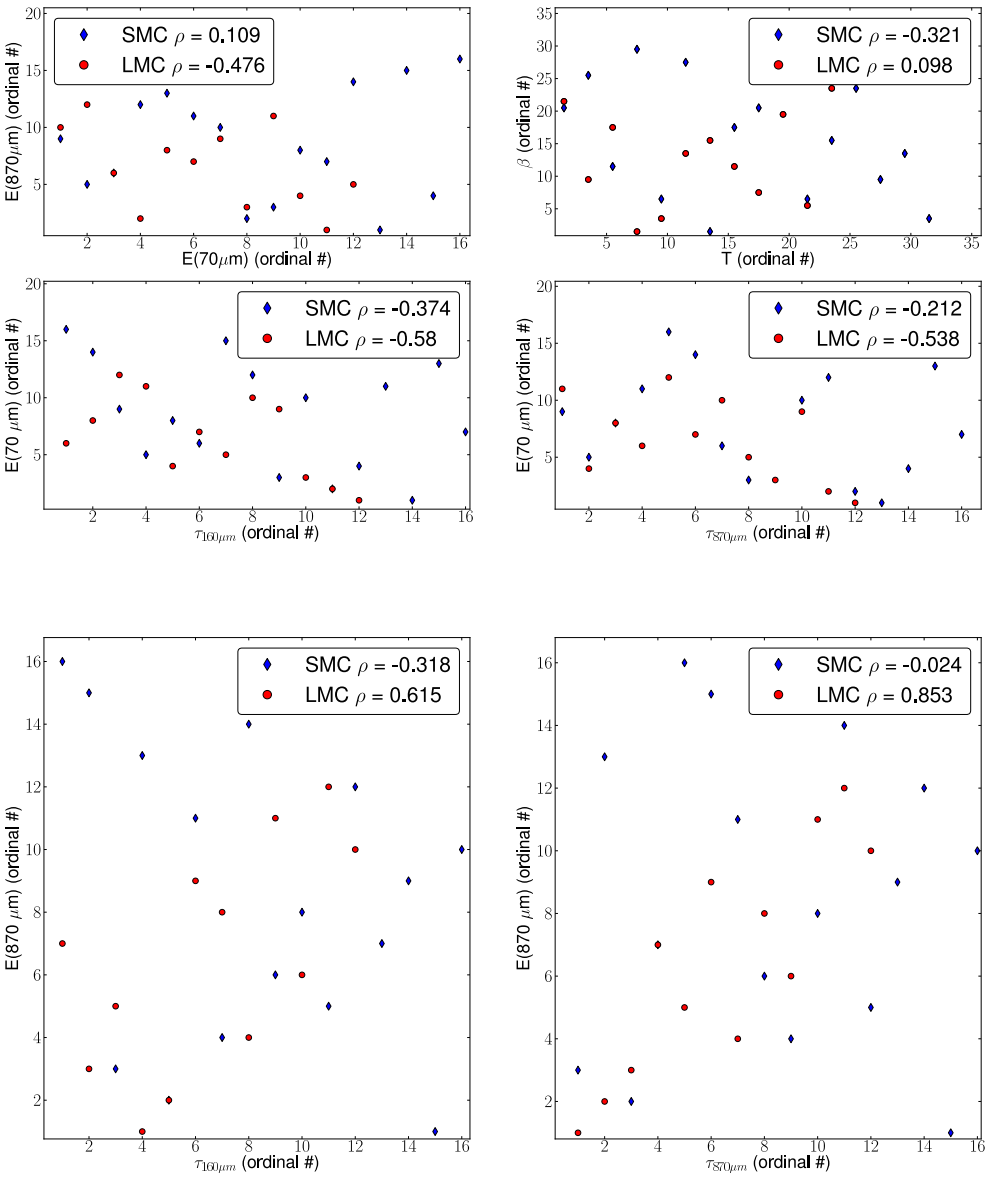

Figure 5.4: Rank correlation plots. Values of variables in axes have been replaced by the ordinal number. ρ is the spearman's rho calculated from equation (5.1)

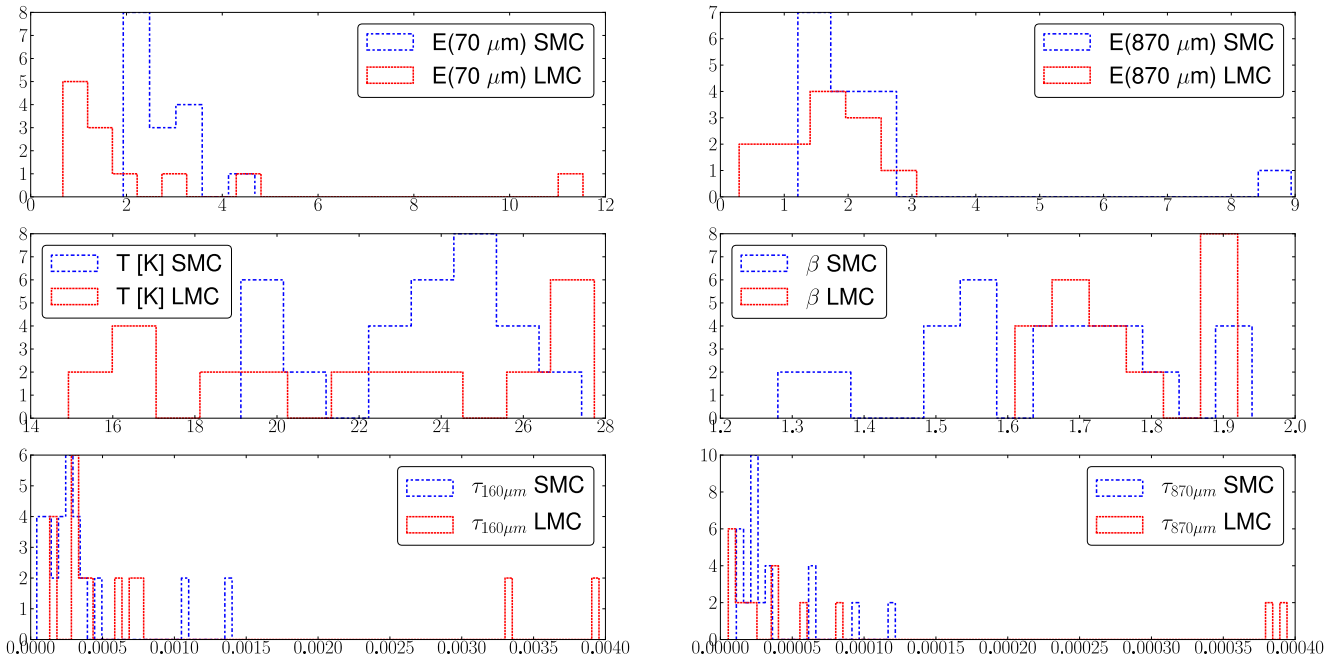

Figure 5.5: Histograms for excesses, dust temperatures, $\beta's$ and opacities. Only for E($70\mu m$) there is a clear difference between SMC and LMC.

excesses at $70\mu m$ and the dust temperature for the LMC with a ρ of -0.85. All the other plots do not have a ρ close enough to $+1$ or -1 to assure a monotonic correlation.

In order to see the shape of the distribution of each one the properties observed, we plotted histograms for the excesses, temperatures, $\beta's$ and opacities. Figure 5.5 presents these results.

A first conclusion from these histograms is that the average value of excess at 70 μm is higher for the SMC than for the LMC, and that the distributions seem different. For the other histograms, we cannot conclude that the distributions of each of the properties calculated come from the same parent distribution or not. To answer this question we performed a Kolmogorov-Smirnov (K-S) test to each parameter (T_d, β, E($70\mu m$), E($870\mu m$), $\tau_{160\mu m}$ and $\tau_{870\mu m}$) between the values for the SMC and LMC. Figure 5.6 presents the cumulative distributions for each parameter and the results of the Kolmogorov-Smirnov test.

Assuming a true null hypothesis that the two distributions, in the SMC and LMC, of the same property come from the same parent distribution, from each Kolmogorov-Smirnov test we obtained a D value equal to the maximum distance between the two cumulative distributions of the same property in the SMC and LMC, and a p-value corresponding to the probability of obtaining a statistic test at least as extreme as the one that is actually observed, assuming that the null hypothesis is true. In other words, it is the probability of obtaining a $D > D_{obs}$ under the assumption of a true null hypothesis. With this we are testing the value of D_{obs} to determine if it is good enough to reject the null hypothesis that the two distributions come from the same parent distribution. The results of the Kolmogorov-Smirnov test are summarized in Table 5.2

The p-values obtained for each test of T_d, β, E($70\mu m$), E($870\mu m$), $\tau_{160\mu m}$ and $\tau_{870\mu m}$ are presented in Table 5.2 along with the viability of rejecting the null hypothesis at a significance level of 5%. This means that a p-value lower than 0.05 is a very low probability of obtaining

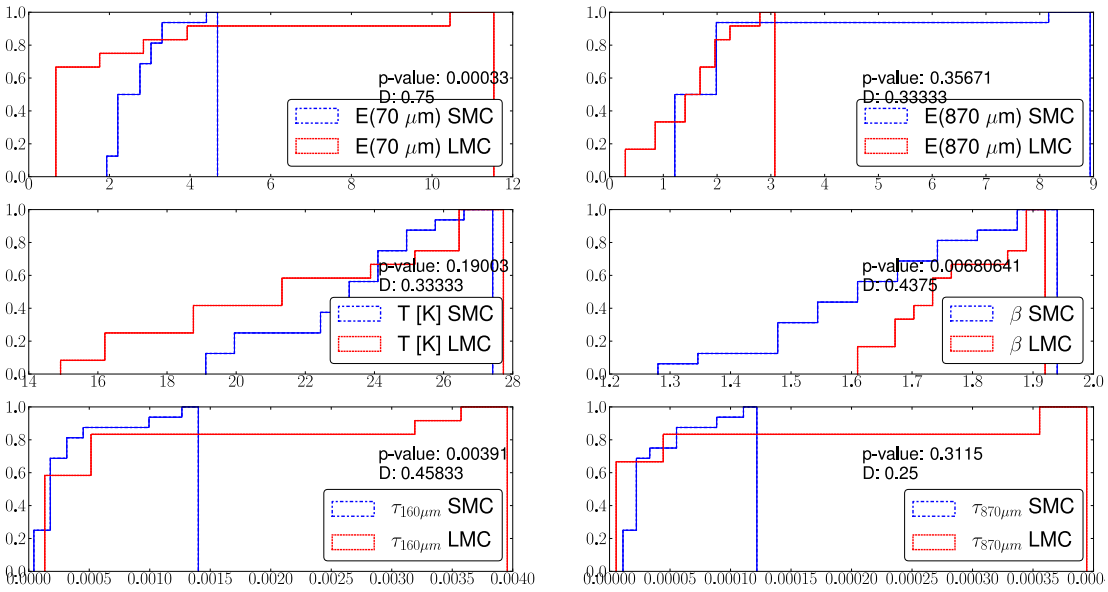

Figure 5.6: Cumulative distributions for excesses, dust temperatures, $\beta's$ and opacities and K-S test results between SMC and LMC

Table 5.2. K-S test results

	E(70μm)	E(870μm)	T_d	β	$\tau_{160\mu m}$	$\tau_{870\mu m}$
p-value	0.00033	0.35671	0.19003	0.00681	0.00391	0.3115
rejection 5%	yes	no	no	yes	yes	no
rejection 1%	yes	no	no	yes	yes	no

a $D > D_{obs}$ assuming a true null hypothesis, in other words, there is a very low probability of obtaining a result more extreme than the observed under the null hypothesis. So if p-value is lower than 0.05 we can reject the null hypothesis at a level of significance of 5%. Using this criteria we can reject the null hypothesis for the excesses at 70 μm, $\beta' s$ and opacities at 160μm. In order to check the validity of this premise, we can repeat this same analysis to a lower (and more strict) significance level of 1%, and using the same reasoning as for the 5% significance level, we reject the null hypothesis at a level of 1% if p-value is lower than 0.01. Using this criteria, once again we reject the null hyphotesis for the excesses at 70 μm, $\beta' s$ and opacities at 160μm. So differences between SMC and LMC in the distributions of these parameters could be due to different properties that characterize these two galaxies, like metallicity for example. From the first panel of Figure 5.5 and the result of the K-S test for the excess of emission at 70 μm, we can see that in the SMC excess is higher, meaning more dust or higer levels of emissivity at this wavelenght. The difference between the distibutions of $\beta' s$ is also important since it shows a difference in the dust properties, like chemical composition or grain size distribution. Larger dust grains can increase the dust emission and could explain the higher excess of emission at 70 μm in the SMC. The difference between the dust opacities at 160μm in SMC and LMC illustrates a difference in the peak emission of these two populations.

In the following sections of this Chapter we will work with different parameters that can be obtained from sub-millimeter dust emission: gas mass, dust-to-gas ratio and dust emissivity. In each subsection we will assume as known one or two of these parameters and will infered the remaining parameters and analyse the consequences of these assumptions. Since these parameters are result of the same dust emission studied, they should reflect a relationship. The motivation of this analysis is to verify this idea.

5.2 Dust and gas correlation

In this section we will assume that the gas mass is known through the virial mass as calculated in equation (5.2) below (i.e the viral mas traces the total amount of gas), and from this we will calculate the dust emissivity. Also assuming a dust-to-gas ratio we will explain and determine dust absorption coeficients.

Recalling the expression for the intensity $I_\nu = \tau_\nu B_\nu(T)$, in an optically thin medium the dust emission depends linearly on the opacity term, so we can study the dust emission from the dust opacity, and correlate it with the gas emission, which depends on the amount of gas (column density). The correlation between the dust and gas emission, or dust emissivity as in Boulanger et al. (1996) is defined as the quotient between the dust opacity and the column density of HI: τ/N_H, and it is a direct relation between the ratio of dust and gas masses and the emissivity of the atomic gas. It is actually an optical depth per gas nucleon which is an emissivity per gas column.

By analysing this parameter we can estimate how the dust is emiting in relation to the gas present in these low metallicity systems and make a comparision with our Galaxy. Dust opacities were obtained using equations (4.17) and (4.18) and presented in Table 4.9. H_2 column densities were obtained from virial masses through CO data taken from the literature for those sources whose CO observations where available. If we assume that a molecular cloud is in virial equilibrium and that the virial mas traces the total amount of gas, we can calculate its total gas mass from

the CO line emission. This is known as the virial mass (MacLaren et al. 1988)

$$M_{vir} = C\Delta V^2 R \tag{5.2}$$

where C is a constant value that depends on the density profile chosen, ΔV is the FWHM of the CO line that measures the velocity dispersion of the gas and R is the physical radius of the amount of CO in the cloud. This radius is measured from the CO maps available in the literature. For those sources with no CO maps in the literature, a CO radius was assumed equal to the beamsize of the corresponding telescope. The virial mass is a gravitational mass, so if the virial approximation is correct, the virial mass traces the total mass in the cloud. Now, at the typical conditions of density and temperature of molecular clouds, the gas tends to be mainly molecular, so the (total) mass traced by the virial approximation is a molecular gas mass. Assuming a constant density profile, the value of C in equation (5.2) is 210, and the resulting masses are presented in Table 5.3

From the mass of H_2 traced by the virial mass we can calculate the column density of H_2 assuming a spherical symmetry

$$N_{H_2} = \frac{M_{vir}}{\mu m_{H_2} \pi R^2} \tag{5.3}$$

where m_{H_2} is the mass of the H_2 molecule[1], R is the radius of the aperture photometry and μ is the molecular weight taking He in account[2]. Finally, as a H_2 molecule is composed of two H atoms, the column density of the atomic gas N_H will be $2N_{H_2}$. We selected the sources in the sample with available CO data in the literature and calculated their virial masses and H column density. Table 5.3 presents these results.

We plotted the obtained τ/N_H as a function of temperature and hydrogen column density and present them in Figure 5.7, where clouds for the SMC have been separated from those of LMC and Magellanic Bridge. In Figure 5.7, at $870\mu m$ we cannot see any apparent trend with the dust temperature. LMC-N52 and LMC-N159S fall far away from the other LMC sources, which draws our attention since these two sources are interesting for being molecular clouds with no evidence of active star formation. Concerning hydrogen column density, τ/N_H seems to have a negative trend with increasing N_H, which is a rather curious result since if the dust and gas are correlated, τ/N_H is a value related with the amount of dust emission per gas column, so larger gas columns should allow more dust emission, implying a nearly flat dependency with N_H. It is quite interesting that LMC-N159S and MagBridgeA escape from this expected flatness. Perhaps this negative trend is real, but more data is needed to verify this hyphotesis. Also, there is no apparent difference between the values of SMC and LMC. At 160 μm, there could be a negative trend for τ/N_H with T if it were not for N52 and N159S (the two interesting sources for their lack of star formation activity), and it seems that the sources for the SMC have lower τ/N_H then the LMC sources, but once again we need more data to verify this tendency. As for the dependency with N_H at 160 μm, once again we recover the peculiar negative relation with τ/N_H, which draws our attention.

An interesting result is that at 870 μm the source in the Magellanic Bridge has the highest values of τ/N_H, meaning a high dust emission per amount of gas. This result can be explained with the high excess of emission observed at 870 μm for this source, despite its low dust content expected from its low metallicity.

[1] $3.348 \times 10^{-24} g$
[2] 1.36

Table 5.3. Virial masses and column densities

Source	$M_{vir}[10^5 M_\odot]$	$N_H[10^{21} cm^{-2}]$	$\frac{\tau_{160\mu m}}{N_H}[10^{-25} cm^2]$	$\frac{\tau_{870\mu m}}{N_H}[10^{-27} cm^2]$
LMC-N4	0.77^a	0.88	3.71 ± 0.25	9.01 ± 1.71
LMC-N159W	2.97 ± 0.59^b	41.30 ± 8.26	0.96 ± 0.22	9.55 ± 2.74
LMC-N159E	2.44 ± 0.49^b	15.07 ± 3.01	2.20 ± 0.54	25.39 ± 7.39
LMC-N159S	3.21 ± 0.64^b	30.93 ± 6.19	0.04 ± 0.01	0.43 ± 0.12
LMC-N113	0.96 ± 0.10^c	1.09 ± 0.11	6.93 ± 0.83	55.19 ± 12.97
LMC-N52	1.03 ± 0.12^a	6.34 ± 0.76	0.56 ± 0.10	3.66 ± 0.86
MagBridgeA	0.01 ± 0.002^d	0.06 ± 0.01	7.42 ± 1.25	395.78 ± 98.75
SMC-N83A	0.18 ± 0.01^e	5.76 ± 0.35	2.43 ± 0.35	21.14 ± 4.34
SMC-N83B	0.18 ± 0.03^e	9.10 ± 1.64	1.17 ± 0.23	10.46 ± 2.76
SMC-N84A	0.53 ± 0.29^e	8.94 ± 4.83	0.37 ± 0.20	7.31 ± 4.22
SMC-N84B	0.29 ± 0.04^e	2.40 ± 0.34	2.02 ± 0.35	25.74 ± 6.34

References. —
[a]M. Rubio private communication
[b]Bolatto et al. (2000)
[c]Wang et al. (2009)
[d]E. Muller private communication
[e]Bolatto et al. (2003)

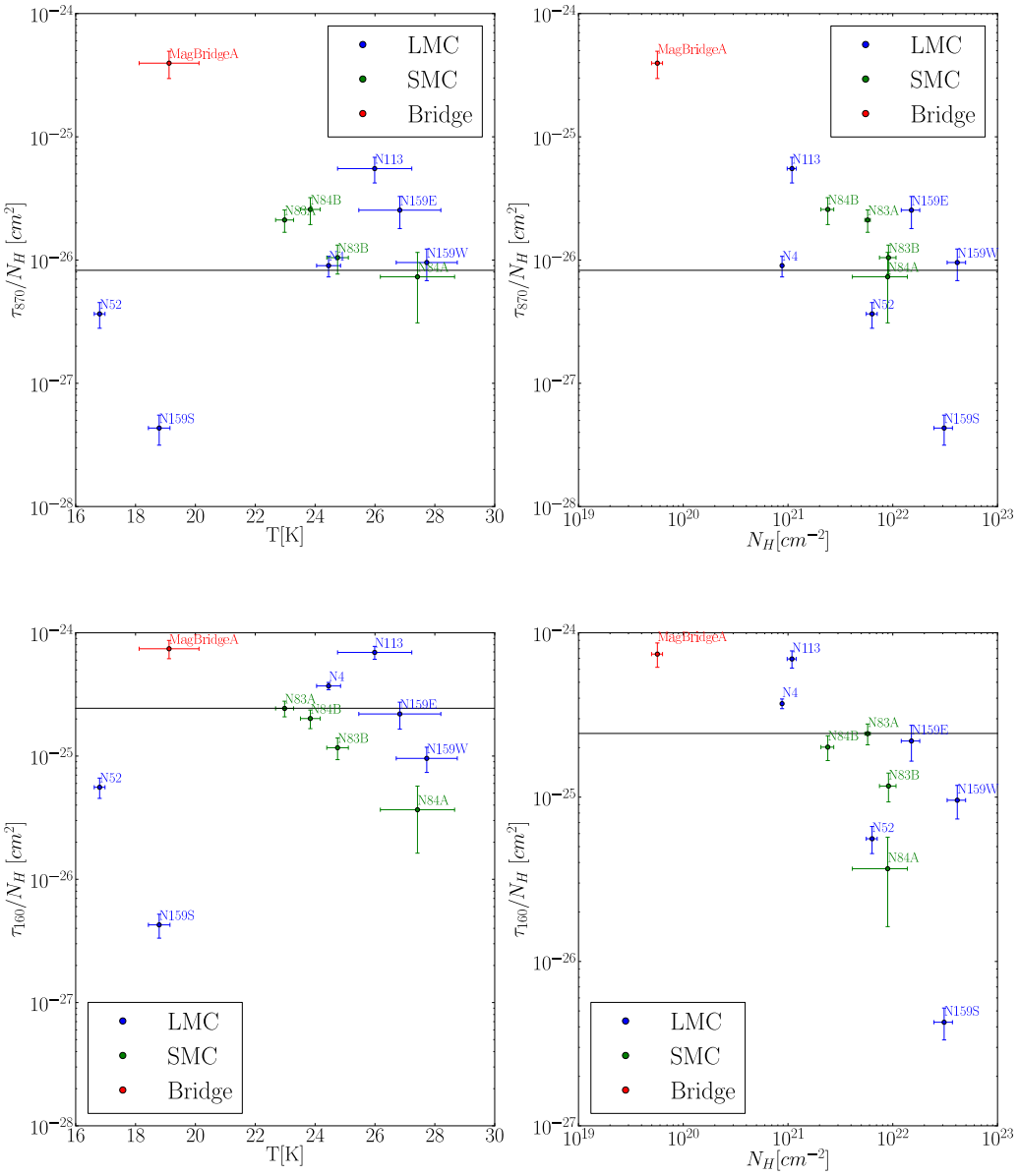

Figure 5.7: Results of optical depth per gas nucleon τ/N_H or emissivity per column. There is not apparent dependence with T, and it seems to be a negative relation with N_H.

5.2.1 Comparison with the Milky Way

In Boulanger et al. (1996) dust emissivity $\epsilon_d(\nu)$ was directly measured with infrared observations from the DIRBE and FIRAS instruments on board the COBE space telescope and HI data from the Leiden/Dwingeloo survey of the entire north sky, correlating the distribution of the IR emission at high Galactic latitude with that of the interstellar gas. This dust-to-gas correlation in zones of our Galaxy where the gas is diffuse resulted in a relation for the dust emissivity:

$$\frac{\tau_d(\lambda)}{N_H} = 1.0 \times 10^{-25} \left(\frac{\lambda}{250\mu m}\right)^{-2} cm^2 \tag{5.4}$$

which is remarkably close to the value in Draine & Lee (1984) and was recently corroborated by the Planck Collaboration et al. (2011) for a set of low velocity clouds at high galactic latitude in our Galaxy combining data from PLANCK and IRAS with 21-cm observations of HI from the Green Bank Telescope.

The horizontal lines in the plots of Figure 5.7 represent the value of τ/N_H obtained for our Galaxy in Boulanger et al. (1996). From Figure 5.7, at 870 μm, almost all SMC sources have values of τ/N_H higher than the Galactic, implying more dust emission per gas column. For the LMC the dispersion of the values is larger, but with most of them above the Galactic line (except for LMC-N52 and LMC-N159S). At 160 μm, only the Magellanic Bridge has a τ/N_H higher than the Galactic. Most of SMC points now fall below the Milky Way result, as well as the majority LMC points. This is because previously we were analysing the τ/N_H at 870 μm, with a clear excess of emission (as explained in the previous chapter) evident in this dust emission per gas column analysis.

But the key conclusion of this analysis is that most values of τ/N_H at 870 μm are higher than the Galactic result. In low metallicity systems, a lower content of dust is expected, resulting in lower values of dust emisiion per gas column (lower τ/N_H). Under the assumption of $M_g = M_{vir}$, if τ/N_H is higher of what was expected it is either because the virial mass is lower than the true gas mass (i.e. the virial approximation would be wrong) or the dust emissivity is higher at 870 μm

5.2.2 Emissivity of the dust (ϵ_d)

In these subsection we will assume the emissivities (ϵ_d, dust emissivity per H nucleon) explained in the previous subsection and calculate dust absorption coeffcients κ_μ (which is just the dust emissivity per dust gram) assuming a dust-to-gas ratio.

As explained in the previous subsection, the optical depth per gas nucleon is measured from the dust and gas emission as the quotient between the dust opacity and the HI column density (Boulanger et al. 1996):

$$\epsilon_d(\nu) = \frac{\tau_d(\nu)}{N_H} \tag{5.5}$$

which is close to a dust-to-gas ratio or an emissivity per gas column. Now, the dust opacity τ_d

Table 5.4. Dust emissivities per gas nucleon ϵ_d and absorption coefficients κ_d assuming a $M_g = M_{vir}$ and and a dust-to-gas ratio δ_d.

Source	$\epsilon_d^{160\mu m}[10^{-25} cm^2]$	$\epsilon_d^{870\mu m}[10^{-27} cm^2]$	$\kappa_d^{160\mu m}[cm^2/g]$	$\kappa_d^{870\mu m}[cm^2/g]$
LMC-N4	3.71 ± 0.25	9.01 ± 1.71	46.50 ± 3.15	1.13 ± 0.21
LMC-N159W	0.96 ± 0.22	9.55 ± 2.74	12.02 ± 2.78	1.20 ± 0.34
LMC-N159E	2.20 ± 0.54	25.39 ± 7.39	27.55 ± 6.77	3.19 ± 0.93
LMC-N159S	0.04 ± 0.01	0.43 ± 0.12	0.54 ± 0.12	0.05 ± 0.01
LMC-N113	6.93 ± 0.83	55.19 ± 12.97	86.99 ± 10.43	6.93 ± 1.63
LMC-N52	0.56 ± 0.10	3.66 ± 0.86	7.00 ± 1.31	0.46 ± 0.11
MagBridgeA	7.42 ± 1.25	395.78 ± 98.75	465.65 ± 78.71	248.35 ± 61.96
SMC-N83A	2.43 ± 0.35	21.14 ± 4.34	152.70 ± 22.15	13.26 ± 2.72
SMC-N83B	1.17 ± 0.23	10.46 ± 2.76	73.29 ± 14.61	6.56 ± 1.73
SMC-N84A	0.37 ± 0.20	7.31 ± 4.22	23.01 ± 12.79	4.59 ± 2.65
SMC-N84B	2.02 ± 0.35	25.74 ± 6.34	126.46 ± 21.71	16.15 ± 3.98

can be expressed in terms of the absorption coefficient as

$$\tau_d(\nu) = \kappa_d(\nu) \int \rho dl = \kappa_d(\nu)\Sigma_d \tag{5.6}$$

with $\kappa_d(\nu)$ the absorption coefficient per unit dust mass in $\left[cm^2 g^{-1}\right]$, ρ the gas density in $\left[g\ cm^{-3}\right]$, $\int dl$ is the integral in the line of sight and Σ_d the dust surface mass density in $\left[g\ cm^{-2}\right]$.

So the dust opacity is

$$\tau_d(\nu) = \kappa_d(\nu)\Sigma_d \tag{5.7}$$

where Σ_d is the dust surface density that can be expressed as a function of the gas superficial density Σ_g and the dust-to-gas ratio δ_d like

$$\Sigma_d = \Sigma_g \delta_d = \mu m_H N_H \delta_d \tag{5.8}$$

with N_H the H column density, μ the H molecular weight (1.36 including He) and m_H is the H mass, so

$$\tau_d(\nu) = \kappa_d \mu m_H N_H \delta_d \tag{5.9}$$

Therefore the dust emissivity can be expressed as a function of the dust absorption coefficient like

$$\epsilon_d(\nu) = \tau_d(\nu)/N_H = \kappa_d \mu m_H \delta_d \tag{5.10}$$

So from the results of the previous section of τ/N_H we have the dust emissivity for every source of the subsample for which CO data are available (Table 5.4), and using a dust to gas ratio, we obtain results for dust absorption coefficients as:

$$\kappa_d = \frac{\epsilon_d}{\mu m_H \delta_d} \tag{5.11}$$

Now, making the assumption that the dust-to-gas ratio depends linearly on the metallicity (Issa et al. 1990, James et al. 2002), from Draine et al. (2007)

$$\delta_d(\odot) = 0.007 \tag{5.12}$$

for the solar neighborhood, and using a linear dependence with the metallicity:

$$\delta_d(LMC) = \delta_d(\odot) Z_{LMC} \tag{5.13}$$

$$\delta_d(SMC) = \delta_d(\odot) Z_{SMC} \tag{5.14}$$

With these relations, we calculated dust absorption coefficients and present them in Table 5.4. With the obtained results of ϵ_d in the following section we will be able to calculate gas masses from the millimeter emission, and dust masses using the κ_ν with the assumption the dust-to-gas ratio depends linearly on the metallicity.

5.3 Gas and Dust Masses

In this section we will assume a result for the dust emissivity and dust-to-gas ratio and calculate gas and dust masses.

When observing molecular clouds at millimeter and submillimeter wavelengths, we can assume an optically thin medium ($\tau_\nu \ll 1$), so from the radiative transfer equation we get the thermal emission of a cloud of gas and dust:

$$I_\nu = \tau_d(\nu) B_\nu(T_d) \tag{5.15}$$

where τ_d is the dust opacity and $B_\nu(T_d)$ is the Planck function of the dust emitting at temperature T_d.

As explained in Equation 5.6, dust opacity τ_d can be expressed in terms of the absorption coefficient like

$$\tau_d(\nu) = \kappa_d(\nu) \int \rho dl = \kappa_d(\nu) \Sigma_d \tag{5.16}$$

If we combine equations (5.15) and (5.16) we get

$$I_\nu = \kappa_d(\nu) \Sigma_d B(T_d) \tag{5.17}$$

Integrating (5.17) in the source's solid angle $d\Omega = \frac{dA}{D^2}$ (dA is the differential area of the source and D the distance to the source) and recalling that Σ_d is the superficial dust density, we obtain the flux density as

$$S_\nu = \kappa_d B_\nu(T_d) \int \Sigma_d \frac{dA}{D^2} = \kappa_d B_\nu(T_d) \frac{M_d}{D^2} \tag{5.18}$$

so the dust mass in the cloud can be expressed as

$$M_d = \frac{S_\nu D^2}{\kappa_d(\nu) B_\nu(T)} \tag{5.19}$$

where S_ν is the flux density measured from the photometry, D is the distance to the cloud (50 kpc to LMC, 65 kpc to SMC) and T is the dust temperature obtained from the fit. Results of dust masses are presented in Table 5.5, using the assumption that the dust-to-gas ratios depends linearly on the metallicity to obtain the dust absorption coefficients.

It is important to highlight the assumption that in all our analysis we are assuming only a single dust temperature in the blackbody approximation, while in reality molecular clouds have distributions of dust temperatures.

Gas mass can also be obtained from dust emission. Recalling from the previous subsection that ϵ_d can be expressed as a function of the dust absorption coefficient κ_d as

$$\epsilon_d(\nu) = \kappa_d \mu m_H \delta_d \tag{5.20}$$

where x_d is a dust to gas ratio, i.e. $\delta_d = M_d/M_g$, we have that

$$M_g = \frac{M_d}{\delta_d} = \frac{S_\nu D^2}{\kappa_d(\nu) B_\nu(T) \delta_d} \tag{5.21}$$

and from 5.20

$$\kappa_d = \frac{\epsilon_d}{\mu m_H \delta_d} \tag{5.22}$$

so

$$M^H_{mm} = \frac{S_\nu D^2 \mu m_H}{\epsilon_d B_\nu(T_d)} \tag{5.23}$$

Equation (5.23) is the expression of gas mass obtained from the millimetric emission, where ϵ_d is the optical depth per gas nucleon, or emissivity, described in the previous section, obtained with the dust opacities calculated from the fitting results and the H column densities from the virial masses. Using the emission obtained at 870 and 160 μm and the dust emissivities and absorption coefficients we calculated in Table 5.4, dust and millimeter gas masses are presented in Table 5.5.

Comparison with the Milky Way

In the following we will compare the gas mass traced by the virial mass and the millimeter emission, which in our galaxy trace the same amount of gas.

In order to make a comparison with the results of Bot et al. (2010) of M_{vir}/M_{mm} in the SMC, we also calculated the gas millimeter masses for our sources using the same value of dust emissivity of Bot et al. (2010) of $3.94 \pm 0.05\ cm^2 g^{-1}$ (which is a Galactic value corrected for dust-to-gas ratio) and present these results in Figure 5.8. It can be seen that all sources in the SMC have $M_{mm} > M_{vir}$, as in Bot et al. (2010). This be interpreted as an underestimation of the total amount of gas by the virial mass (perhaps the virial equilibrium is not a valid assumption in these systems as discussed in the

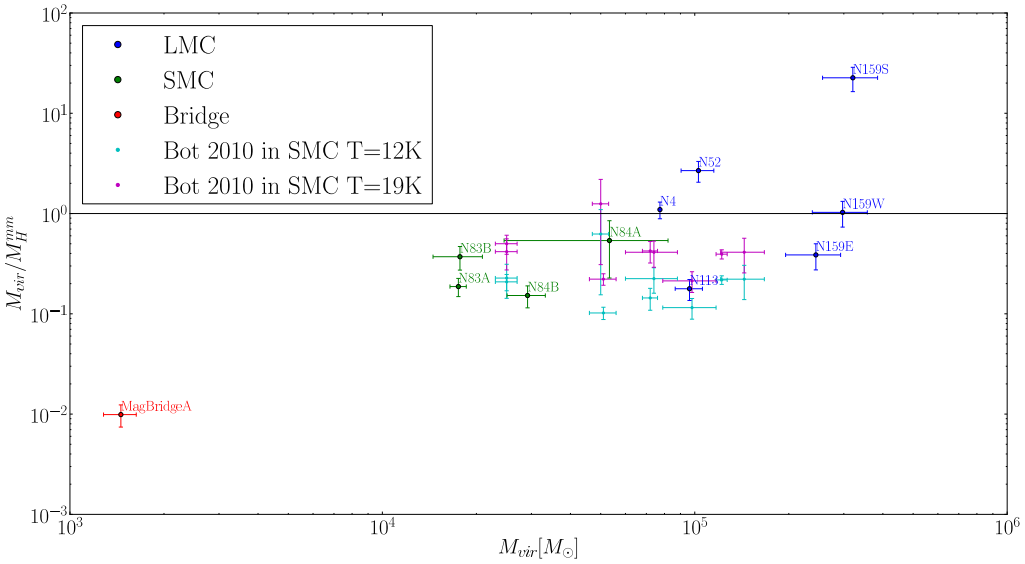

Figure 5.8: Ratios between virial and millimeter masses using ϵ_d of Bot et al. (2010) and SMC and MagBridgeA and corrected for LMC with the metallicity ratio with SMC.

previous analysis) or that the excess of emission observed in the millimeter range is causing an overestimation of the gas mass. High values of millimeter masses could also be due to a unrealistic low dust emissivity, implying that the use of the Galactic value of ϵ_d corrected for dust-to-gas ratio is incorrect. This would demonstrate that properties of dust emissivitie are different between the Magellanic system and our Galaxy. This trend for the SMC is not observed (at leat not so clear) in the LMC, with millimeter masses closer to the virial ones (except for N52 and N159S). Lower millimeter masses could be due to a lower dust content (which would be unexpected since the LMC has a higher metallicity), or a lower dust emission, but more data is needed to verify this result. MagBridgeA, with the highest excess of emission, has the highest millimeter mass.

5.4 Gas to Dust ratios

Finally, in this section we will asume a gas mas traced totally by the virial mass ($M_g = M_{vir}$) and a dust emissivity per gas column and calculate gas-to-dust ratios. This dust emissivity ϵ_d will be the Galactic value scaled with the dust-to-gas ratio for the SMC of Bot et al. 2010

We obtained gas to dust ratios as the quotient between gas and dust masses:

$$\frac{1}{\delta_d} = \frac{M_{gas}}{M_{dust}} \tag{5.24}$$

where the dust mass is obtained from the dust emission and the gas mass is derived from the virial mass, which under the assumptions made in this analysis, traces the total a mount of molecular gas in a cloud with spherical symmetry. Thus we can obtain the dust

Table 5.5. Dust masses (assuming a δ_d that depends linearly on the metallicity) and Gas masses derived from millimeter emission

Source	$M_d[10^2 M_\odot](160\mu m)$	$M^H_{mm}[10^4 M_\odot](160\mu m)$	$M_d[10^2 M_\odot](870\mu m)$	$M^H_{mm}[10^5 M_\odot](870\mu m)$
LMC-N4	1.12 ± 0.22	3.19 ± 0.63	2.71 ± 0.73	0.77 ± 0.21
LMC-N159W	2.45 ± 0.69	6.99 ± 1.96	10.45 ± 3.69	2.99 ± 1.05
LMC-N159E	5.07 ± 1.62	14.49 ± 4.63	8.57 ± 3.08	2.45 ± 0.88
LMC-N159S	7.49 ± 1.93	21.39 ± 5.52	11.30 ± 3.72	3.23 ± 1.06
LMC-N113	2.19 ± 0.51	6.26 ± 1.45	3.38 ± 10.72	0.97 ± 0.31
LMC-N52	2.56 ± 0.57	7.32 ± 1.62	3.61 ± 1.12	1.03 ± 0.32
MagBridgeA	0.008 ± 0.02	0.12 ± 0.04	0.01 ± 0.003	0.015 ± 0.005
SMC-N83A	0.12 ± 0.02	1.76 ± 0.32	0.12 ± 0.03	0.17 ± 0.05
SMC-N83B	0.11 ± 0.03	1.63 ± 0.43	0.13 ± 0.04	0.18 ± 0.06
SMC-N84A	0.37 ± 0.22	5.28 ± 3.09	0.37 ± 0.23	0.53 ± 0.33
SMC-N84B	0.26 ± 0.05	3.67 ± 0.76	0.20 ± 0.07	0.29 ± 0.09

Table 5.6. Gas-to-dust ratios, calculated with dust masses obtained from the emission at 870 and 160 μm (Table 5.5) and the virial masses obtained from the CO data in the literature in section 5.2 (see column 2 of Table 5.3)

Source	$1/\delta_d(160\mu m)[10^2]$	$1/\delta_d(870\mu m)[10^2]$
LMC-N4	6.92 ± 1.36	2.86 ± 0.77
LMC-N159W	12.16 ± 4.19	2.85 ± 1.15
LMC-N159E	4.81 ± 1.81	2.85 ± 1.17
LMC-N159S	4.28 ± 1.40	2.84 ± 1.09
LMC-N113	4.39 ± 1.11	2.85 ± 0.95
LMC-N52	4.01 ± 1.01	2.84 ± 0.94
MagBridgeA	17.36 ± 5.87	14.19 ± 5.00
SMC-N83A	14.25 ± 2.75	14.33 ± 4.16
SMC-N83B	15.51 ± 4.99	14.07 ± 5.26
SMC-N84A	14.42 ± 11.48	14.26 ± 11.63
SMC-N84B	11.34 ± 2.82	14.22 ± 4.95

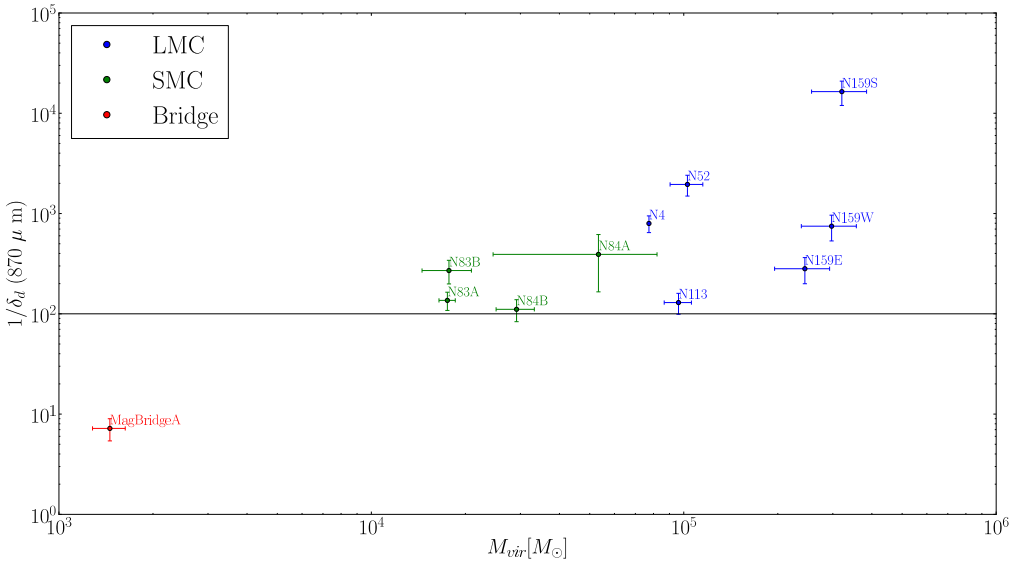

Figure 5.9: Gas-to-dust ratios calculated assuming a gas mass $M_{gas} = M_{vir}$ and a Galactic value of dust emissivity per gas column ϵ_d, scaled with the metallicity. The horizontal line represents the Galactic value of ~ 100 (Draine et al. 2007)

and gas masses from two independent methods to calculate the gas-to-dust ratios. We calculated dust masses using equation (5.19) with $\kappa_d = 1.26 \pm 0.02 cm^2 g^{-1}$ from Bot et al. 2010 calculated from the Galactic value of ϵ_d scaled with the dust to gas ratio for the SMC. We scaled this κ_d with metallicity using a factor 2.5 for the LMC. With these dust masses and virial masses we calculated gas-to-dust ratios ($1/\delta_d$) and present them in Figure 5.9 , where we have separated the sources for SMC, LMC and Magellanic Bridge. In our galaxy the typical value for gas to dust ratios is ~ 100 (marked as an horizontal line. Draine et al. 2007). From Figure 5.9 we can see that the values for SMC and LMC are above the Galatic line, indicating higher values of gas-to-dust ratios than in our Galaxy. This is coherent with the low metallicity of these systems that imply lower amounts of dust, since dust grains are composed of heavy elements that determine the metallicity of a system, like carbons and silicates. Figure 5.9 shows that in the SMC and LMC there are lower amounts of dust in relation with gas than in our Galaxy. Low amounts of dust make very difficult to explain the excesses of emission observed in the SEDs with a different dust mass component at a lower temperature. As in the previous analysis, we recover this separation between SMC and LMC values. It could be real, implying a difference between both galaxies, but more data is needed to verify this trend. MagBridgeA has the lowest value of gas-to-dust ratio, despite its low dust content expected from its low metallicity. This result can be explained with the high excess of emission at 870 μm for this source.

Additionally, we calculated gas-to-dust ratios by using both, the dust masses obtained from the emission at 870 and 160 μm (Table 5.5) with the dust absorption coefficients of Table 5.4, and the virial masses obtained from the CO data in the literature in section 5.2 (see column 2 of Table 5.3). We present these results in Table 5.6.

Chapter 6

Summary and Conclusions

This work presents observations and results of dust continuum emission at 870 μm using the LABOCA bolometer of the APEX telescope, for the first time of several molecular clouds in the Magellanic system. One source in the Magellanic Bridge is of particular interest since it is the first time that a molecular cloud in this region is observed at 870 μm. Most of these sources are faint and extended, and due to the high emission of the sky at these wavelenghts, the reduction of the LABOCA data is rather complex, since it involves an iterative process with many variable to consider and requires several hours of computer time. This iterative process produces a dust continuum map at each step that will be used in the next iteration. By using a signal-to-noise mask we remove the source from the map before the reduction in iteration i and add it back to the map before iteration $i+1$. This process is repeated as many times as needed until reaching a good signal-to-noise (>10 in most cases).

We carried out an aperture photometry in the LABOCA maps to obtain flux densities. After subtracting CO and free-free contributions at 870 μm, we present the results of dust emission at 870 μm for all the sources in the sample, with density fluxes ranging between 0.1 and 16 Jy. This kind of work has been done previously only for sources in the SMC-SW region, others than our own.

The LABOCA data are complemented with Spitzer data at 70 and 160 μm and unpublished HERSCHEL data at 100, 160, 250, 350 and 500 μm in order to obtain flux densities at the corresponding wavelengths and construct spectral energy distributions (SED's). A simple modified blackbody law was fitted to these SED's in order to obtain dust temperatures, spectral emissivity indices and dust opacities. Average values of dust temperatures for LMC, SMC and Magellanic Bridge are 22, 24 and 19 K respectively, and for the spectral emissivity indices these values are 1.7, 1.6 and 1.7. Finally, for the dust opacities at 870 μm the mean values for the LMC, SMC and Magellanic Bridge are $9{\cdot}10^{-5}$, $4{\cdot}10^{-5}$ and $2{\cdot}10^{-5}$ respectively.

From the SED's obtained, a clear excess of emission is observed at 870 μm with respect to the modified blackbody law fitted, a result previously reported at these long wavelengths for molecular clouds in the Magellanic system and entire low metalliciy galaxies, including the Magellanic Clouds (Sauvage et al. 1990, Aguirre et al. 2003, Galametz et al. 2011, Israel et al. 2010). For the LMC, these excesses varie from 0.3 to 3 times of what was

predicted by the modified blackbody law at 870 μm, and from 1.3 to 2.5 for the SMC. The source in the Magellanic Bridge reported the highest excess with a factor of 9. This result is of particular interest because it is the first source in the Magellanic Bridge to ever been studied at these wavelenghts, and this system has a lower metallicity than the LMC and SMC, a factor that could be related to the high excess of emission.

The excess observed at 870 and 70 μm along with parameters obtained from the fitting procedure, T, β and τ were analyzed in order to detect a possible relation between them. With a rank correlation coefficient analysis only a negative monotonic relation was determined between the dust temperature and the excess observed at 70 μm, and this excess turned out to be higher for the SMC than for the LMC. In order to determine if the differences in these properties where separated in SMC and LMC we made a Kolgomorov-Smirnov test with the null hypothesis that the distribution of each one of these properties in the SMC and LMC came from the same parent distribution. This hypothesis could be rejected only for the excesses at 70 μm, the $\beta's$ and the $\tau's$ at 160 μm with confidence levels of 5% and 1%, so the differences observed between SMC and LMC in the distributions of these parameters could be due to the fact that we are looking at two different galaxies, and their different properties, like metallicity for example, could be influencing these parameters. The origin of the excess of emission at 870 μm is not clear yet. One option is the possibility of a second dust component at a lower temperature, but due to the high levels of excesses reported in most sources (2 times higher than the value predicted by the model), a large amount of colder dust would be needed to explain these excess, which would be difficult to obtain. For example, for the source in the Magellanic Bridge, to obtain a component with its peak of emission at 870 μm, its temperature would have to be around 3 K, implying a dust mass of 185 $M_{\odot}$, whereas the dust temperature that fits all the other points in the SED is 19 K implying a dust mass of just 1 $M_{\odot}$.

From the dust emission, three parameters can be obtained and analysed: gas mas, dust emissivity and dust-to-gas ratio. We made an analysis of three parts, assuming as known two of the parameters and leaving the third one as unknown in each part.

In the first part we assumed a gas mas traced as the virial mass and a dust-to-gas ratio to calculate dust emissivities. CO complementary data taken from the literature was included in order to determine H column densities which, along with the dust opacities, helped us to determine dust emissivities and absorption coefficients. Dust emissivities per gas column (τ/N_H) do not seem to have a trend with dust temperature, either at 870 or 160 μm. Two sources in particular, N159S and N52 have lower dust emissivities than the rest of the LMC sources, which could be related to their lack of star formation activity. Also, dust emissivities seem to have a negative trend with the column density N_H, which it was unexpected since if dust and gas are correlated, larger amounts of gas columns should allow larger values of τ/N_H, implying a rather flat tendency. The source in the Magellanic Bridge has the highest values of τ/N_H, implying more dust emission per gas column, more than the SMC or LMC with their higher metallicities. Results of emissivities (τ/N_H) are compared with the values for our galaxy obtained in Boulanger et al. (1996) at 160 and 870 μm. One interesting result is that this value for the Magellanic Bridge source is considerably higher than the Galactic value, both at 160 and 870 μm, implying that in this region the dust emission is higher in comparison to the gas emission. The results of τ/N_H at 870 μm are higher than those at 160 μm, indicating the presence

of the excess of emission of the dust at this wavelength.

In the second part, we assumed a dust emissivity and a dust-to-gas ratio and calculated dust and gas masses. With the results of emissivity and absorption coefficients we were able to calculate dust and gas masses and make important comparisons with our Galaxy. Using the result of dust emissivity in Bot et al. (2010) we calculated gas masses obtained from the millimeter emission and compared them to their results of M_{vir}/M_{mm}. As in Bot et al. (2010), in our sources these ratios turned out to be smaller than for our galaxy, where virial and millimetric masses trace the same amount of gas. This result in the Magellanic Clouds could be explained as a overestimation of the gas mass at millimeter wavelengths due to the excess of emission observed or that maybe the assumption of virial equilibrium is not valid in these systems, implying an underestimation of the total amount of gas.

From these two first analysis we conclude the dust emissivity at 870 μm is higher or the virail mass does not trace the total amount of gasm making the virial approximation a wrong one. This could be explained with the low dust content from the low metallicity od these systems (see last paragraph).

Finally, we assumed a gas mass ($M_g = M_{vir}$) and a Galactic dust emissivity corrected for metallicity to calulate gas-to-dust ratios. We used dust masses obtained from the millimeter emission and gas masses from CO data and virial approximation to obtain gas-to-dust ratios, which turned out to be larger than the typical value for our galaxy ($\sim$100, Draine et al. 2007). This is related with the low metallicity of these systems that imply lower amounts of dust, since dust grains are composed of heavy elements that determine the metallicity of a system, like carbons and silicates. Figure 5.9 shows that in the SMC and LMC there are lower amounts of dust in relation with gas than in our Galaxy. This result makes very difficult to explain the excesses of emission observed in the SEDs as a different dust mass component at a lower temperature, since a large amount of dust would be needed.

A lower dust content in these molecular clouds could be an explanation for the mass discrepancy between dust and CO emission, since dust particles are a natural shield for CO molecules from the surrounding UV radiation, capable of photo-dissociating the molecule. Due to this photo-dissociation the amount of CO in molecular clouds is diminished, probably making its distribution in molecular clouds less homogeneous (more clumpy). This would imply a weaker velocity dispersion measured from the CO line and a subsequent underestimation of the gas mass traced by this molecule and the viral approximation.

Bibliography

Aguirre, J. E., et al. 2003, ApJ, 596, 273

Belloche, A., et al. 2011, A&A, 527, A145

Bolatto, A. D., Jackson, J. M., Israel, F. P., Zhang, X., & Kim, S. 2000, ApJ, 545, 234

Bolatto, A. D., Leroy, A., Israel, F. P., & Jackson, J. M. 2003, ApJ, 595, 167

Bolatto, A. D., et al. 2007, ApJ, 655, 212

Bot, C., Boulanger, F., Rubio, M., & Rantakyro, F. 2007, A&A, 471, 103

Bot, C., et al. 2010, A&A, 524, A52

Boulanger, F., Abergel, A., Bernard, J.-P., Burton, W. B., Desert, F.-X., Hartmann, D., Lagache, G., & Puget, J.-L. 1996, A&A, 312, 256

Dame, T. M., Hartmann, D., & Thaddeus, P. 2001, ApJ, 547, 792

Dickel, J. R., Gruendl, R. A., McIntyre, V. J., & Amy, S. W. 2010, AJ, 140, 1511

Draine, B. T., & Lee, H. M. 1984, ApJ, 285, 89

Draine, B. T., et al. 2007, ApJ, 663, 866

Galametz, M., Madden, S. C., Galliano, F., Hony, S., Bendo, G. J., & Sauvage, M. 2011, A&A, 532, A56

Griffin, M., et al. 2006, in Society of Photo-Optical Instrumentation Engineers (SPIE) Conference Series, Vol. 6265, Society of Photo-Optical Instrumentation Engineers (SPIE) Conference Series

Güsten, R., Nyman, L. Å., Schilke, P., Menten, K., Cesarsky, C., & Booth, R. 2006, A&A, 454, L13

Guzmán, V. 2010, Master's thesis: Emisión de polvo frío y gas molecular en las regiones de 30 dorado y N83-N84 en las Nubes de Magallanes

Heydari-Malayeri, M., & Lecavelier Des Etangs, A. 1994, A&A, 291, 960

Hildebrand, R. H. 1983, QJRAS, 24, 267

Hilditch, R. W., Howarth, I. D., & Harries, T. J. 2005, MNRAS, 357, 304

Israel, F. P., Wall, W. F., Raban, D., Reach, W. T., Bot, C., Oonk, J. B. R., Ysard, N., & Bernard, J. P. 2010, A&A, 519, A67

Israel, F. P., et al. 1993, A&A, 276, 25

Issa, M. R., MacLaren, I., & Wolfendale, A. W. 1990, A&A, 236, 237

James, A., Dunne, L., Eales, S., & Edmunds, M. G. 2002, MNRAS, 335, 753

Keller, S. C., & Wood, P. R. 2006, ApJ, 642, 834

MacLaren, I., Richardson, K. M., & Wolfendale, A. W. 1988, ApJ, 333, 821

Maeder, A., Grebel, E. K., & Mermilliod, J.-C. 1999, A&A, 346, 459

Meixner, M., et al. 2006, AJ, 132, 2268

Pardo, J. R., Cernicharo, J., & Serabyn, E. 2001, IEEE Trans. on Antennas and Propagation, 49, 1683

Persson, S. E., Madore, B. F., Krzemiński, W., Freedman, W. L., Roth, M., & Murphy, D. C. 2004, AJ, 128, 2239

Planck Collaboration et al. 2011, A&A, 536, A24

Poglitsch, A., et al. 2010, A&A, 518, L2

Rantakyrö, F. T., Rubio, M., Johansson, L. E. B., Chini, R., & Merkel-Ferreira, E. 2005, in Astronomical Society of the Pacific Conference Series, Vol. 344, The Cool Universe: Observing Cosmic Dawn, ed. C. Lidman & D. Alloin, 215

Rubio, M., Boulanger, F., Rantakyro, F., & Contursi, A. 2004, A&A, 425, L1

Rubio, M., Lequeux, J., & Boulanger, F. 1993a, A&A, 271, 9

Rubio, M., et al. 1993b, A&A, 271, 1

—. 1996, A&AS, 118, 263

Sauvage, M., Vigroux, L., & Thuan, T. X. 1990, A&A, 237, 296

Schuller, F., Nord, M., Vlahakis, C., Albrecht, M., Beelen, A., Bertoldi, F., Mueller, S., & Schaaf, R. 2008, BoA - The Bolometer Data Analysis Software User and Reference Manual

Siringo, G., et al. 2009, A&A, 497, 945

Wang, M., Chin, Y.-N., Henkel, C., Whiteoak, J. B., & Cunningham, M. 2009, ApJ, 690, 580

Appendix A

Reduction Scripts

BoA reduction of LABOCA data was done using the following codes and instructions:
Step 1: Obtain flux correction factors:

These values are obtained with the 'reduce-calib-loop.boa' script, that loop over every calibrator scans (corresponding to planets or secondary calibrators) and uses the $\tau's$ values obtained from the radiometer. these factors will be stored in the Laboca-calib.dat file and used in every step of the iterative reduction. The 'reduce-calib-loop.boa' script is:

```
from boa.fortran import fStat
from boa.Utilities import getTau
import os

scans=[61013,61373,61793,61972,80599,80600,80601,80859,81233] #calibrators, just for project C-086.F-0679A-2010
output=file('/home/celia/Dropbox/datos_laboca/C-086.F0679-2010/Reduction/BoaRed/Laboca-calib.dat','w')
taus=[0.261,0.342,0.26,0.183,0.304,0.292,0.29,0.315,0.419] #calibrators taus for project C-086.F-0679A-2010

ok = 0
for num in range(len(scans)):
    try:
        ok = read(str(scans[num]))
    except:
        ok = -1

    if ok == 0:
        scannr = scans[num]
        mjdref = fStat.f_mean(data.ScanParam.MJD)
        tau=taus[num]
        scandate = data.ScanParam.DateObs
        scanmjd = data.ScanParam.MJD[0]
        scanel  = fStat.f_mean(data.ScanParam.El)
        taucorr = exp(tau/sin(scanel * pi / 180.))

        data.correctOpacity(tau)
        execfile(os.path.join(os.getenv('BOA_HOME_LABOCA'), 'reduce-calibrator.boa'))

        output.write('%i  %s %18.12f %5.3f %5.3f\n' %(scannr,scandate,scanmjd,calcorrmap,taucorr))


output.close()
```

Step 2: Define the main reduction script `reduce-map-weaksource.boa` that will be used in every iteration (This is the core of the reduction)

```
############################################################
#
# reduce-map-weaksource.boa
# script for pipeline reduction of LABOCA data
# optimised for weak source
#
# Note that opacity is not corrected in this script
#

# Read LABOCA specific definitions
import os
if not os.getenv('BOA_HOME_LABOCA'):
   raise 'Environment variable BOA_HOME_LABOCA undefined'
labocadir = os.getenv('BOA_HOME_LABOCA') + '/'
try:
        execfile(labocadir + 'cabling.py')
        execfile(labocadir + 'Laboca-RCPs.py')
except IOError:
        print " *** Some important file not found, exiting !!!"
        raise

CntstoJy(data)
mjdref = data.ScanParam.MJD[0]
rcp=getLabocaRCP(mjdref)
updateRCP(rcp)
flagRCP(rcp)

data.zeroStart()
flat()

# Flag bad channels
flagC(resistor)
cross=getLabocaCross(mjdref)
flagC(cross)
flagC(sealed_may07)

# Flag stationary points and high acceleration
data.flagSpeed (below=30.)
data.flagSpeed(above=500.)
data.flagAccel(above=800.)

# Flag dead and very noisy channels
data.flagFractionRms(ratio=5)

# First correlated noise removal on all channels and despiking
medianNoiseRemoval(chanRef=-1,factor=0.9,nbloop=5)
despike(below=-5,above=5)

# correlated noise removal by groups and boxes of channels
# (Laboca wireing)
correlbox(data,factor=0.95,nbloop=3)
correlgroup(data,factor=0.8,nbloop=3)

# Flag noisy channels
data.flagFractionRms(ratio=5)

# Despiking
despike(below=-5,above=5)

# Filter on low frequencies
data.flattenFreq(below=0.1,hiref=0.15)
```

```
base(order=1,subscan=0)
despike(below=-5,above=5)

# Compute weights based on rms off each channel
weight()
```

Step 3: iterative reduction

There are three main steps defined in this iterative process: a first reduction done with the basic "weak source" reduction given above with the code `'first-reduction.py'`:

```
op()
indir('/liukura/celia/C-086.F0679-2010/rawdata')
proj('C-086.F-0679-2010')
ils()

#LMC-N4
scans=[62003,62004,62005,62006,62007] #for the source LMC-N4
taus=[0.187,0.195,0.191,0.182,0.192]
ra1,ra2=73.4,72.7
de1,de2=-67.05,-66.80


ms = 0
for num in range(len(scans)):
    s=str(scans[num])
    read(s)
    mjdref = fStat.f_mean(data.ScanParam.MJD)
    tau=taus[num]
    data.correctOpacity(tau)
    calcorr = getCalCorr(mjdref,'linear','/liukura/celia/C-086.F0679-2010/Reduction/BoaRed/Laboca-calib-v2.dat')
    data.Data /= array(calcorr,'f')
    ###
    execfile('/usr/local/boa/laboca/reduce-map-weaksource.boa')
    data.doMap(system='EQ',sizeX=[ra1,ra2],sizeY=[de1,de2],oversamp=4)
    if ms:
      ms = mapsumfast([ms,data.Map])
    else:
      ms = copy.deepcopy(data.Map)

ms.dumpMap('LMC-N4_BoA_iter_1.data')
ms.smoothBy(13./3600.)
ms.display()
ms.writeFits('LMC-N4_BoA_iter_1.fits')
```

The result of running this script is then used in the next script: `'iter-flag.py'`, which works quite similar to `'first-reduction.py'` except that it first 'flags' data that is only above a certain signal to noise threshold (3.5 in this case) in order to reduce only significant data and to get rid of the extra noise so present in these weak and extended sources. This script is iterated three times.

```
modelo = restoreFile('LMC-N4_BoA_iter_1.data')
snr = copy.deepcopy(modelo) # compute a S/N map named as snr
snr.smoothBy(12./3600.)
snr.Data *= sqrt(snr.Weight)
snr.computeRms()
snr.Data /= array(snr.RmsBeam,'f')


#test = snr.Data < 3.5 or modelo.Data == float('nan')
#modelo.Data = where(test,0.,modelo.Data)
#modelo.smoothBy(12./3600.)

ms2 = 0 #initialise sum map
scans=[62003,62004,62005,62006,62007] #for source LMC-N4
taus=[0.187,0.195,0.191,0.182,0.192]

for num in range(len(scans)):
        s=str(scans[num])
        read(s)
        mjdref = fStat.f_mean(data.ScanParam.MJD)
        tau=taus[num]
        data.correctOpacity(tau)
        calcorr = getCalCorr(mjdref,'linear','/liukura/celia/C-086.F0679-2010/Reduction/BoaRed/Laboca-calib.dat')
        data.Data /= array(calcorr,'f')
        #FLAG SOURCE in the 2 or 3 iterations instead of subtracting. use the SNR map above 3.5 sigma for this
        data.flagSource(model=snr,threshold=3.5,flag=8)
        execfile('/usr/local/boa/laboca/reduce-map-weaksource.boa')
        #unflag source
        data.unflag(flag=8)
        data.doMap(system='EQ',sizeX=[ra1,ra2],sizeY=[de1,de2],oversamp=4)
        if ms2:
                ms2 = mapsumfast([ms2,data.Map])
        else:
                ms2 =copy.deepcopy(data.Map)  #if it is the first scan

ms2.dumpMap('LMC-N4_BoA_iter_2.data')
ms2.smoothBy(13./3600.)
ms2.display()
ms2.writeFits('LMC-N4_BoA_iter_2.fits')
```

Finally, after the flagging iterations are done, the last result is used in the final script: 'iter-subtract.py', in which a mask is created from the previous map with all pixel values with signal to noise below a given threshold (3.5 in this case) are set to zero, thus the mask considers only the source. This mask is subtracted from the data before doing the reduction and then it is add back after the reduction is done. Each time this step is done, the cleaning of the map from the noise is more efficient, so this step is iterated as many times as necessary until a clear image of the source is obtained.

```
modelo = restoreFile('LMC-N4_BoA_iter_4.data')
snr = copy.deepcopy(modelo)
snr.smoothBy(12./3600.)
snr.Data *= sqrt(snr.Weight)
snr.computeRms()
snr.Data /= array(snr.RmsBeam,'f')


test = snr.Data < 3.5 or modelo.Data == float('nan')
modelo.Data = where(test,0.,modelo.Data)
```

```
modelo.smoothBy(12./3600.)

ms = 0
scans=[62003,62004,62005,62006,62007] #for source LMC-N4
taus=[0.187,0.195,0.191,0.182,0.192]

for num in range(len(scans)):
        s=str(scans[num])
        read(s)
        mjdref = fStat.f_mean(data.ScanParam.MJD)
        tau=taus[num]
        data.correctOpacity(tau)
        calcorr = getCalCorr(mjdref,'linear','/liukura/celia/C-086.F0679-2010/Reduction/BoaRed/Laboca-calib.dat')
        data.Data /= array(calcorr,'f')
        CntstoJy(data)
        #SUBTRACT SOURCE USING THE MODEL YOU GET FROM THE FLAGED ITERATION.
        #data.doMap(system='EQ',sizeX=[ra1,ra2],sizeY=[de1,de2],oversamp=3)
        data.addSource(model=modelo,factor=-1)
        #data.doMap(system='EQ',sizeX=[ra1,ra2],sizeY=[de1,de2],oversamp=3)
        execfile('/usr/local/boa/laboca/reduce-map-weaksource-subtract.boa')
        data.computeWeight()
        #data.doMap(system='EQ',sizeX=[ra1,ra2],sizeY=[de1,de2],oversamp=3)
        data.addSource(model=modelo,factor=1)
        data.doMap(system='EQ',sizeX=[ra1,ra2],sizeY=[de1,de2],oversamp=4)
        if ms:
                ms = mapsumfast([ms,data.Map])
        else:
                ms =copy.deepcopy(data.Map)


ms.dumpMap('LMC-N4_BoA_iter_5.data')
ms.smoothBy(13./3600.)
ms.display()
ms.writeFits('LMC-N4_BoA_iter_5.fits')
```

Where `'reduce-map-weaksource-subtract.boa'` is the same as `'reduce-map-weaksource.boa'` except for the line `CntstoJy(data)` that now is commented. This code is iterated as many time as necessary until the source is shown clearly with a good S/N (tipycally 10 iterations).

Appendix B

Image Proccesing

```
import pyfits as pf
import scipy as sc
import numpy as np
import astLib as a
import matplotlib.pyplot as plt
import matplotlib.mlab as mlab
import stsci
from stsci.convolve import convolve2d


LMC8_6_GHz_2D = pf.open('LMC8.6-i.m_2D.fits')              # ATCA image
LMC8_6_GHz_2D_data = LMC8_6_GHz_2D[0].data                 # data table
hdr_LMC8_6_GHz_2D = pf.getheader('LMC8.6-i.m_2D.fits')     # image header
wcs_atca=a.astWCS.WCS('LMC8.6-i.m_2D.fits')                # coordinate system
cdelt_atca = abs(hdr_LMC8_6_GHz_2D['CDELT1'])*3600         # width of 1 pixel in arcseconds


N4_laboca = pf.open('LMC-N4_BoA_iter_6_9.fits')            # LABOCA image
N4_laboca_data = N4_laboca[0].data
N4_laboca_hdr = pf.getheader('LMC-N4_BoA_iter_6_9.fits')
wcs_laboca=a.astWCS.WCS('LMC-N4_BoA_iter_6_9.fits')
cdelt_laboca = abs(N4_laboca_hdr['CDELT1'])*3600



FWHFi = 21.999996341748     # ATCA FWHM in arcsec
FWHFf = 22.3842672          # LABOCA FWHM in arsec

# define a 2D array for the kernel. It's width must be about 3 times the final FWHM
n=15
ker=np.zeros((n,n))
x0=y0=n/2
i=j=0

for i in range(n):
  for j in range(n):
    ker[i,j]=(abs(i-x0))**2+(abs(j-y0))**2



kernel=np.exp(-8.*np.log(2)*cdelt_atca*ker/(FWHFf**2-FWHFi**2))      # gaussian kernel
kernel = kernel*(np.sum(kernel)**(-1))                               # normalization

im_conv = 0
im_conv=convolve2d(LMC8_6_GHz_2D_data,kernel,output=None,fft=0,mode='nearest',cval=0.)   # convolution
hdr_LMC8_6_GHz_2D.update('FWHM_con','22.4 #arcsec')
```

```
pf.writeto('LMC8.6-i.m_2D_FWHM_22.4_arcsec_LABOCA.fits',im_conv,hdr_LMC8_6_GHz_2D) # ATCA image with
                                                                                   # LABOCA FWHM = 22.4''
```

Once the ATCA image is convolved to the LABOCA (worst) resolution, it must be projected in the LABOCA coordinate grid so every pair of corresponding pixels in both ATCA and LABOCA actually have the same celestial coordinates and a one-to-one subtraction of both images.

```
imagen_atca = 'LMC8.6-i.m_2D_FWHM_22.4_arcsec_LABOCA.fits'

atca_conv = pf.open(imagen_atca)
atca_conv_data = atca_conv[0].data
wcs_atca_conv = a.astWCS.WCS(imagen_atca)
atca_conv_hdr = pf.getheader(imagen_atca)

imagen_laboca = 'LMC-N52_BoA_iter_RM_10.fits'

source_laboca = pf.open(imagen_laboca)
source_laboca_data = source_laboca[0].data
wcs_laboca=a.astWCS.WCS(imagen_laboca)
source_laboca_hdr = pf.getheader(imagen_laboca)

resampleo=a.astImages.resampleToWCS(source_laboca_data,wcs_laboca,atca_conv_data,wcs_atca_conv,highAccuracy=True, /
onlyOverlapping=True)                                    # projection of ATCA image onto LABOCA coordinate grid
pf.writeto('LMC-N52_atca_on_laboca_grid.fits',resampleo['data'],source_laboca_hdr)  # ATCA imagen on LABOCA grid

imagen_projectada = 'LMC-N52_atca_on_laboca_grid.fits'
atca_projected =pf.open(imagen_projectada)
atca_projected_data = atca_projected[0].data
wcs_laboca = a.astWCS.WCS(imagen_laboca)
wcs_atca_projected = a.astWCS.WCS(imagen_projectada)

match=a.astWCS.findWCSOverlap(wcs_laboca,wcs_atca_projected)   # to verify if coordInates
match                                                          # and pixels match between both images.
```

Finally the convolved and projected ATCA images are transformed from 8.6 GHz to 345 GHz with a $S_\nu \propto \nu^{-0.1}$ law and then subtraced to the LABOCA maps in order to get clean dust maps, without free-free contribution.

```
atca_projected_data = atca_projected_data*((345./8.64)**(-0.1))   # conversion from 8.6GHz to 345 GHz emission

mapa_limpio = source_laboca_data - atca_projected_data            # subtraction of both maps

pf.writeto('LMC-N52_BoA_iter_RM_10_free_free_subtracted.fits',mapa_limpio,source_laboca_hdr)  # LABOCA image
                                                                                              # without free-free
                                                                                              # contribution.
```

Appendix C

Photometry scripts for IRAF

Photometry was done with the 'qphot' task in the 'digiphot.apphot' package of IRAF, using the following template. Parameters chosen are aperture, annulus and dannulus. Image name and source image coordinates mus also be entered.

```
                                  I R A F
                       Image Reduction and Analysis Facility
PACKAGE = apphot
   TASK = qphot

image   = LMC-N4_BoA_iter_6_9.fits[0]  The input image(s)
cbox    =                    1.  The centering box width in pixels
annulus =                    6.  The inner radius of sky annulus in pixels
dannulus=                    2.  The width of the sky annulus in pixels
aperture=                  3.0  The list of photometry apertures
(coords =            LMC-N4.coo) The input coordinate file(s) (default: *.coo.?)
(output =              default) The output photometry file(s) (default: *.mag.?)
(plotfil=                     ) The output plot metacode file
(zmag   =                  25.) The zero point of the magnitude scale
(exposur=                     ) The exposure time image header keyword
(airmass=                     ) The airmass image header keyword
(filter =                     ) The filter image header keyword
(obstime=                     ) The time of observation image header keyword
(epadu  =                   1.) The instrument gain in e-/ADU
(interac=                   no) Interactive mode ?
(radplot=                   no) Plot the radial profiles in interactive mode ?
(icomman=                     ) Image cursor: [x y wcs] key [cmd]
(gcomman=                     ) Graphics cursor: [x y wcs] key [cmd]
(wcsin  =             )_.wcsin) The input coordinate system (logical,tv,physical,wo
(wcsout =            )_.wcsout) The output coordinate system (logical,tv,physical)
(cache  =             )_.cache) Cache input image pixels in memory ?
(verbose=           )_.verbose) Print messages in non-interactive mode ?
(graphic=          )_.graphics) Graphics device
(display=           )_.display) Display device
(mode   =                  ql)
```